The role of substrate orientation induced strain on the $GdMnO_3$ epitaxial thin films properties

Pedro Jorge Correia Machado
MAP-fis Doctoral Program in Physics
Department of Physics and Astronomy
2023

Supervisor
Joaquim Agostinho Moreira, Professor Associado com Agregação,
Faculdade de Ciências da Universidade do Porto

Co-supervisor
Abílio Almeida, Professor Associado,
Faculdade de Ciências da Universidade do Porto

Universidade do Minho

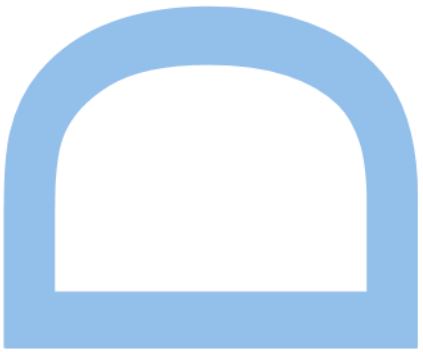

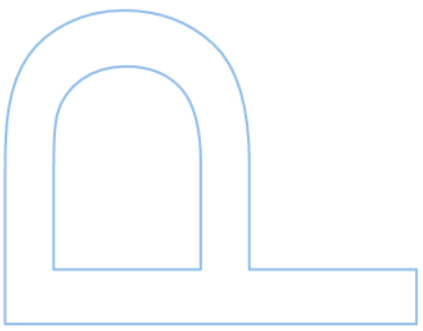

To my daughter Sara Gil Machado

Acknowledgements

I would like to thank my supervisors Joaquim Agostinho Moreira and Abílio Almeida, my family and friends as well as all the colleagues, technicians and professors from FCUP, UMINHO, UTAD and INESC-MN who helped to carry out this work.
Finally, I also thank Fundação para a Ciência e a Tecnologia (FCT) for the fellowship SFRH/BD/108509/2015.

Resumo

Entre as perovskitas de terras raras, o $GdMnO_3$ ortorrômbico revela-se um material interessante para sondar o conceito de propriedades para demanda, pois apresenta forte correlação entre graus de liberdade spin-orbital-rede que podem ser adaptados através de engenharia de deformação. Por deformação epitaxial em filmes finos, a estrutura pode alterar e surgir novas/inesperadas fases e propriedades físicas.

Nesta tese, apresentamos um estudo experimental do efeito da deformação nas propriedades de filmes finos de $GdMnO_3$ não relaxados, depositados em substratos de $SrTiO_3$ orientados (001) e (110) por meio de pulverização catódica em magnetrão-RF. A estrutura, microestrutura, propriedades dielétricas e magnéticas dos filmes preparados foram investigadas em detalhe.

De acordo com as orientações dos substratos, duas classes cristalográficas diferentes foram observadas, exibindo propriedades diferentes, evidenciando a importante influência da orientação do substrato nas interações microscópicas subjacentes tanto ao magnetismo quanto às propriedades dielétricas.

Os resultados de XRD revelaram que os filmes finos de $GdMnO_3$ depositados em substratos (001)- $SrTiO_3$ exibem uma simetria tetragonal, com o seu eixo perpendicular à superfície do filme e em que os parâmetros da rede basal são impostos pela estrutura cúbica do substrato. O surgimento de uma polarização elétrica espontânea abaixo de ~ 31 K aponta para a estabilização de uma fase ferroelétrica imprópria em baixas temperaturas, o que não é observado no $GdMnO_3$ em bulk.

Os filmes finos de $GdMnO_3$ depositados em substratos (110)- $SrTiO_3$ exibem uma simetria ortorrômbica epitaxial tensionada e crescem preferencialmente na orientação fora do plano (001), em que os parâmetros da rede basal são deformados pela rede do substrato, impondo uma fase α geminada nos filmes finos de $GdMnO_3$ na direção (100) que evoluem para uma fase γ crescendo preferencialmente na orientação (001). Foi verificado um processo de relaxação dielétrica, cuja energia de ativação é sensível às transições de fase magnéticas. A natureza da fase magnética de baixa temperatura e a estabilização de uma fase ferroelétrica também são discutidas.

Este trabalho mostra como a engenharia de deformação pode ser usada para ajustar a estrutura e as propriedades de óxidos fortemente correlacionados.

Palavras-chave: Engenharia de deformação, crescimento epitaxial, filmes finos, perovskite tetragonal, ferroeletricidade.

Abstract

Among the rare earth perovskites, the orthorhombic $GdMnO_3$ probes to be an interesting material to probe the concept of properties for demand, as it presents strong correlation between spin-orbital-lattice degrees of freedom which can be tailor through strain engineering. By epitaxial strain, structure can change and new and unexpected phases and physical properties in thin films arise.

In this thesis, we present an experimental study of the effect of strain in the low properties of non-relaxed $GdMnO_3$ thin films deposited onto (001)- and (110)- oriented $SrTiO_3$ substrates by means of RF magnetron sputtering. The structure, microstructure, dielectric and magnetic properties of the as-prepared films were investigated in detail.

According to substrates orientations, two different crystallographic classes were observed, exhibiting different properties, evidencing the important influence of substrate orientation on the microscope interactions underlying both magnetism and dielectric properties.

The XRD results revealed that the $GdMnO_3$ thin films deposited onto (001)- $SrTiO_3$ substrates exhibit a tetragonal symmetry with its axis perpendicular to the film surface in which the basal lattice parameters are imposed by the cubic structure of the substrate. The emergence of a spontaneous electric polarization below ~ 31 K points to the stabilization of an improper ferroelectric phase at low temperatures, which is not observed in bulk $GdMnO_3$.

The $GdMnO_3$ thin films deposited onto (110)- $SrTiO_3$ substrates exhibit an epitaxial strained orthorhombic symmetry and grow preferably in off-plane (001) orientation, wherein the basal lattice parameters are strained by the substrate lattice, imposing a twinned α-phase on the GMO thin films in (100) direction that evolves to a γ-phase that grows preferably in (001) orientation. A dielectric relaxation process was ascertained, whose activation energy is sensitive to the magnetic phase transitions. The canted nature of the low temperature magnetic phase and the stabilization of a ferroelectric phase are also discussed.

This work shows how strain engineering can be used to tailor the structure and properties of strongly correlated oxides.

Keywords: Strain-engineering, epitaxial growth, thin films, tetragonal perovskites, ferroelectricity.

Table of Contents

List of Tables

List of Figures

List of Abbreviations

AFM	ANTIFERROMAGNETIC
AFM-3D	ATOMIC FORCE MICROSCOPY- 3D
B	MAGNETIC FIELD
DC	DIRECT CURRENT
EDS	ENERGY DISPERSIVE SPECTROSCOPY
FC	FIELD COOLING
FM	FERROMAGNETIC
GMO	$GdMnO_3$
IDES	INTERDIGITAL ELECTRODES
M	MAGNETIZATION
PLD	PULSE LASER DEPOSITION
RF	RADIO FREQUENCY
RSM	RECIPROCAL SPACE MAP
SEM	SCANNING ELECTRON MICROSCOPY
SQUID	SUPERCONDUCTING QUANTUM INTERFERENCE DEVICE
STO	$SrTiO_3$
T	TEMPERATURE
TEM	TRANSMISSION ELECTRON MICROSCOPY
TSDC	THERMALLY STIMULATED DEPOLARIZATION CURRENT
XPS	X-RAY PHOTOELECTRON SPECTROSCOPY
XRD	X-RAY DIFFRACTION
XRR	X-RAY REFLECTOMETRY
YSZ	YTTRIA-STABILIZED ZIRCONIA
ZFC	ZERO FIELD COOLING

Introduction

The whole current technology is based on the discovery of new materials with (multi)functional properties that allow improving the existing functionalities or open doors to new (multi)functionalities. To achieve this new technological level, the current research has been focused on materials exhibiting coupling between different degrees of freedom. The knowledge concerning the microscopic mechanisms underlying the coupling between orbital, electronic, spin and lattice degrees of freedom, occurring in transition metal oxides with perovskite structure, has provided a significant advance in the discovering of new physics and the design of (multi)functional devices. These materials, classified as strongly correlated systems are sensitive to external parameters, which when meeting specific requirements, stabilize new phases with different properties.

Strain engineering has been an interesting and powerful way to control the physical properties of materials at the nanoscale level, such as thin films that can withstand tensile or shear stresses up to a significant fraction of their ideal strength. The structural distortions induced by epitaxial strain, change the original state of atomic bonds by elongating or shortening bond lengths and bond angles, being able to tailor structural parameters towards stabilizing new crystallographic structures and thermodynamic phases, not observed in the bulk materials, thus fostering new functionalities in the working temperature range of interest. To attain significant effects of strain on the physical properties, in addition to a good connectivity between film and substrate, a strong coupling between lattice and other degrees of freedom, like electronic, charge, spin and orbital, is required. In this regard, rare-earth manganites (RMnO$_3$, R a trivalent rare-earth cation) are attractive candidates for strain-engineered designed properties as towards fulfill those requests.

Rare-earth manganites exhibit a large set of physical properties, including colossal magnetoresistance, charge-orbital ordering, different magnetic structures and multiferroicity. As the magnetism and transport properties of orthorhombic RMnO$_3$ scale with the Mn-O-Mn bond angle, which defines the balance between competitive electronic and magnetic interactions, these materials are highly sensitive to external parameters which can distort the crystallographic structure, like hydrostatic pressure, applied magnetic/electric fields and epitaxial strain. Among rare-earth manganites exhibiting orthorhombic *Pnma* symmetry at room conditions, GdMnO$_3$ is especially interesting to strain-engineering its properties, as the magnitude of the Mn-O-Mn bond angle sets at

the border line between the value for $TbMnO_3$ and $DyMnO_3$ spontaneous multiferroics, and the $EuMnO_3$ magnetic-field induced multiferroic. In this scope, several studies have been undertaken in doped $GdMnO_3$ bulk samples, and significant progresses have been made. However, few works have addressed the properties of totally strained stoichiometric $GdMnO_3$ thin films. Numerous open questions associated with the role of strain, defects, interface, microstructure, and heterogeneity at different length scales on the physical properties of this material are still waiting answers.

This thesis aims at unravelling the role played by strain-engineering in tuning the physical properties of $GdMnO_3$ thin films deposited onto (100) and (110)-oriented $SrTiO_3$ substrates. The results evidence the noteworthy effect of the epitaxial strain induced by substrate orientation on the structural distortions of $GdMnO_3$ thin films, and how strain mediated supplementary distortions influence the macroscopic properties.

This thesis is organized in four main chapters. The first chapter presents the literature review concerning the state-of-the-art of the strain-engineered properties in the most outstanding strong correlated materials, an overview of the physical properties of the $GdMnO_3$ crystals, ceramics, and thin films, whilst looking at the effects of external parameters on their properties. This chapter ends with the main objectives and a methodology. The techniques used for the thin films preparation and their structural, physical and macroscopic characterization are described in the second chapter. In chapter 3, the experimental results obtained in this thesis on non-relaxed strained $GdMnO_3$ thin films are described in order to highlight the effect of orientation-dependent strain on their structure and macroscopic properties. The thesis closes with the main conclusions and future work.

1. State of the Art

1.1. Strain-engineering: Modifying properties in Low-dimensional Systems

Strain-engineering refers to the degree of deformation that a low dimensional system withstands due to the mechanical interactions with host matrix (that can be also a single crystalline oriented substrate) and its effects on its properties. This approach has been widely used to tune optical properties of semiconductors, to induce novel phases as ferroelectricity in the well-known quantum paraelectric $SrTiO_3$ (STO), or to stabilize specific polymorphous of $BiFeO_3$ and thus creating and manipulating particular functionalities [1][2].

Contrarily to hydrostatic pressure, strain is direction dependent. This is the case of $PbZr_xTi_{1-x}O_3$ film in which compressive strain forms monodomains structures, while tensile strain forms multidomain structures [3].

In epitaxial (non-relaxed) films deposited onto oriented crystalline substrates, strain arises from the lattice-mismatch between materials, which depends on the substrate orientation. Moreover, lattice expansion coefficients of both substrate and film are generally different and temperature dependent, and thus the concomitant thermally induced strains will provide opening opportunities for temperature-controlled properties [3].

Strain-engineering has been applied to many simple perovskite oxides with general formula ABO_3. Figure 1 (a) shows a scheme of the simple perovskite structure. The ideal ABO_3 perovskite structure is cubic with space group $Pm\bar{3}m$. The primitive unit cell can be described as follows. The A- cations occupy the vertices of the cubic primitive cell, and are 12-fold coordinated by oxygen anions, while occupy the centers of the cubic faces. The B- cations are in the cubic cell centre, with 6-fold coordinated by oxygen anions.

However, this structure is scarcely found at room conditions because the ionic size of A- or B- cations does not match the ideal tolerance factor [4]:

$$t = \frac{R_A + R_0}{\sqrt{2}\,(R_B + R_0)} \tag{1.1}$$

where R_A, R_B and R_0 are the ionic radii of the A-, B- cations and oxygen anions, respectively. Due to this ionic radius mismatch, perovskites adopt distorted structure, lowering the crystal symmetry.

In this thesis, we are interested in the orthorhombic *Pnma* structure, exhibited by *R*MnO_3, R = La – Dy at room conditions. This structure is shown in Figure 1 (b) and is obtained from the ideal $Pm\bar{3}m$ structure due to the condensation of *B*O_6 octahedra rotation modes. It can be described as a 3D network of rotated corner-sharing *B*O_6 octahedral, while the A- cations occupy the dodecahedral site, but with 8-fold coordination.

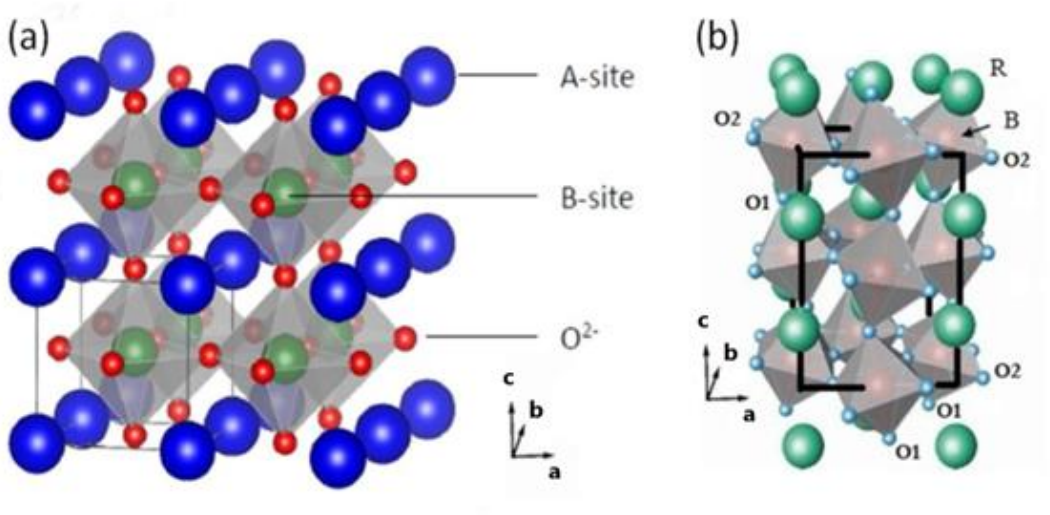

Figure 1: (a) Structure of an ideal cubic perovskite with $Pm\bar{3}m$ symmetry and general formula *ABX*$_3$ (the primitive cell is also evidenced) (b) Distorted perovskite structure with *Pnma* symmetry resulting from the octahedra tilting [5].

The properties of many orthorhombic perovskites scale with the O-B-O bond angle, which decreases from the straight 180º of the $Pm\bar{3}m$ structure due to the *B*O_6 octahedra rotation occurring in this *Pnma* structure. So, strain-engineering these octahedral rotations has been carried out, wherein the effect of strain on the substrate-induced rotation patterns, can yield significant symmetry changes [6], [7] [8]. These changes should convey the mechanisms required to the emergence of unprecedent physical properties. As a representative example compressive $SrRuO_3$ films on (110) $NdGaO_3$ substrate (-1.7%) undergoes a rotation pattern of a tetragonal phase, exhibiting a perpendicular magnetic anisotropy and a reduced Curie temperature, while the tensile

strained $SrRuO_3$ films on (001) $KTaO_3$ substrate (~ 1.5%) shows a rotation pattern characteristic of orthorhombic bulk $SrRuO_3$ with no relevant changes in Curie temperature or magnetic anisotropy [9]. However, Kan *et al.* [6] report stabilized tetragonal $SrRuO_3$ thin films coherently grown on (110) $GdScO_3$ substrates under tensile strain (~ 1.0%), with a ferromagnetic transition temperature T_C = 100 K lower than the films on $KTaO_3$ or bulk $SrRuO_3$ (T_C ~ 160 K) [6]. These results are correlated to the different octahedral response to compressive and tensile strains and reveal a strong dependence of the electronic and magnetic properties on the substrate-induced epitaxial strain [6].

In the following, we shall review two outstanding case-studies of strain-engineered films: the case of $SrTiO_3$ regarding the stabilization of ferroelectric phase and its electronic transport properties, and the case of $TbMnO_3$, concerning the room temperature ferroelectricity in the hexagonal phase. Many other examples can be found in the literature, but the examples here presented clearly evidence the high impact of strain-engineering to control properties through structure.

1.1.1. Strain-engineered $SrTiO_3$

$SrTiO_3$ is the prototype for simple perovskites structure, as its tolerance factor at room conditions is very close to the ideal value (t_{ideal} = 1 ; t_{STO} = 1.009) [4].

At room conditions, $SrTiO_3$ is cubic $(Pm\bar{3}m)$ and paraelectric, exhibiting good insulating properties [10]. At T_C = 105 K, it undergoes an antiferrodistortive phase transition (AFD), triggered by the octahedral rotations, although it retains a centrosymmetric structure (see Figure 2) [11]. As its structural instabilities are of zone border, the transition is accompanied by cell doubling and $SrTiO_3$ become tetragonal $P4/mmm$ below 105 K keeping its paraelectric properties [12]. As temperature approaches 0 K, the electric permittivity monotonously increases, but never reaches a maximum, meaning that $SrTiO_3$ does not transit into a ferroelectric phase at finite temperature [13]. Quantum fluctuations have been ascribed to the incipient ferroelectric character of $SrTiO_3$ [14]. Indeed, experimental results involving doping effects, have shown that ferroelectricity can be stabilized at finite temperatures. This is the case of $Ca_xSr_{1-x}TiO_3$ (X= 0.009) [15],[16].

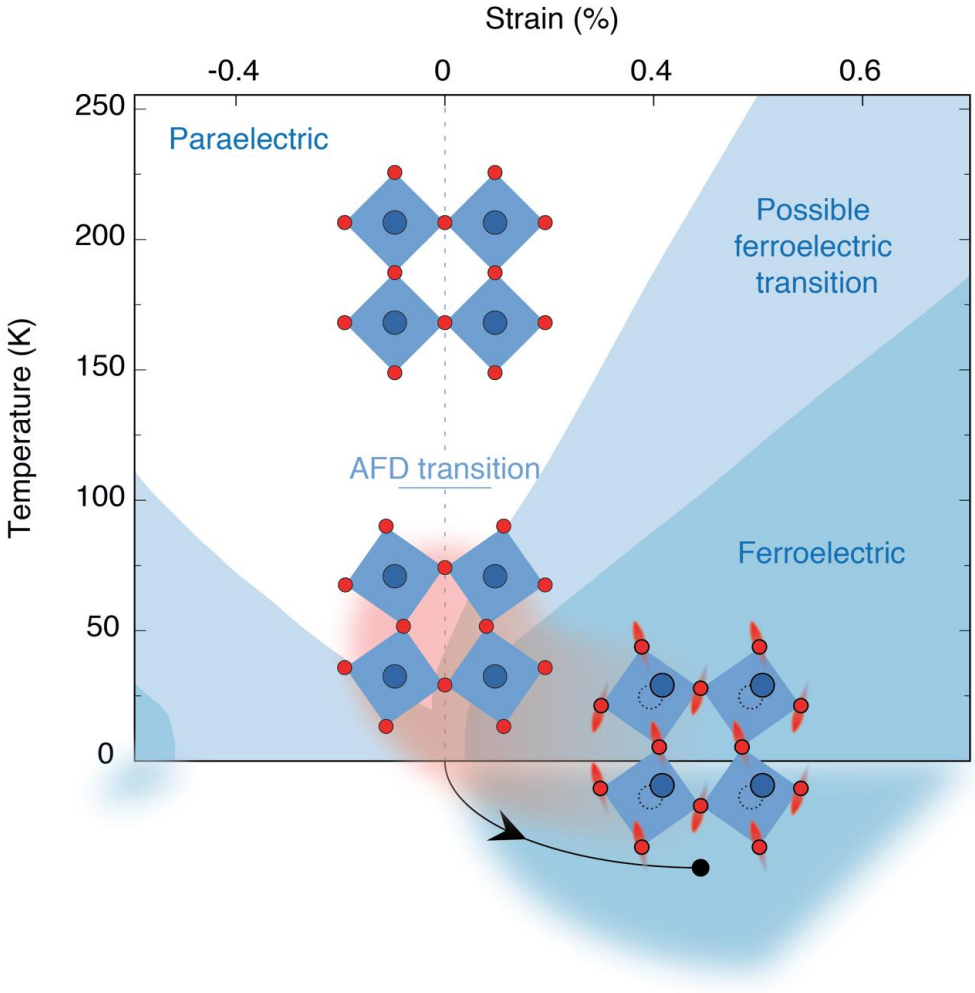

Figure 2: Strain-phase diagram and dynamical ferroelectricity of $SrTiO_3$ in function of temperature. Adapted from [17].

Figure 2 shows that the stabilization of the ferroelectric phase in $SrTiO_3$ thin films can also be achieved by mechanical stress and the Curie temperature increases with growing values of applied strain. It was first predicted and experimental demonstrated that there is a correlation between epitaxial strain and the electronic properties of $SrTiO_3$ [18]–[22]. One of the best parameters to evidence the stabilization of the ferroelectric phase in epitaxial $SrTiO_3$ film is the maximum value of the electric permittivity curve ε'(T), which gives access to the Curie temperature T_C [13].

Figure 3 (a) shows the temperature dependence of the electric permittivity of unstrained $SrTiO_3$ and strained $SrTiO_3$ deposited onto (110)-oriented scandates substrates (C-$SrTiO_3$/$DyScO_3$, D-$SrTiO_3$/$TbScO_3$ and E-$SrTiO_3$/$GdScO_3$), evidencing a large impact that epitaxial strain has on the Curie temperature, shifting the transition temperature of epitaxial $SrTiO_3$ films in a range of values between 280 K and 370 K depending on the amount of strain impose by the substrate.

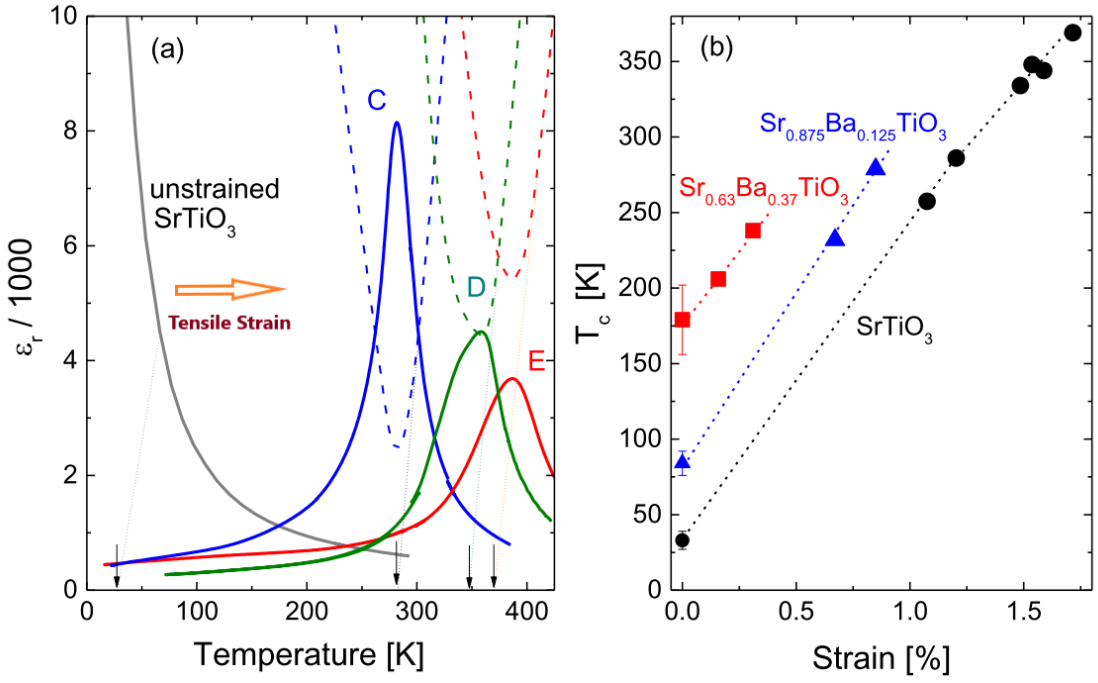

Figure 3: (a) Examples of the temperature dependence of the electric permittivity of unstrained $SrTiO_3$ and strained $SrTiO_3$ deposited onto (110)-oriented scandates substrates (C-$SrTiO_3$/$DyScO_3$, D-$SrTiO_3$/$TbScO_3$, E-$SrTiO_3$/$GdScO_3$), (b) resulting strain dependence of the Curie–Weiss temperature for unstrained and epitaxially strained $Sr_{(1-x)}Ba_{(x)}TiO_3$ (x = 0; 0.125 and 0.37) films deposited onto $DyScO_3$ (110)-oriented substrates. The dashed and dotted lines in (a) show the temperature dependence of the inverse permittivity and the Curie–Weiss fit (linear extrapolations), respectively. The arrows depict the resulting Curie–Weiss temperatures [13].

Figure 3 (b) shows the resulting strain dependence of the Curie–Weiss temperature for unstrained and epitaxially strained $Sr_{(1-x)}Ba_{(x)}TiO_3$ (x = 0; 0.125 and 0.37) films deposited onto $DyScO_3$ (110)-oriented substrates in which the dashed lines allow us to conclude that the slopes (ΔT_c / ΔStrain) for the three different concentrations of *x,* presents similar values and the T_c shows a near-linear increase with the strain for each stoichiometry. As it can be seen, epitaxial strain stabilized the ferroelectric phase of both $SrTiO_3$ and mixed system (Sr, Ba) TiO_3, pushing the critical temperature towards 550 K, which is an outstanding result as $SrTiO_3$ becomes ferroelectric at room temperature for high enough strain (ε > 1%).

Although the result described above has large impact and stimulated the strain engineering in other materials, this approach is not without its problems, due to the lack of ability to produce large and continuously variable strain states. Very recently, R. Xu *et al.* have published an experimental report on the dynamic strain-induced ferroelectricity in $SrTiO_3$ by laminating freestanding oxide films onto stretchable polymer substrate [23]. The authors have demonstrated the stabilization of the ferroelectric phase in $SrTiO_3$ with 2.0 % uniaxial tensile strain, with evidence for 180° ferroelectric domains at room temperatures and having extrapolated T_C ~ 400 K (see Figure 4). It should be noted that

these results on membranes of $SrTiO_3$ are similar to those of epitaxial $SrTiO_3$ films presented in Figure 3 (b), thus showing that strain can shift T_C towards, or even beyond room temperature.

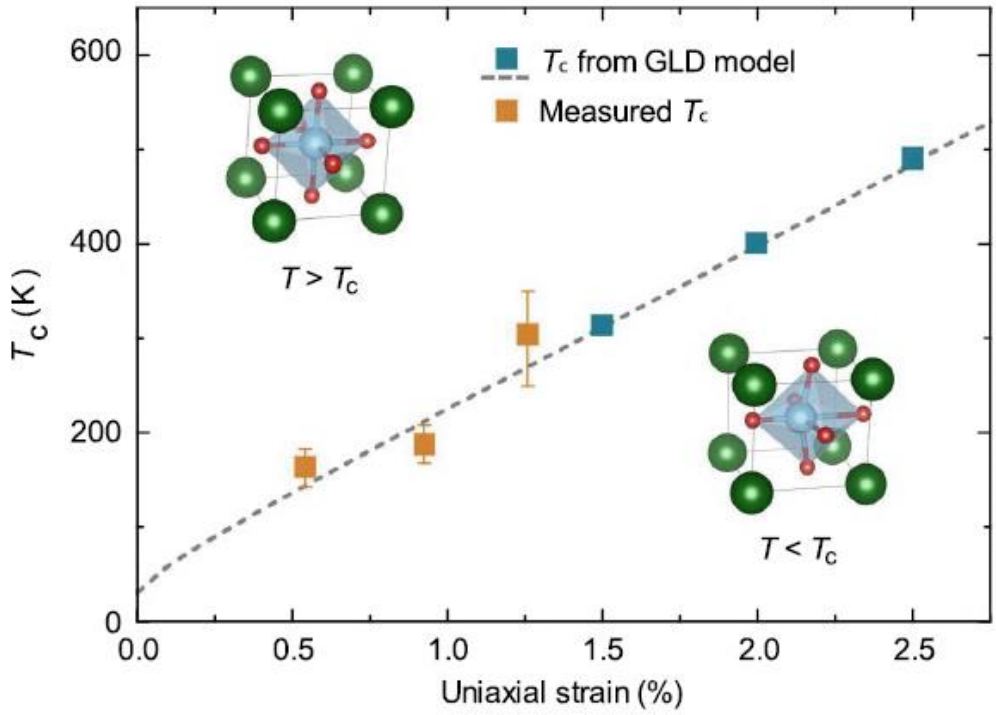

Figure 4: Tc plotted as a function of uniaxial strain directly measured from the optical second harmonic generation (SHG) measurements of $SrTiO_3$ membranes, as well as high temperature extrapolations of the Ginsburg–Landau–Devonshire model (GLD). Error bars represent the standard deviation [23].

Strain engineering has been also successfully applied to change the band gap of $SrTiO_3$ [24]. Stoichiometric, undoped, and unstrained $SrTiO_3$ is a band insulator with an indirect band gap energy of 3.25 eV, and a direct gap of 3.75 eV [25]. The valence band is mainly associated with O-*2p* states, while the conduction band is originated by Ti-*3d* states. Doping $SrTiO_3$ with trivalent ions (Al^{3+}, La^{3+}) on the Sr-site, and with pentavalent ions (Nb^{5+}, Ta^{5+}) on the Ti-site, dramatically change its band structure [26], [27]. However, this approach easily induces defects based on non-stoichiometry, namely oxygen vacancies which play an important role on the electrical conductivity [10], [28]. Strain also boosts the formations of oxygen vacancies, their mobility, and the conductivity of $SrTiO_3$ thin films. However, strain also modifies the base structure of $SrTiO_3$ and affects the occupation of the O-*2p* like bands, contributing to the density of states at the Fermi level and enhancing conductivity in the direction of tensile strain. Thus, with adequate strain, epitaxial $SrTiO_3$ can exhibit semiconductive-like properties, making this material under strain ideal for many electronic applications [29]–[31].

1.2. Tunning properties in epitaxial strained $TbMnO_3$

The next example approaches the topic addressed in this thesis. Bulk orthorhombic $TbMnO_3$ is one of the best known intrinsic multiferroic material at low temperature [32]–[34]. Ferroelectricity arises from the cycloidal modulated spin structure, due to the inverse Dzyaloshinskii-Moriya interaction [35]. However, $TbMnO_3$ can also crystallize on the hexagonal structure ($P6_3cm$), exhibiting ferroelectricity at high temperature, typically below T_C = 600 K [36]. The problem is that hexagonal $TbMnO_3$ (h-$TbMnO_3$) has to be prepared using extreme conditions (high pressure (up to 10 GPa) and high temperature ~ 1600 K) preventing the processing of enough large samples [33]. This hinderness led to an intense research to stabilize the hexagonal structure in $TbMnO_3$ epitaxial thin films.

Epitaxial strained h-$TbMnO_3$ thin films were successfully deposited onto Pt (111) / Al_2O_3 (0001) substrates, with 20 unit cells (~ 23 nm) thickness, by PLD [36]. Recent experimentally characterization of these films through I-V measurements and local current mapping of the h-$TbMnO_3$ film, after poling with +6 V and -6 V tip bias, has revealed semiconductive and ferroelectric properties at room temperature (see Figure 5), clearly demonstrating the possibility to change both structure and properties of $TbMnO_3$ at room conditions by strain-engineering.

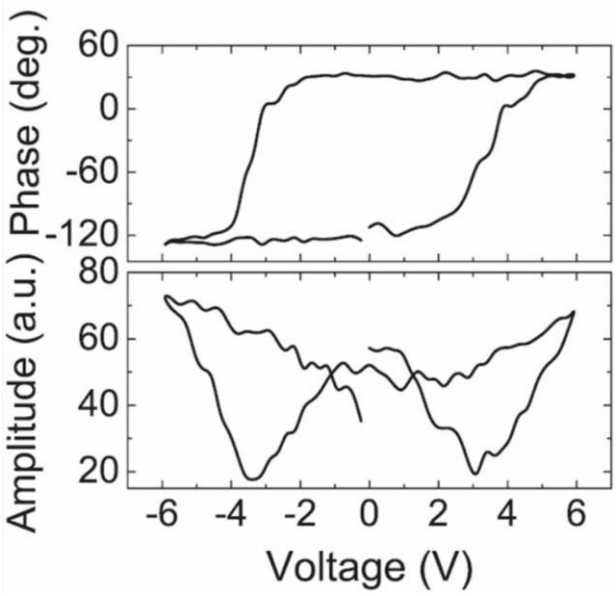

Figure 5: Testing of ferroelectric switching using local PFM hysteresis loops of the h-$TbMnO_3$/Pt(111)/Al_2O_3 film [36].

After this study, Noheda *et al.* published a report on $TbMnO_3$ thin film deposited onto TiO_2 terminated (001)-oriented $SrTiO_3$ substrates [37]. The films were found to grow under compressive strain and exhibit the preferential grow direction (001) in *Pnma* setting. In very thin films (2 nm, ~ 3 unit cells), the $TbMnO_3$ exhibits tetragonal symmetry,

while for thicker films (17 - 80 nm, 25 - 125 unit cells) they remain orthorhombic as in bulk (see Figure 6).

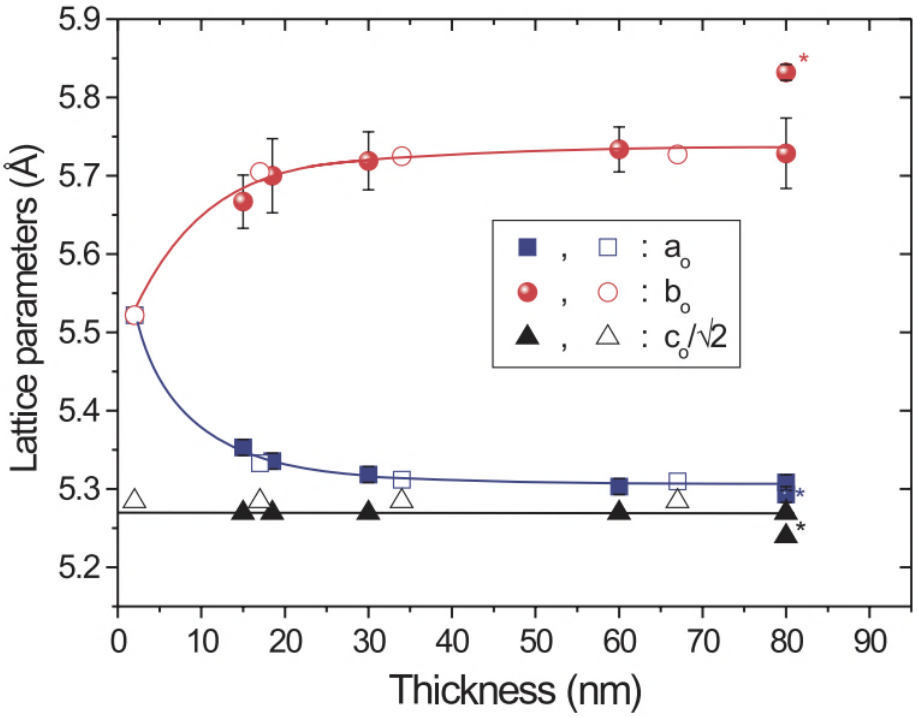

Figure 6: Lattice parameters (a_o, b_o, $c_o/\sqrt{2}$) as a function of thickness for films of $TbMnO_3$ grown on $SrTiO_3$ with pO_2 = 0.9 mbar (filled symbols) and 0.25 mbar (open symbols). In the 80 nm film, the symbols marked with a star corresponds to the bulk orthorhombic unit cell. The lines are guides to the eye [37].

Interesting is the stabilization of a ferromagnetic phase and the disappearance of ferroelectricity below 40 K [38]. The stabilization of a ferromagnetic phase in compressed $TbMnO_3$ films has been tentatively interpreted by Noheda *et al.* as consequence of magnetoelectric coupling [37]. However, antiferromagnets are piezomagnetics and the epitaxial strain could induce a magnetic moment ordering in the films [38]. Moreover, the linear magnetostriction in antiferromagnets is usually several orders of magnitude larger [39]. As the stress in the films was estimated to be 2 x 10^8 N/m^2, and taking the Young Modulus of 20 GPa [40], the magnetization values reported are compatible with the piezomagnetic coefficient of 10^{-10} m/A. However, this value is smaller than the reported magnetostrictive values in bulk and one order of magnitude larger than typical intrinsic piezomagnetic coefficient in antiferromagnets [39]. So, a final conclusion regarding the origin of ferromagnetic behavior is still unknown. Finally, the epitaxial strain prevents other low-temperature magnetic transition in $TbMnO_3$ films.

Although not exhaustive, these two cases clearly show that strain-engineering is an interesting way to modify material properties at the nano-scale level systems.

1.3. Physical properties of $GdMnO_3$

1.3.1. Orthorhombic $RMnO_3$ phase diagram - an overview

After a very short review of two outstanding cases, in the following, we shall focus on the characterization of $GdMnO_3$ bulk and thin films, which will be the subject of this thesis. Orthorhombic rare-earth manganites, hereafter designated further in the text as O-*R*MnO_3, are structurally characterized by the so-called $GdFeO_3$-type distortion involving the in-phase and anti-phase tilts of the MnO_6 octahedra, yielding at room conditions a symmetry lowering from the ideal $Pm\bar{3}m$ to the *Pnma* structure, associated with a fourfold increase of the primitive unit cell (Z = 4) (see Figure 1 (b)) [41][42][43]. The in-phase tilt occurs around the $[010]_{pc}$ and the anti-phase tilt around the $[101]_{pc}$ pseudocubic axes, with respect to the ideal $Pm\bar{3}m$ perovskite structure [41]. The octahedral tilts internally deform the MnO_6 octahedra, emerging two different Mn-O bond lengths [41]. Moreover, the Jahn-Teller activity of the Mn^{3+} cation induces additional deformation in the MnO_6 octahedra that yields three different length Mn-O bond pairs [44]. This structural symmetry reduction affects the symmetry constrains in the position of each atom in the primitive cell, which can be described by the corresponding Wyckoff positions (see Table 1).

Table 1: Wyckoff positions for the $Pm\bar{3}m$ (top) and the *Pnma* (bottom) phase of the *A*BO_3 perovskite structure.

Atom	Multiplicity	Wyckoff positions	Site symmetry
A	1	a	$m\bar{3}m$
B	1	b	$m\bar{3}m$
O	3	c	$4/mmm$

Atom	Multiplicity	Wyckoff positions	Site symmetry
A	4	c	m
B	4	b	$\bar{1}$
O1	4	c	m
O2	8	d	1

In the *Pnma* phase, the Mn-cation remains at the symmetry inversion site, while the rare-earth cation now occupies a site with a mirror plane symmetry, with two unconstrained coordinates (x and z). The oxygens are located at two different sites. The two O1 (the apical oxygens of the octahedron) have the same symmetry as the rare-earth cation, occupying the same xz symmetry plane. The four O2 (the equatorial oxygens of the octahedron) are sited in general positions, without any constrains on their coordinates. It is worth to mention that due to these oxygen displacements, the rare-earth cation forms

8 shorter bonds and 4 longer bonds with the oxygens. Thus, its coordination is reduced from 12 to 8, which must be considered when calculating the tolerance factor.

The properties of O-*R*MnO_3 are strongly dependent on the degree of lattice distortion. This can be achieved by changing the R^{3+} cation, which means a changing of the dodecahedron dimensions and consequently octahedra tilt angle variations. As R^{3+} cation size for the 8th fold coordination decreases (La → Dy), the octahedra tilt angle increase; i.e., the Mn-O-Mn bond angle reduces. In this way, the electronic orbital overlapping between adjacent Mn^{3+} and O^{2-} ions is changed and, consequently, the superexchange integrals. In O-*R*M*n*O_3 compounds, nearest neighbors antiferromagnetic interactions and next nearest neighbors ferromagnetic interactions of Mn^{3+} ions compete, and the balance between the competitive magnetic interactions underlies the phase sequence for each compound from R = La to Dy [45]. The interplay between lattice and magnetism yields the possibility to tailor the magnetic properties in O-*R*M*n*O_3, which can be further used to accomplish a desired physical behavior [46], [47].

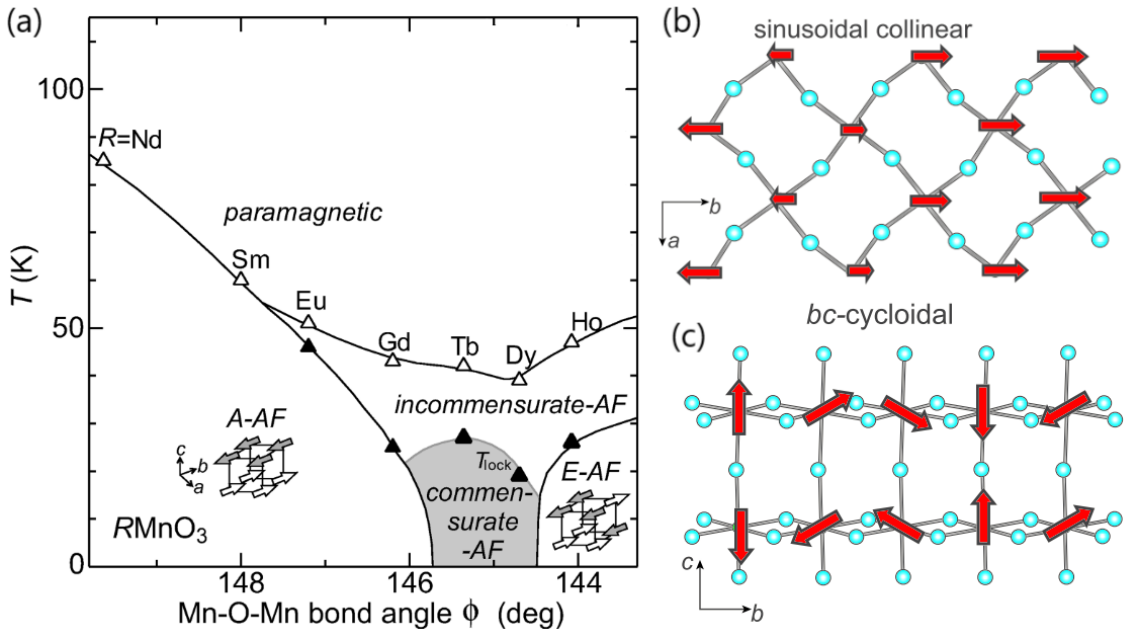

Figure 7: (a) Experimental magnetic phase diagram of O-*R*MnO_3 (*R* = Nd, Sm, Eu, Gd, Tb, Dy and Ho) as a function of Mn-O-Mn bond angle φ [48], (b) ordering of the collinear-sinusoidal incommensurate and (c) cycloidal commensurate antiferromagnetic spin structures of O-*R*MnO_3 (*Pnma* setting) [49].

Above 1000 K, all the O-*R*MnO_3 compounds present an orbital ordering transition associated with the stabilization of the Jahn-Teller distortion [50] . Figure 7 (a) shows the low-temperature magnetic phase diagram of O-*R*MnO_3, with *R* = Nd to Ho [48]. At room temperature, they are all paramagnetic and paraelectric. Below room temperature, for *R* = La to Sm, there is a single-phase transition between T_N = 140 K and 62 K, respectively,

from the paramagnetic state to a canted A-type antiferromagnetic phase [45]. For *R* = Eu and Gd, two phase transitions are observed. One at T_N, from the paramagnetic to a collinear-sinusoidal incommensurate antiferromagnetic phase along the *b*-axis (see Figure 7 (b)), and another at lower temperature to a canted A-type antiferromagnetic phase. As the A-site ionic radius further decreases, for *R* = Tb and Dy, besides the collinear-sinusoidal incommensurate antiferromagnetic phase, at T_{lock}, around 27 K and 20 K, respectively, the spin ordering changes into a cycloidal commensurate antiferromagnetic structure on the *bc*-plane (Figure 7 (c)) and the magnetic modulation wave vector (q_m, 0, 0) is locked into a fixed value q_m = 0.27 and 0.38, respectively. The structural modulation vector k_l presents a similar temperature dependence and is given by: $k_l = 2q_{mag}$ for the $TbMnO_3$ case (see Figure 8). This magnetic structure allows a spontaneous ferroelectric ordering in the plane of the *bc*-cycloidal along the *c*-axis, which can be explained through different models, via the Dzyaloshinskii-Moriya interaction mechanism [35], [51], [52].

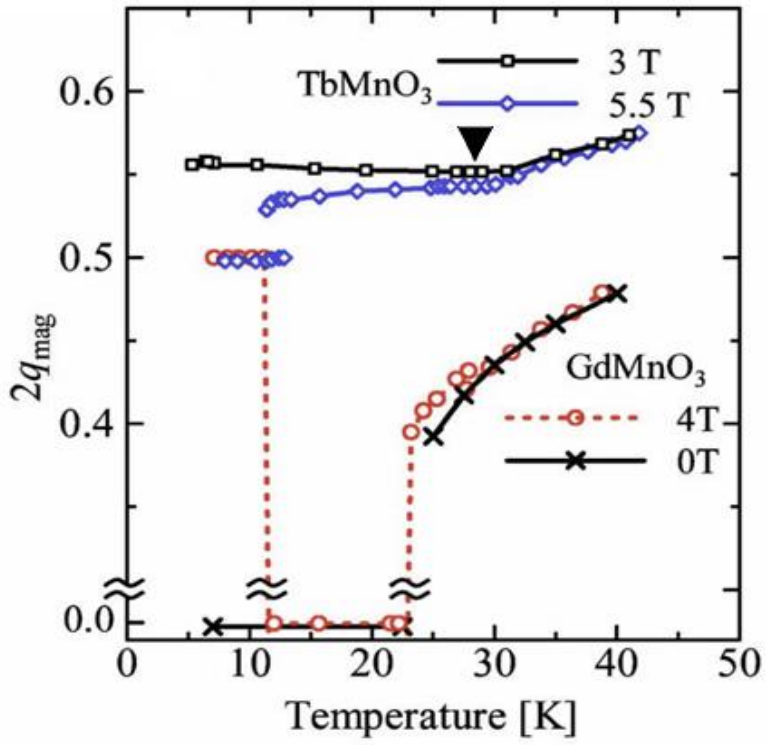

Figure 8: Change in spin modulation wave vectors (q_{Mn} 1 0) of $GdMnO_3$ ($TbMnO_3$) with temperature in magnetic fields of 0 and 4 T (3 and 5.5 T). A solid triangle indicates the T_{lock} of $TbMnO_3$ [53].

The applied magnetic field has a strong effect on the spin structure of both $GdMnO_3$ and $TbMnO_3$. Figure 8 shows the temperature dependence of the modulation vector q_{mag} of $GdMnO_3$ and $TbMnO_3$, measured at zero and 4 T applied magnetic field ($GdMnO_3$) and at 3 T and 5.5 T ($TbMnO_3$), along *c*-axis (*Pnma* setting). As the temperature decreases,

under an applied magnetic field of 4 T, $GdMnO_3$ q_{mag} (T) evidences for a successive phase transition. It can be seen from Figure 8, that q_{mag} (T) for $GdMnO_3$ is weakly dependent on the magnetic field above 12 K. The appearance of commensurate spin structure in the magnetic field below 12 K has interpreted as a manifestation of the onset of a ferroelectric phase transition under the applied external field [53]. Concerning $TbMnO_3$, no significant changes were reported on the temperature dependence of the q_{mag} (T) measured under 3 T and without an external field evidencing that a 3 T magnetic field is not enough to promote changes on the phase sequence of $TbMnO_3$. Under a 5.5 T, q_{mag} (T) deviates from its value at 3 T, and a lock-in transition is observed below 10 K, with a coexistence of a incommensurate and commensurate modulation between 10 - 13 K. Above 13 K the commensurability disappears, corresponding very well to the polarization flop phenomenon from P//b to P//a [34]. Although changes on the phase sequence can be obtained from both chemical substitution or applied fields, the required substitution level or magnetic field strength are large. As we have previously discussed in the last section for the case of $TbMnO_3$, we will present in the following section, for $GdMnO_3$, strain engineering as suitable to induce changes in much large extent in these materials.

Despite the strong interplay between lattice and spin degrees of freedom in $GdMnO_3$, to the best of our knowledge, no studies concerning the high-pressure effect on magnetism and ferroelectricity in $GdMnO_3$ were published. Only the effect of extreme pressure (P > 40 GPa) was studied looking at the lattice structure [54]. Actually, a first order structural phase transition was reported at P_c ~ 50 GPa. Even in this regard, no consensus about the high-pressure structure was achieved. While Chualong Lin *et al.* have reported an isostructural phase transition with 5% volume reduction [55], J. Oliveira *et al.* have reported a structural and insulator-to-metal phase transition from *Pnma* structure to a metrically cubic one, described by the $P2_13$ space group [56].

1.3.2. Magnetoelectric coupling in $GdMnO_3$

A large consensus is found concerning the spontaneous magnetoelectric effect in $TbMnO_3$ and $DyMnO_3$ [48], [57], [58]. $EuMnO_3$ is known to exhibit a magnetic field induced transition into a ferroelectric ground-state, for intense magnetic fields with strength larger than 20 T at temperatures below 40 K [35], [48], [51], [52], [59]. Nevertheless, contradictory results regarding the spontaneous ferroelectric phase have been published in $GdMnO_3$. Following Kimura *et al*., $GdMnO_3$ exhibits a spontaneous ferroelectric polarization along the *b*-axis, between 5.1 K and 8.2 K, even in the absence

of a magnetic field [58]. When a magnetic field is applied along the *c*-axis, the temperature range of stability of the ferroelectric phase increases up to 15 K (see Figure 9 (a)), stabilizing a commensurate magnetic structure similar to the one found in $TbMnO_3$ and $DyMnO_3$ [58]. Still, Noda *et al*. reported a finite polarization below 13 K along the *b*-axis of $GdMnO_3$, in the absence of an external magnetic field, and also, as a function of applied magnetic field along the *a*-axis. From these measurements, a (T, B) magnetic phase diagram was drawn, which is partially shown in Figure 9 (b) [58]. For magnetic fields between 0.25 and 0.5 T, a re-entrant ferroelectric phase is found, which is only stable down to the lowest temperatures above 1 T. Until 10 T, the ferroelectricity is always found along the *b*-axis (i.e. *bc*-cycloidal spin structure), without any possibility to be reoriented.

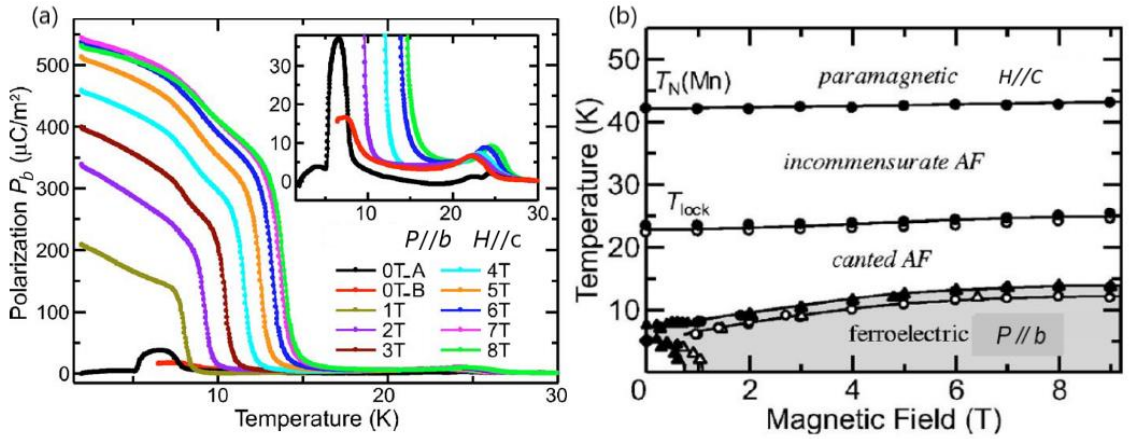

Figure 9: (a) Temperature profiles of electric polarization along the *b*-axis at various magnetic fields（up to 8 T) along the *c*-axis for a $GdMnO_3$ crystal (*Pnma* setting). The inset shows a magnified view. (b) (T, B) magnetic phase diagram of $GdMnO_3$. Except for the data denoted by black dots（0T_A, ~200 V/mm), all the data were taken at zero electric fields after poling the crystal [58].

However, Arima *et al.* claim that $GdMnO_3$ single-crystal is not ferroelectric in the absence of an applied magnetic field [53]. They have found the ferroelectric phase (P//b) induced by the application of a magnetic field at low temperatures which is characterized by commensurate lattice modulation along the orthorhombic *c*-axis. It is worth to mention that the reported values of the electric polarization were obtained after cooling the samples under a rather high poling electric field, usually having values of the order of magnitude of several kV/m. Such high values of poling fields can induce contribution to the electric polarization, other than the ferroelectric one.

1.3.3. $GdMnO_3$ thin films

In the following the main results reported in $GdMnO_3$ thin films will be addressed. Below we present a critical review of the results obtained in thin films of $GdMnO_3$ deposited by different methods on different substrates.

$GdMnO_3$ thin films have been deposited onto different substrates by using both chemical and physical routes [46], [60]–[67]. Up to now, two different crystal symmetries have been reported for $GdMnO_3$ thin films. Orthorhombic $GdMnO_3$ thin films (*Pbnm* space group) have been the most frequently obtained at room temperature [46], [63]–[67]. Epitaxial $GdMnO_3$ thin films, with 10 nm thickness, were successfully deposited on oriented (010)-$YAlO_3$ substrates by pulse laser deposition method which grows along *b* axis [46], [64]. These orthorhombic films (*Pbnm* setting) exhibit a polar phase below 30 K (*H*=0), with a remnant polarization of about ~ 1 μC/cm^2 at 10 K (see Figure 10) that increased 250 times relatively to the value of spontaneous polarization of the bulk $GdMnO_3$ ~ 0.004 μC/cm^2 (see Figure 9 (a)) [46] [65].

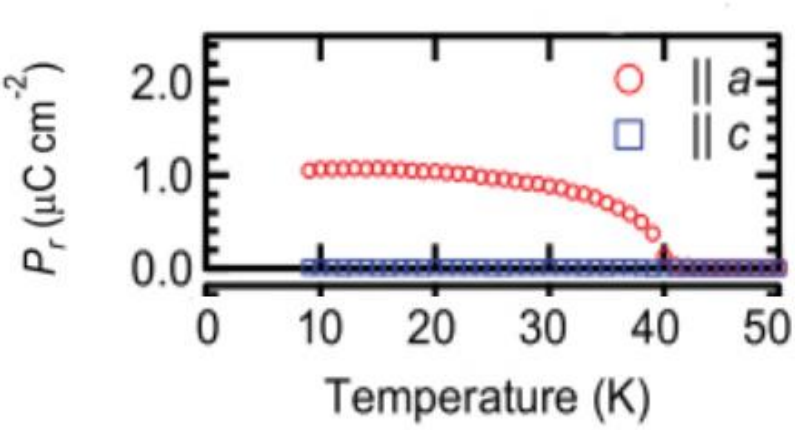

Figure 10: Temperature-dependent of remanent polarization (P_r) of $GdMnO_3$ films coherently grown on (010)-oriented $YAlO_3$ substrates. Adapted from [46].

The rather large value of the electric polarization has been ascribed to the stabilization of an antiferromagnetic phase, characterized by an incommensurate Mn^{3+} spin ordering, which successively locks into a commensurate E-type state [64].

$GdMnO_3$ films onto (100)-oriented Si substrate prepared by sol-gel method that crystallize in a *Pbnm* orthorhombic structure with 230 nm average thickness, are paramagnetic above 80 K, showing a ferromagnetic response below 15 K (see Figure 11) [66]. The temperature dependence of the magnetization, measured in both zero-field- cooling (ZFC) and field-cooling (FC) conditions using 10 mT magnetic field is shown

in Figure 11. Both (ZFC) and (FC) magnetization M(T) curves merge from 300 K down to ~ 60 K. Below 60, the magnetization M(T) measured under (FC) conditions have higher values than obtained (ZFC). Although Kimura *et al.* [58] claim that the Néel temperature is ~ 42 K, the separation of the magnetization M(T) curves evidence for a weak ferromagnetism response just below 60 K, pointing for a upshift of Néel temperature and a change of magnetic structure in the films. Other anomalies in the magnetization M(T) curve are evident in ZFC conditions: a shoulder at ~ 17 K which has been associated in bulk $GdMnO_3$ to an incommensurate antiferromagnetic - canted antiferromagnetic phase transition and a maximum at ~ 6.5 K that corresponds to a long-range ordering of the Gd^{3+} moments associated with the interaction of the 4*f* spins.

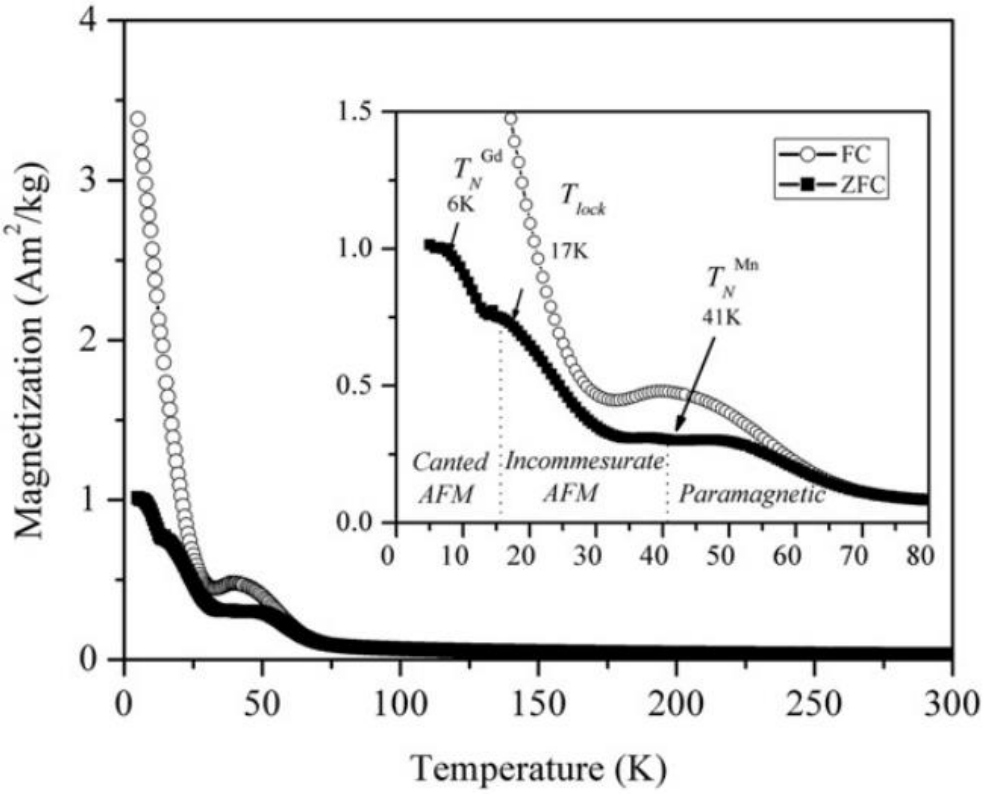

Figure 11: Temperature dependence of the magnetic response of the $GdMnO_3$ thin film annealed at 850 °C, measured in zero-field-cooling (ZFC) and field-cooling (FC) conditions, using 10 mT magnetic field. In the inset, T_N(Mn) is the Néel temperature for Mn^{3+} moments, T_{lock} is the lock-in transition temperature and T_N(Gd) is the Néel temperature for Gd^{3+} moments [66].

Interestingly, this 230 nm thick film in which its structure is already quite relaxed, exhibits a magnetic behavior similar to that reported in single crystal and ceramic, nevertheless the shape of the anomalies and the magnetic behavior at low temperature reveal that the response of these films is highly influenced by the substrate under an applied

magnetic field. An anomaly at T ≈ 27 K in the dielectric permittivity is also observed, which has been assigned to the magnetic transition taking place in this temperature range in bulk material, which reveals that at this temperature it is quite possible that the electric response can be influenced by the magnetic response [66], [67]. However, it seems that these results deserve further study.

More recently, a ferroelectric state, with rather high Curie temperature (T_C = 75 K) and a strong ferromagnetic component emerging below 105 K, was reported in orthorhombic $GdMnO_3$ thin films (average thickness 110 nm) deposited by pulsed laser method onto (001)-oriented $SrTiO_3$ substrates [65]. The emergence of an *ac*-plane spiral spin order (*Pnma* setting) below 105 K was proposed to explain the stabilization of the ferroelectric polarization and a nano-scale twin-like domain structure was appointed as essential for the rather high temperature ferroelectric and ferromagnetic phases observed in the $GdMnO_3$ films [65].

Hexagonal $GdMnO_3$ thin films have also been reported in literature [61], [62]. $GdMnO_3$ thin films deposited onto YSZ(111) substrates, with average thickness 67 nm, exhibit enhanced ferromagnetic properties [61].

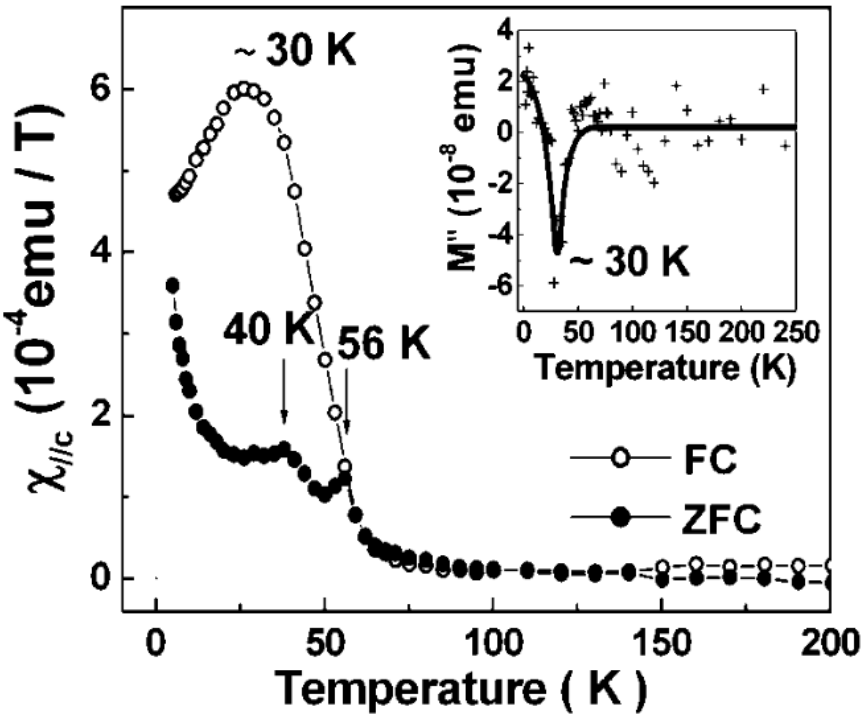

Figure 12: Temperature dependence of the dc magnetic susceptibility of $GdMnO_3$ thin films deposited onto YSZ(111) substrates, along the hexagonal direction *c*-axis, measured with an applied magnetic field of 100 Oe under both zero-field-cooling（ZFC) and field-cooling（FC) conditions. The inset shows the temperature dependence of the imaginary part of the ac magnetization measured at 1778 Hz oscillating magnetic field [61].

The temperature dependence of the magnetization measured in zero-field-cooling (ZFC) conditions (see Figure 12), shows clear anomalies at 56 and 40 K, respectively, while the field-cooling (FC) curve exhibits a broad peak at about 30 K. The anomaly at 56 K was assigned to the antiferromagnetic ordering of the Mn^{3+} spins in the in-plane triangular lattice, and the anomaly at 40 K was ascribed to the Mn^{3+} spin-reorientation transition [68]. The remnant magnetization (M_r) values are about 0.30 and 0.041 μ_B / f.u. at 4.2 and 30 K, respectively and the temperature variation of magnetization (M_r) indicates that the ferromagnetic transition occurs at around 30 K, which corresponds to the peak temperature of the (FC) curve in Figure 12. The inset of Figure 12 shows the temperature dependence of the imaginary part of the ac magnetization (M ”) under a magnetic field oscillating at 1778 Hz, yielding additional evidence that the ferromagnetic ordering starts at ~ 30 K, thus confirming that an artificial material with improved magnetic properties can be fabricated using the epitaxial stabilization technique.

1.4. Objectives of the thesis

As previously mentioned, $GdMnO_3$ proves to be a promising material due to its physical properties and some unique characteristics. One of them is that $GdMnO_3$ lies in the borderline between a non-spontaneous and spontaneous magnetoelectric multiferroic. However, the work that has been done so far has not been systematically explored. Here in this thesis, we will study strain-engineering using thin films deposited by the same technique on the same substrate, but with two different orientations. These two distinct orientations allow the induction of different states of mechanical stress which, in turn, cause different structural distortions that may stabilize in new crystallographic structures and strongly affect the transport and magnetic properties of $GdMnO_3$ thin films. We choose $SrTiO_3$ crystalline substrates since they are of oxide nature, and exhibit perovskite structure, allowing a good interconnectivity between the substrate and the film material, ensuring better epitaxy and control of octahedron rotation.

Our goal is to study fully tensioned thin films with sufficient thickness to allow analysis by various techniques. In this scope, we intend to produce non-relaxed $GdMnO_3$ thin films, in which the epitaxial strain induces structural changes, thus being able to alter the physical properties, since the relaxed thin films present structural, electrical and magnetic properties similar to the $GdMnO_3$ in bulk. As the latter case does not bring any novelty, we did not include the study of relaxed thin films in this work.

For the deposition of the $GdMnO_3$ thin films, the RF magnetron sputtering technique was used because it is the equipment that IFIMUP had available to deposit oxide films, guaranteeing a high quality in the production of epitaxial thin films.

The polar properties are studied by measuring the pyroelectric current using different experimental conditions and the magnetic measurements. The obtained results are discussed involving a comparison with previous results in orthorhombic $GdMnO_3$ films deposited onto similar substrates. Raman spectroscopy could not be performed due to the $SrTiO_3$ substrate signal overlapping the $GdMnO_3$ thin film spectra.

2. Experimental Procedure

The overall experimental procedure involved in this thesis work will be enlightened in this chapter. Firstly, we will present the substrate preparation and film deposition techniques. Secondly, a detailed description of the characterization techniques used to determine film structure and morphology will be considered. Finally, the macroscopic properties characterization techniques will be touched on.

2.1. Preparation and characterization of substrates

In general, the properties of the perovskite oxides will be similar to the bulk properties for small or negligible epitaxial strain, but they can be quite different with increasing tensile or compressive strain, due to the B-O-B bond angle and corresponding symmetry changes [69]. According to the crystallographic orientation of the flat surface of a crystalline and oriented substrate, different film strain states can be induced in thin films, and thus it is possible to impose specific lattice distortions arising from changes in the oxygen octahedra tilts over several atomic layers. These tilts control many electronic and magnetic interactions which, in turn, profoundly alter the physical properties of the film. For instance, considerably reshaping the magnetic phase sequency in rare earth manganites.

Thin films are usually under mechanical strain due to the misfit between the lattice parameters and thermal expansion coefficients of substrate and the material from which the film is made up [69], [70]. The misfit arising from the differences between lattice parameters, as well as the different crystal symmetries, namely, the substrate orientation surface, have also strong effect on the film orientation growth and structure, underlined by the structural distortions occurring on non-relaxed epitaxial thin films. It is worth mentioning the important role of the substrate to define not only the structure of the films but also their physical properties. The substrate structure is also fundamental for the homogeneous growth of the films and obtaining the desired phase of the film.

So, the substrate selection, including its orientation, is of high relevance for the tuning of structure and properties of functional materials towards applications. According to the difference between the substrate and material film lattice parameters, two scenarios can be envisaged: film distortion involves the in-plane stretching (tensile strain) or in-plane compression (compressive strain) [71].

Usually, the strain state of a non-relaxed film is characterized by the epitaxial strain, also called lattice mismatch, defined as follows [72]:

$$\varepsilon = \frac{a_{substrate} - a_{bulk}}{a_{bulk}} \quad , \tag{2.1}$$

where $a_{substrate}$ and a_{bulk} are the pseudocubic lattice parameters of the substrate and the bulk material, respectively.

The $GdMnO_3$ thin films were deposited onto (100) and (110) oriented crystalline $SrTiO_3$ substrates. Table 2 shows the values of the pseudocubic lattice parameters (a_{pc}) of bulk $SrTiO_3$ and $GdMnO_3$, and the epitaxial strain, following equation (2.1), which corresponds to a moderate tensile strain. Figure 13 shows the pseudocubic lattice parameter of bulk crystalline $GdMnO_3$, and $SrTiO_3$, together with the calculated epitaxial strain from Table 2.

Table 2: Crystal symmetry, pseudocubic lattice parameters (a_{pc}) of bulk $SrTiO_3$ and $GdMnO_3$, and the corresponding epitaxial strain (ε) [73].

	$SrTiO_3$	$GdMnO_3$
Crystal Symmetry	**Cubic** ($Pm\bar{3}m$)	**Orthorhombic** ($Pnma$)
apc (Å)	3.905	3.868
ε (%) $GdMnO_3$	+ 0.96	---------

For the study of the strain effects on the physical properties of $GdMnO_3$ thin films, (001)-oriented $SrTiO_3$, crystalline substrates were chosen to impose tensile strain states.

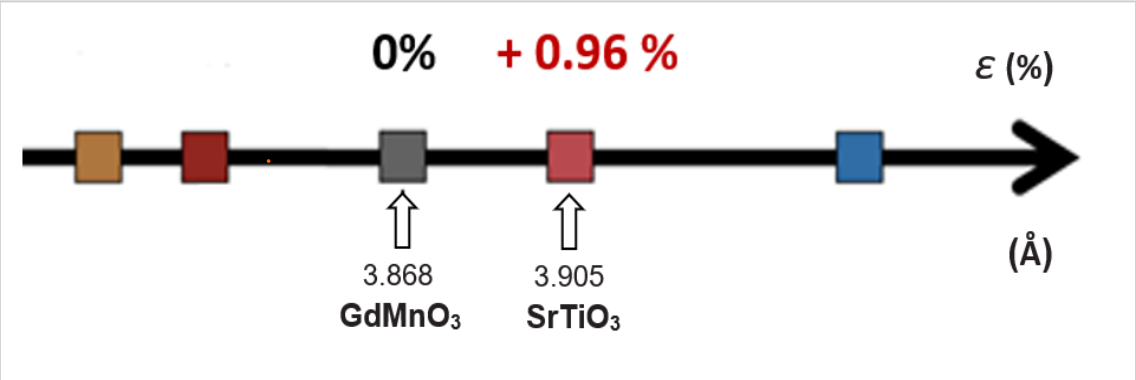

Figure 13: Schematic representation of the lattice mismatch (above) between the in-plane pseudocubic lattice parameter (below) of bulk $GdMnO_3$ deposited onto $SrTiO_3$ substrates.

The substrates with 10 x 10 x 0.5 mm^3 were acquired from Surface Net Corporation, with a mean roughness of 5 Å in both side polished faces and an off-set angle of 0.5°. Figure 14 shows the topography of the atomic structure surface of as-received $SrTiO_3$ (001) substrates. Figure 14 (c) shows the line profile of the corresponding AFM-3D image in Figure 14 (b) thus confirming the low roughness presented by the manufacturer and the high quality of the substrates to be deposited.

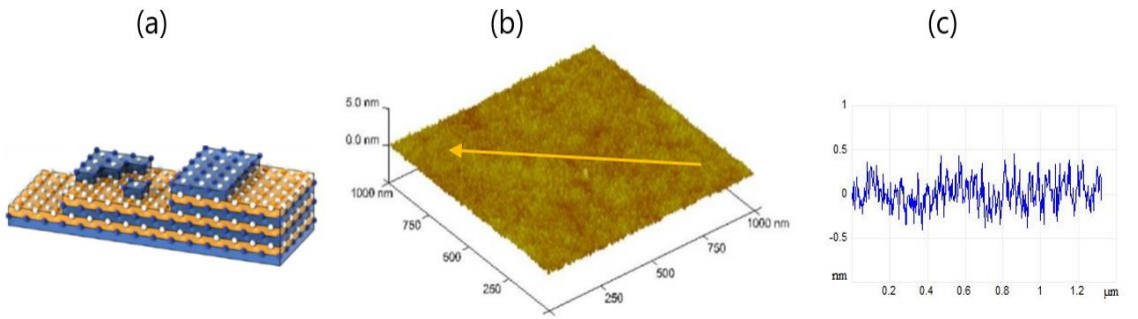

Figure 14: Typical topography a) Schematic, b) AFM image, and c) surface profile of an as-received (100)-oriented $SrTiO_3$ surface atomic structure [74].

In this work, all the substrates were cleaned before the deposition in ultrasonic baths, to remove dust particles and greases, using acetone and isopropanol, for 15 min each and soaked in deionized water.

2.2. Characterization of targets

Ceramic target of $GdMnO_3$ was supplied by Prof. Pedro Tavares, from the Centro de Química de Vila Real, Universidade de Trás-os-Montes e Alto Douro.

The target was produced following the sol-gel combustion method. Details of the ceramic processing can be found in Ref. [75]. They were first characterized from the chemical and structural point of views by X-Ray Diffraction, Energy Dispersion X-Ray Spectroscopy, Fourier Transform Infrared Spectroscopy and Scanning Electron Microscopy. Raman analysis was also performed at room temperature in order to confirm the previously obtained results. From this study, it was possible to ascertain that all processed samples are stoichiometric.

2.3. $GdMnO_3$ thin film deposition

The choice of the technique for the deposition of $GdMnO_3$ films was based on different reasons, namely their thermodynamic properties and the stabilization of the desired phases. Following the previous experience of the research team, we have selected the RF-magnetron sputtering technique.

2.3.1. RF-magnetron sputtering technique

The RF-magnetron sputtering uses a gaseous plasma which is generated and confined to a space including the target, made of the material to be deposited. The surface of the target is eroded by high energy ions within the plasma, and the released atoms then are directed, through the vacuum environment towards the substrate to form the film.

Figure 15 shows a scheme of a RF-magnetron sputtering technique. The main components mounted or inserted, inside a special chamber consist of: The cathode, involving below the magnets (magnetron); The target holder that supports the target, attached to the cathode; The working gas for extracting the deposited atoms from the target; The substrate that is attached to a heater and connected to the anode, and the radio frequency power source, instead of a direct current source, to avoid the accumulation of positive charges that would occur on the target (due to its insulating nature), decreasing the cathode capacity to zero to attract the working gas ions. To ensure a clean environment, the chamber is first evacuated to 5×10^{-6} mbar, and then filled with the working gas. During a half cycle of applied RF-power, wherein a negative electric potential is applied to the cathode, free electrons are accelerated away from it that, by colliding with the working gas atoms, create positive charged ions. These ions are in turn accelerated towards the target. This bombardment leads to the ejection of atoms from the target by physical processes of energy and linear moment. The ejected atoms from the target are then deposited on the substrate forming a film. During the other half cycle of the applied RF-power (positive electric potential is applied to the cathode),

the expected charge build-up on the target surface can be hampered by the free electrons that are attracted to the target, ensuring a negative bias. Moreover, this technique uses magnets behind the cathode to trap electrons over the negatively charged target. Hence, they are not able to bombard the substrate, allowing for faster deposition rates. The schematic plasma in Figure 15 stems from the recombination process of the electrons and the argon working gas ions [76]–[79].

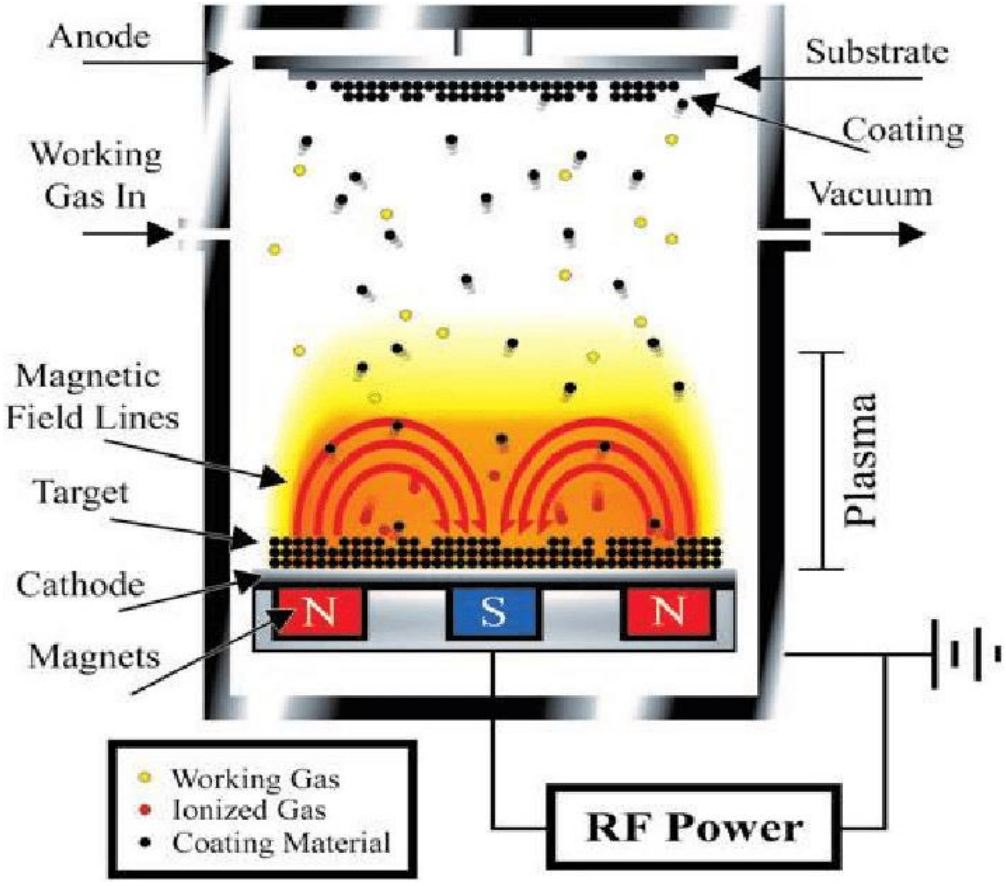

Figure 15: Scheme of a RF- magnetron sputtering deposition system, adapted from Ref. [80].

The radio frequency powering provides sufficient energy to the oscillating electrons to yield ionizing collisions, and thus a self-sustained discharge is maintained. As electrons have higher mobility compared to ions, more electrons will reach the insulating target surface during the positive half cycle than the positive ions during the negative half cycle. Hence the target will be self-biased negatively. This charged surface repels the electrons from the vicinity of the target, and an enriched positive ion layer is formed in this region. These ions bombard the target and sputtering is achieved [76], [77].

One of the advantages of this technique is the high kinetic energy of deposited material that upon reaching the surface of the substrate, increases the mobility of the adsorbed atoms allowing them to better rearrange, thus improving the film properties. The efficiency of this process can be tailored by several factors that directly influence the deposition rate and morphology of the films [81]:

- **the pressure of the gas**, which influences the plasma density and the scattering of the atoms released from the target. By the kinetic theory of gases, an atom is more likely to undergo inelastic scattering at high pressures. This is, however, a disadvantage if the deposited material loses energy, colliding with the gas phase during movement towards the substrate. So, there should be an optimal pressure for reaching the highest possible deposition rate. Figure 16 shows a representative plot of deposition rate/sputter efficiency as a function of gas pressure, hence it is possible to increase the number of Ar ions without increasing the number of Ar neutrals, and to work at relatively lower gas pressure 150 $\times 10^{-3}$ mbar;

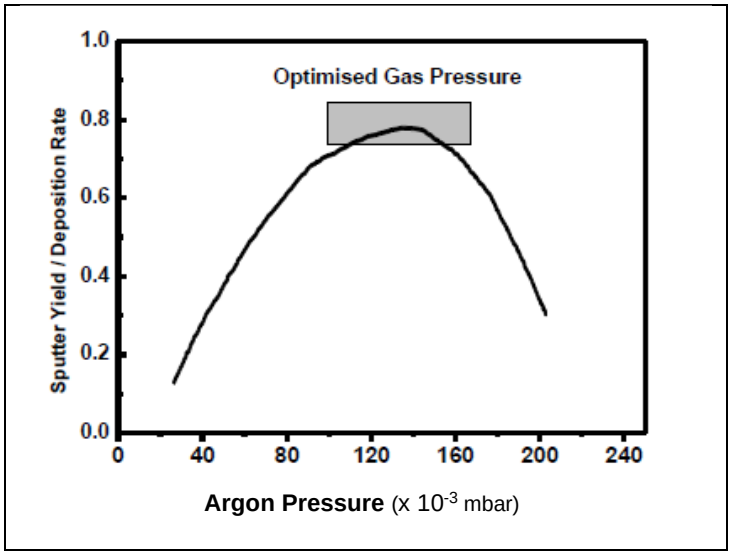

Figure 16: Sputter Yield/ Deposition rate as a function of working gas pressure (Ar) [81].

- **the distance from the target to the substrate** can alter the degree of spreading of the species released from the target. If the travelling distance between atoms increases, further spreading occurs. Additionally, increasing the distance from the target to the substrate will increase the angular distribution of the flow and, consequently, decrease the deposition rate;

- **the temperature of the substrate** influences the mobility of atoms on the substrate surface, thus modifying adhesion, roughness, phase stability, growth, and nucleation [76], [77], [80], [81].

The deposition begins when the first particles impinge the substrate, and then start to diffuse through its surface, chemically bonding to it. This process takes place continuously, forming a film that grows on the surface. The particles can diffuse through the material in different ways, giving rise to different growth modes of the film, as shown in Figure 17.

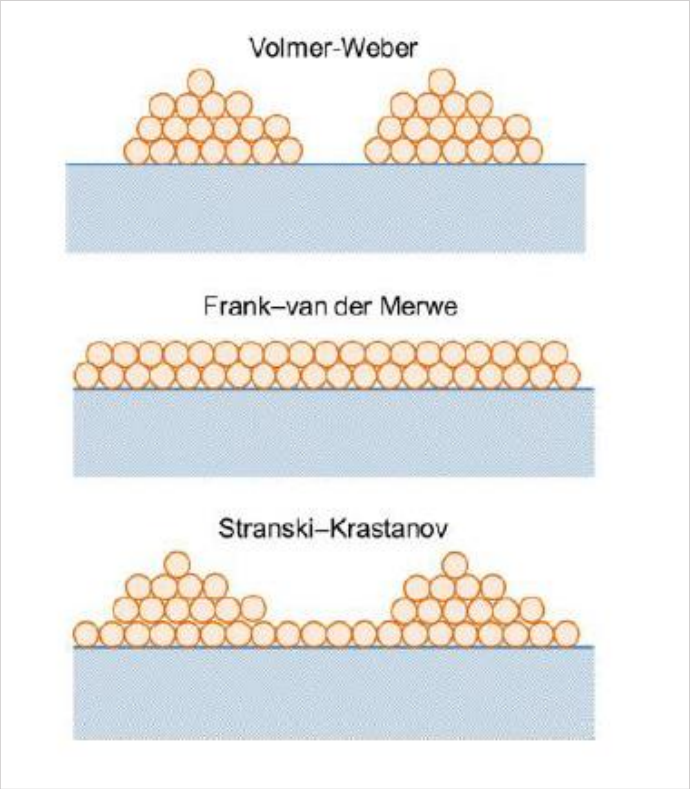

Figure 17: Schematic representation of the three growth modes of the film [82].

Volmer-Weber growth is done by islands due to the greater cohesion energy between the atoms of the film when compared to that of the substrate. Two-dimensional or Frank-van der Merwe growth consists of successive monoatomic layers resulting from a lower interatomic cohesion energy of the film compared to the substrate. Mixed or Stranski-Krastanov growth: initially two-dimensional growth that converts to three-dimensional due to the decrease in the cohesion energy between the atoms and the substrate as the number of layers increases [82].

The system used for the $GdMnO_3$ film deposition is shown in Figure 18. It consists of a spherical chamber with diameter ~ 250 mm with three sputter guns in a confocal arrangement. One sputter gun is used for RF sputtering to deposit insulators/semiconductors, which is our case, and the other two are operational for DC magnetron sputtering used for metallic targets. A 600W (13.56 MHz) *US Gun II-Meivac* RF power supply with an impedance matching network is used for the RF sputtering. Targets of 2-inch diameter are used so that sputtering can yield uniform deposition over 3-inch substrate holder.

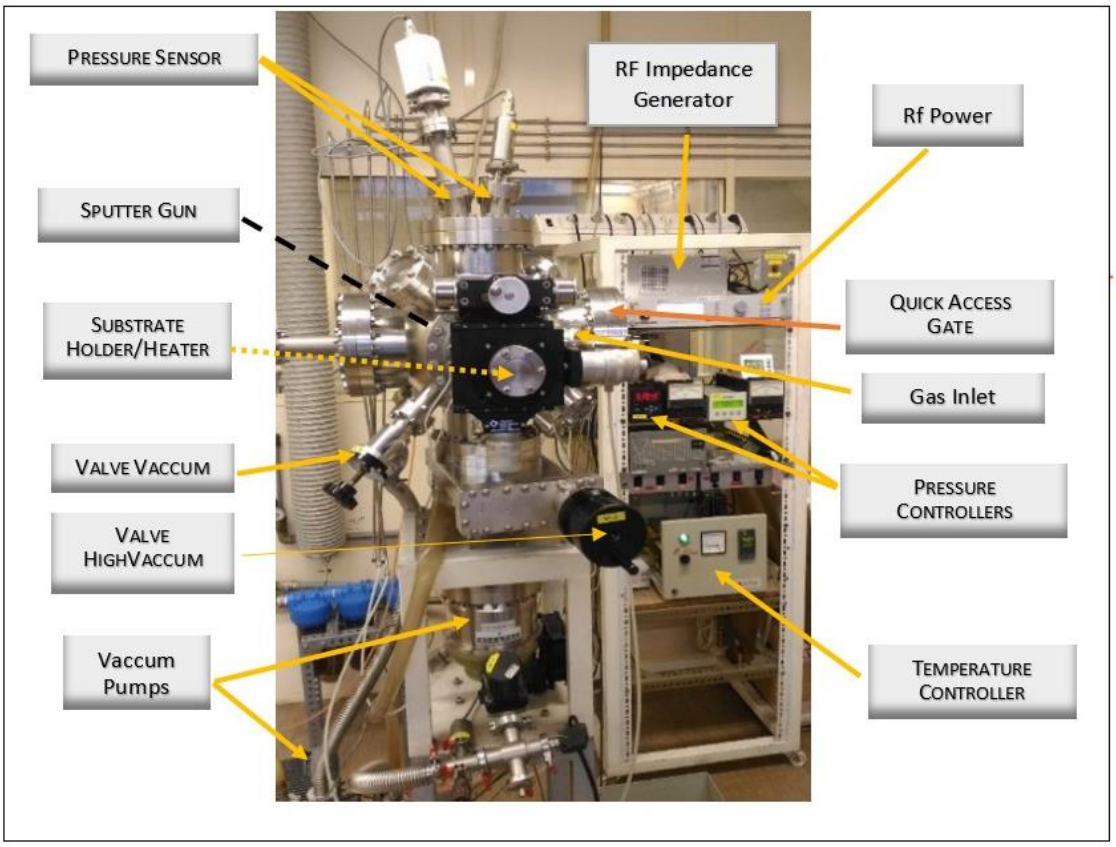

Figure 18: Image of the RF-magnetron sputtering deposition system.

The high temperature heater *Meivac HTR 950-C* is used to keep the substrate at 800 °C during deposition, and temperature is measured with a *K*-type thermocouple positioned directly behind the substrate. The distance between target and substrate was fixed at 130 mm.

The pumping system consists of a turbo molecular pump backed by a rotary pump. Prior to deposition, the chamber was evacuated to 5×10^{-6} mbar. There are two needle valves and adjustable control through partial pressure between the deposition chamber and the vacuum system to maintain a dynamic vacuum in the chamber. During film deposition

the pressure inside the chamber was adjusted to 5×10^{-2} mbar using a reactive O_2 gas and argon working gas composition setting a ratio of Ar:O_2 of 4:1. Oxygen is essential to control the stoichiometry of the deposited material, ensuring the film's properties.

2.3.1.1. Preparation of $GdMnO_3$ thin films

The $GdMnO_3$ thin films were deposited through RF-magnetron sputtering, working at 80 W RF power and 13.56 MHz, onto substrates of $SrTiO_3$ (STO) with the following orientations STO(001) and STO(110). All the substrates were previously cleaned and characterized as described in section 2.1. The deposition rate of $GdMnO_3$ was estimated to be around 2 nm/min. After deposition, the films were left to cool naturally to room temperature in a pure oxygen atmosphere of 1 mbar, without any annealing step.

The choice of the deposition conditions and parameters to achieve a high particle flux, uniformity and density of the films stemmed from a previously work carried out by a group of researchers we have collaborated with: Profs. Ramiro Fernandes and Pedro Tavares from the Centro de Química de Vila Real, Universidade de Trás-os-Montes e Alto Douro.

2.3.1.2. Assessment of the RF-magnetron sputtering

The RF-magnetron sputtering allows to obtain films with a good adhesion to the substrate, excellent uniformity, with smooth surfaces, obtaining different properties of the volumetric material in bulk when the thickness of the film is about a few unit cells, still offering a huge range of advantages, not only in terms of the control of the parameters of deposition and deposition rates, but also in terms of obtaining considerable adhesions (achieved in part by prior ionic cleaning of the substrates - Etching). In addition to the characteristics already mentioned, there are others that justify the application of this. Among these, the following stand out: (i) possibility of operating at very low working pressures, allowing the synthesis of high purity materials; (ii) providing relatively high deposition rates (depending on deposition parameters); (iii) possibility to reproduce results and control the thickness, once the parameters are established; (iv) coating structure control; (v) Ion bombardment promotes epitaxial growth and promotes atomic mobility; (vi) Relative low deposition temperatures. Moreover, the choice of a suitable substrate temperature can drastically affect surface diffusion and nucleation processes. Still, the aforementioned abilities can play a key role in determining grain size, morphology, and epitaxy of the deposited films [83], [84].

2.4. Structural characterization

2.4.1. X-ray diffraction

X-rays is an electromagnetic radiation in the range of wavelength between 100 Å and 0.1 Å. Due to the wavelength values, X-ray radiation can be used to measure interatomic distances through diffraction. X-ray diffraction is the most widely used technique for general crystalline material characterization, including the study of crystal structure (atomic positions and lattice parameters), lattice distortions and residual stress states, defects, crystallite size, preferential orientation growth of thin films, among others [85].

The X-ray diffraction phenomenon can be explained by two different but completely equivalent approaches. Let's begin with the Bragg formulation of the X-ray diffraction. According to the Bragg formulation the diffraction occurs as a consequence of the constructive interference of specularly reflected X-rays by the atoms in consecutive crystallographic planes. Figure 19 shows the reflection of an X-ray beam by two adjacent planes, spaced a distance *d* apart. The collimated X-ray beam impinges the crystallographic plane at an angle *Θ*, and a diffraction peak will be observed when the path difference between two rays is an integral number of wavelengths, leading to the well-known Bragg's Law:

$$n\,\lambda = 2\;\; d_{(hkl)}\sin\theta \tag{2.2}$$

where *λ* is the X-ray wavelength, $d_{(hkl)}$ is the distance between crystalline planes, *Θ* is the angle between the incident beam direction and the direction of the Bragg plane responsible for the diffraction and the integer *n* is called the order of the corresponding reflection.

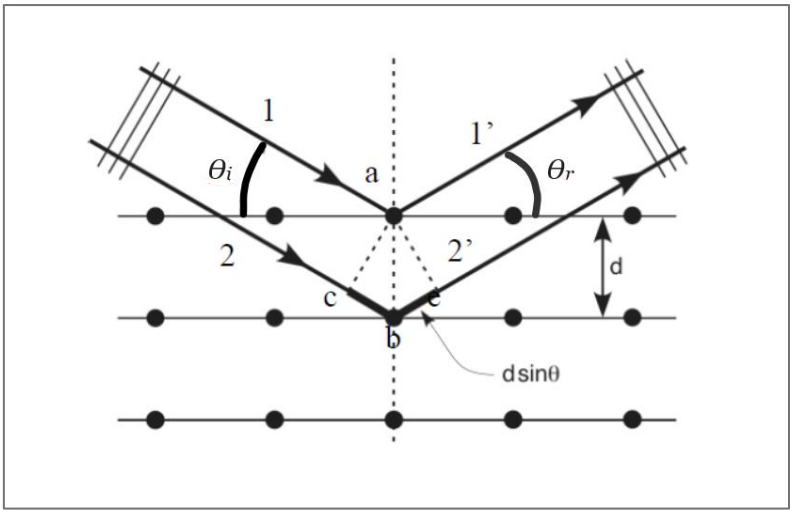

Figure 19: Schematic representation of diffracted X-rays by the layers of atoms in a crystalline material [86].

An alternative approach of the X-ray diffraction was presented by Max von Laue. According to Max von Laue**,** no particular sectioning of crystal into lattice planes is considered and no assumption of reflections is assumed. Instead, the crystal is regarded as composed of atoms or ions placed at Bravais lattice sites. Each of the atoms elastically scatter the incident radiation in all directions. Diffraction peaks will be observed in directions for which the scattered rays from all atoms interfere constructively. This condition is fulfilled when the change in wave vector of the scattered and incident X-rays beams is a vector of the reciprocal lattice:

$$\vec{k}\,' - \vec{k} \quad = \overrightarrow{K'} \quad , \tag{2.3}$$

Where $\overrightarrow{k'}$ and $\vec{k}$ are the wave vectors of the incident and scattered rays, and $\vec{K}$ is a reciprocal lattice vector (see Figure 20).

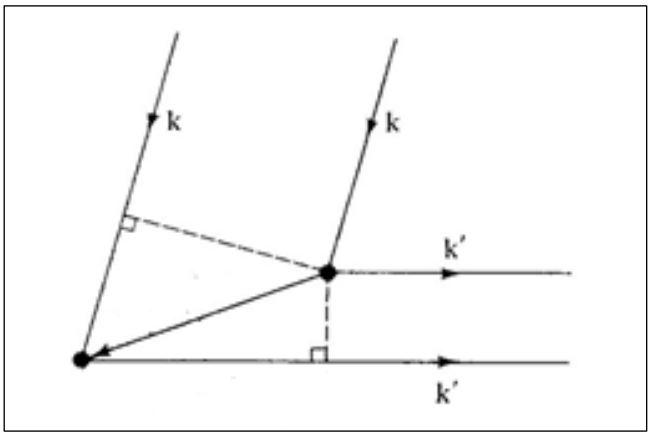

Figure 20: Schematic representation of diffracted X-ray diagram of Max von Laue formulation [87].

The two approaches are equivalent. Actually, the Laue diffraction peak corresponding to a change in the wave vector given by reciprocal lattice vector $\vec{k}$ corresponds to a Bragg reflection from the family of planes perpendicular to $\vec{k}$. From the conceptional point of view, the Laue formulation brings in the reciprocal lattice to play a more expressive role in the description of the crystalline structure; the reciprocal lattice is the geometric place after which diffraction peaks have to be found out. Moreover, the Laue formulation is the most suitable for the description of the X-ray diffraction techniques.

2.4.1.1. Powder diffraction method

This method uses a polycrystalline sample or powder in which grains are still large on the atomic scale. Since the grains are randomly oriented, the diffraction pattern produced by the sample is a combination of the diffraction from all possible orientations of the single crystal. This method is most suitable wherein large and high-quality crystals are not available. Moreover, even when appropriate crystals are available, this method is still extensively used. In this case, the crystal is crushed, and the obtained powder sieved to ensure grain size uniformity.

In this thesis, the crystalline structure of targets and films and the search for the possible emergence of secondary phases was carried out using this technique.

The diffraction patterns were recorded using a X'Pert Pro, PANalytical diffractometer, in the Bragg-Brentano geometry, of the Electron Microscopy Unit of Centro de Química, at University of Trás-os-Montes and Alto Douro in Vila Real, Portugal, by Prof. Pedro Tavares. The measurements were performed using the $K_{\alpha 1}$ and $K_{\alpha 2}$ doublet emitted by the Cu cathode, with wavelengths 1.540598 Å and 1.544426 Å, respectively. The diffractometer uses a X'Celerator detector, with a Ni filter to minimize the K_{β} radiation and a secondary monochromator. An acceleration voltage of 50 kV and a current of 40 mA were used for performing conventional theta-2theta (Θ-2Θ) scans.

The phase formation and crystallographic structure of the films were analyzed by high resolution X-ray diffraction (HR-XRD) at room conditions, using a *X'Pert MRD Philips* four-circle diffractometer, based in a Bragg-Brentano para-focusing optics configuration, operating with Cu K_{α} radiation λ = 1.54056 Å at 30 mA and 40 kV, for performing conventional theta-2theta (Θ-2Θ) scans, pole figures and reciprocal space maps (rsm). Analysis of the X-ray diffraction patterns was performed through the basic Le Bail mode for assessment of crystallographic structure and parameters of the film. Full Rietveld refinements were performed on targets using PowderCell 2.4 and HighScore 4.8. Volume percentages from PowderCell were converted to weight percentages using the calculated density from each phase. Lattice parameters and Wyckoff positions were obtained from the Rietveld refinements.

X-ray diffraction has the advantage to be a powerful non-contact and non-destructive technique for studying crystalline structural materials that can be used in most environments, less expensive and practical to operate comparatively to other techniques that provide structural information.

2.4.1.2. Pole figure

A pole figure is a plot of the orientation of a particular set of crystallographic lattice planes, providing a useful illustration of the material texture. This technique allows to determine the preferred crystalline orientation of a film onto a substrate. The pole figure is a recording of intensity of a Bragg peak as a function of rotation and tilt of the sample at different slopes or Psi angles, performed at a fixed dispersion angle (constant *d* spacing), as it is shown in Figure 21. Pole figures are defined by the integral intensities of Bragg reflections, using for the measurements a single detector (usually a scintillation counter) with a wide receiving slit, wherein the integral intensity of a given Bragg reflection is obtained directly. Integral intensities of the diffraction peaks can then be obtained mathematically using peak profile analysis both on overlapped (profile deconvolution) and separated (profile fitting) reflections.

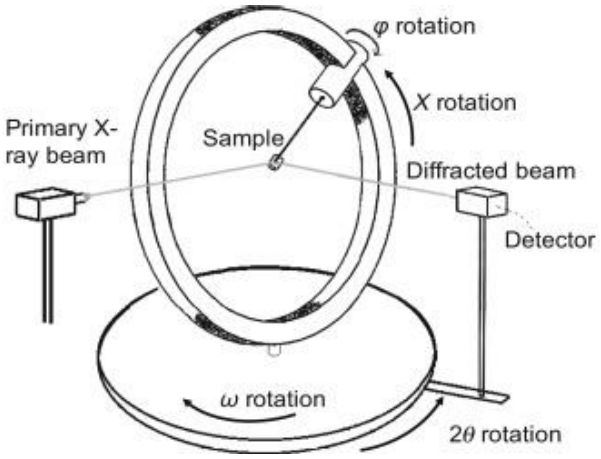

Figure 21: Principle of a 4-circles diffractometer, and definition of rotation angles [88].

The peak profile analysis provides, besides the integral intensity, several other peak parameters, characterizing an individual (*hkl*)-reflection. These parameters are the peak maximum intensity, peak position or peak shift, peak width or peak shape parameters, the local peak background, and the fitting error. The availability of all these peak profile parameters in each sample position allows to define and plot new generalized "pole figures". Besides the texture information contained in the integral intensity pole figures, these generalized pole figures contain information about other microstructural quantities, e.g. particle size, lattice strain, diffuse scattering and amorphous phases.

In an attempt to identify the phases in the films deposited on substrates, the structural investigations were performed using high resolution four-circle diffractometer. The orientation of the films was investigated by Φ scans for an asymmetrical reflection Ψ at

a fixed angle 2Θ, and the Reciprocal Space Maps (RSM) were recorded by analyzing epitaxial thin films. Narrow scans of reciprocal lattice points were performed for various diffractometer settings and the scattered intensity plotted in a 2-dimensional frame.

2.4.2. X-ray reflectometry

The X-ray Reflectometry (XRR) is an analytical technique with high accuracy that uses the effect of total external reflection of X-rays to evaluate surface and interface roughness, to determine the density and the thickness of thin layered structures (from few nm up to 1000 nm) deposited in plain substrates. This method is based on the Bragg-Brentano configuration without so many geometry restrictions relatively to the adjustment of the incident beam to the sample, critical angle, being the measurement performed within a grazing angle of $0.01° < \Theta < 6°$.

Below the critical angle of total internal reflection, X-rays penetrate only a few nanometers into the sample but above this angle the penetration depth increases rapidly. As shown in Figure 22 at every interface where the electron density changes, a part of the X-ray beam is reflected and then interference occurs between the X-rays reflected from the adjacent surface of the film, and the interface between film and substrate. The reflected rays interfere, yielding an intensity oscillation pattern.

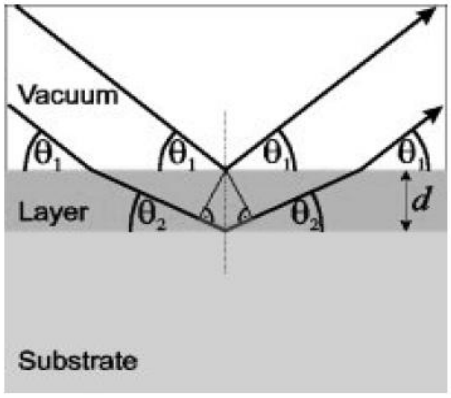

Figure 22: X-Ray Reflectivity and interference effect due to the interfaces of different materials [89].

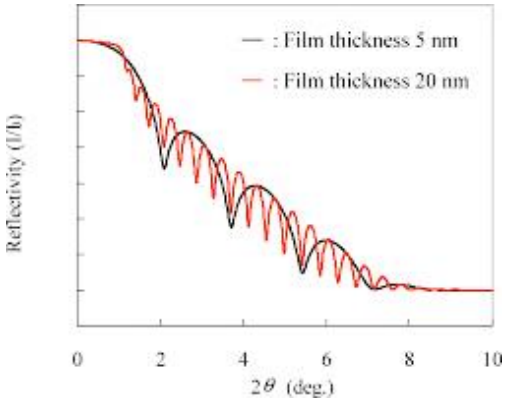

Figure 23: X-Ray Reflectivity curve of constructive interference as a function of the angle 2Θ for two different films thicknesses [90].

Figure 23 presents a typical oscillation profile in the reflectivity curve. The positions of interference fringes observed in a reflectivity curve can be used to determine the

thickness (*d*) of the film. The *Θi* values for the maxima and minima of the interference fringes are associated with the value of *d* by the modified Bragg equation as follows [91]:

$$2\,d\,\sqrt{Sin^2(\Theta i)\,-Sin^2(\Theta c)}\;=m\,\lambda \qquad (2.4)$$

where Θ_i is the observed position of the maximum or minimum of the i^{th} interference fringe, Θ_c the critical angle for total reflection, *m* an integer and *λ* the X-ray wavelength.

This technique does not work effectively if there is no difference between the electron density of different layers or between layer and substrate. While the oscillation amplitude (at fixed photon energy) depends on the difference between the electronic densities of the film and its substrate, and the surface and interface roughness, the oscillation period is mainly determined by the layer thickness.

X-ray reflectivity measurements were performed using a the X'Pert Pro, PANalytical diffractometer, in the Bragg-Brentano geometry of the Electron Microscopy Unit in Centro de Química, at University of Trás-os-Montes and Alto Douro in Vila Real, Portugal, by Prof. Pedro Tavares. An acceleration voltage of 50 kV and a current of 40 mA were used for performing conventional theta-2theta (Θ -2Θ) scans within a grazing angle of 0.3° < Θ < 1°. In this technique, the observed scattering X-rays reflected from the sample is measured as a function of the grazing incidence angle of the X-rays and are the sum of individual electron scattering. The XRR data measurements were then simulated and fitted by using PANalytical X'Pert Reflectivity software.

2.5. Morphological characterization

2.5.1. Scanning electron microscopy

The Scanning electron microscopy (SEM) is a technique that allows the morphological characterization and observation of a material in the sub-micrometer scale, by scanning the sample surface with a focused electron beam. The interaction of incident electrons, having energies in the 0.1 - 30 keV range, with the atoms of the sample yields different process which can be used for structural, morphological and chemical analysis. These processes are shown in Figure 24.

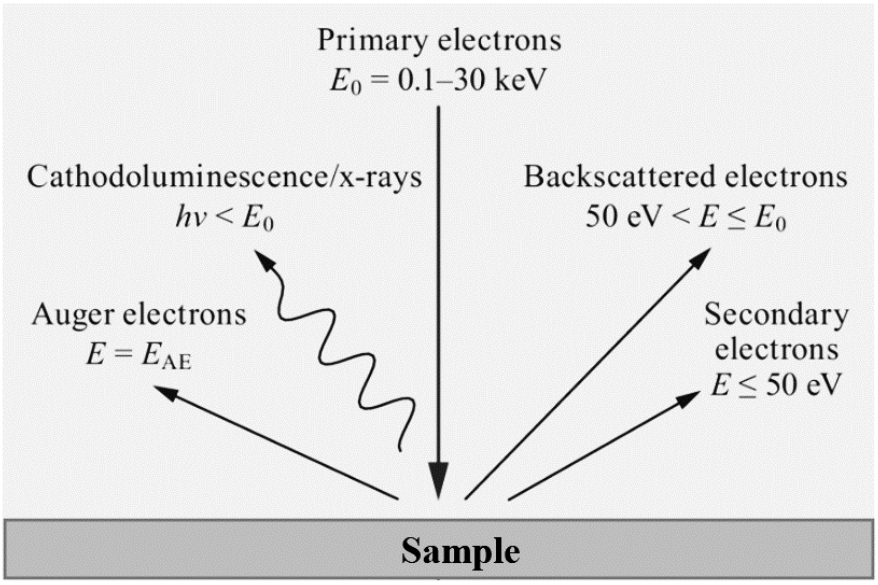

Figure 24: Schematic representation of the process resulting from the interaction of an electron beam with the atoms of the sample in SEM [92].

The signals used in SEM analysis mainly result from the following processes [92]:

1) secondary electrons, whose mean free path in solids is a few nanometers in length, and thus only c.a. 10 nm from the top sample surface can be observed. These electrons provide a major signal collection to reconstruct the image of the sample surface with resolution better than 1 nm.
2) backscattered electrons produced by elastic scattering from the sample, with energies higher than the one of secondary electrons. The former electrons, emerging from deeper localization relative to the sample surface, provide in-depth information, although with less resolution than the image obtained using secondary electrons. The backscattered electrons are also used for elemental distribution analysis.
3) Characteristic X-rays, which are generated from the interaction between the incident electron beam and the atoms of the sample. The collisions between the incident electrons with an atom can remove an inner shell electron from the target atom. Consequently, a higher energy state electron can fill the inner shell, releasing a photon. The energy of the emitted photon is characteristic of the electronic transition. Thus, the analysis of the photon emission, located in the X-ray frequency range, can be used for elemental identification, and chemical characterization. This process is the basis for the Energy Dispersive X-Ray Spectroscopy (section 2.5.2).

Scanning Electron Microscope to which an X-ray detection unit is often associated, is a widely used instrument providing information regarding morphology, thickness, and chemical composition, and supporting development/quality control of materials for technological application. Figure 25 shows a basic schematic representation of a SEM.

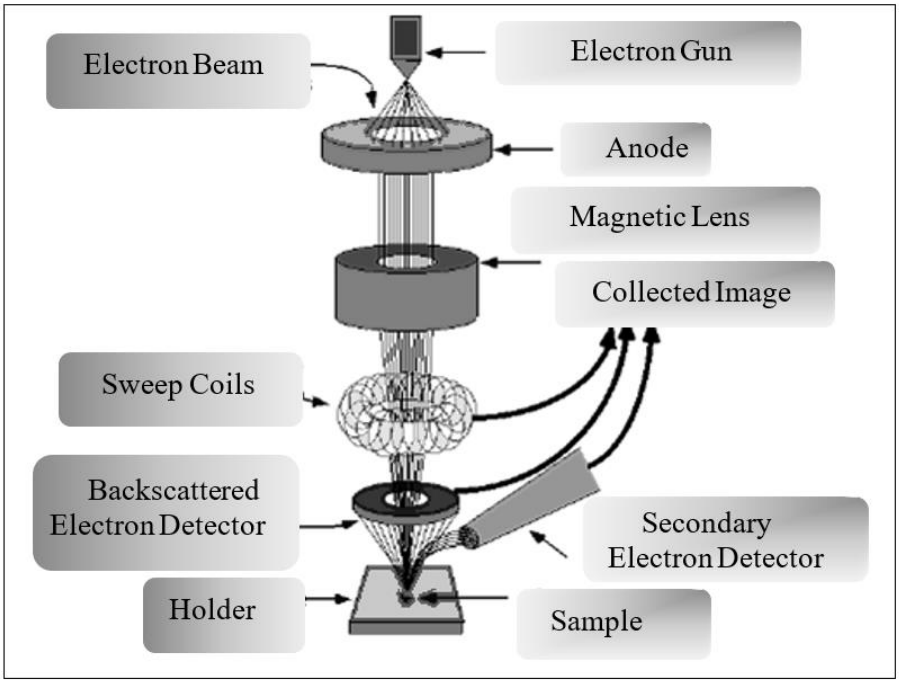

Figure 25: Operating principle of a scanning electron microscope [92].

A basic scanning electron microscope consists of three basic systems that operate together:

• The control console that allows electronic beam control, image processing, scanning/synchronization and control of the vacuum system.

• Vacuum system needed as all processes take place in a vacuum.

• Electron gun: allows electrons to accelerate and create the electronic beam.

Figure 25 describes several components that are essential to its operation. The electron gun produces and accelerates electrons up to the sample under vacuum to prevent their dispersion. The set of magnetic lens allows the electron beam to be focused on the sample and the condenser lens converge and collimate the electron beam, controlling its cross area on the sample. Thereafter, the objective lens directs the focus of the secondary or backscattered electrons from the sample to the electron detectors, wherein the signal is subsequently handled in order to create an image pixel by pixel on a screen.

For this purpose, the electron beam scans the sample horizontally in perpendicular directions (X and Y) [93]–[95].

The samples to be observed in SEM must satisfy several prerequisites. Towards ensuring stable measuring conditions, they should: (i) Not decompose or volatilize in vacuum, (ii) have physical and chemical stability against the effects stemming from the interaction with electrons, (iii) and have superficial electrical conductivity in order to avoid the accumulation of charge, otherwise, a thin layer of gold or other conductive material must be deposited on the sample surface.

The SEM technique was used for the morphological characterization of both targets and films to determine surface topography, cross-section thickness, and chemical composition. To this purpose, the scanning electron microscopy (SEM) in a *Quanta 400 FEG ESEM/EDAX Genesis X4M*, with 15.00 kV for secondary electrons mode and for backscattering mode, at CEMUP in University of Porto, was used.

In this study, the thickness of $GdMnO_3$ films was determined by SEM. XRR was used mainly to confirm the thickness obtained by SEM. It should also be noted that SEM is a destructive technique, since the samples have to be first cut to obtain a suitable cross section that allows the direct observation of the thickness [96].

2.5.2. Energy dispersive X-ray spectroscopy

Energy dispersive spectroscopy (EDS) is an analytical technique to obtain the corresponding elemental composition and chemical characterization of samples by using the emitted X-ray during the electron's bombardment in SEM or TEM measurements. The electron beam interacts with the sample atoms through the ionization of an inner shell electron which remove an electron from an atom. An electron from a higher energy outer shell fills the vacant inner shell, releasing an X-ray photon equal to the potential energy difference between the two shells, which is specific for each element [97]. This process can be used to provide qualitative and/or quantitative information about the elements present at different points of the samples, enabling to trace a map regarding the concentration of each element as a function of the position.

Both SEM and EDS techniques were used from a user perspective. The experiments were carried out by a technician responsible for the operation of the FEI Quanta 400FEG-ESEM / EDAX Genesis X4M coupled with energy dispersive spectroscopy at CEMUP in University of Porto.

2.5.3 X-ray photoelectron spectroscopy

X-ray Photoelectron Spectroscopy (XPS), also known as Electron Spectroscopy for Chemical Analysis (ESCA), is a surface analysis technique, which provides information about the elemental composition, empirical formula, chemical states (oxidation states or chemical groups) and electronic states (electron configurations) of the elements present in the material, as well as their bonding states through the detection of photoelectrons emitted from the sample after it has been irradiated by single-energy X-ray photons (see Figure 26). This technique is useful for quantitative analysis of surface composition and can detect all elements, with the exception of helium and hydrogen, by photoelectron binding energies. Nevertheless, XPS is very sensitive to any surface contamination and/or degradation due to a very small depth of analysis and it is often necessary to clean the surface of materials by sputtering. Typically, XPS probes to a depth of 10 nm, which results from the mean free path of photoelectrons in matter since X-rays penetrate much deeper.

To apply this technique, the sample is subjected to ultra-high vacuum conditions and then analysis is performed by irradiating the material surface with monoenergetic soft X-rays, most commonly Mg K_α (1253.6 eV with a line width ~ 0.7 eV) or Al K_α (1486.6 eV with a line width ~ 0.85 eV), and analyzing the photoelectrons emitted from the surface [98].

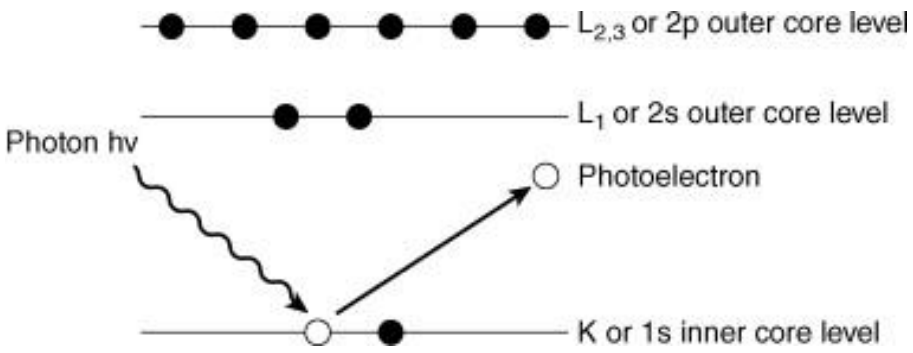

Figure 26: Schematic diagram of photoemission process used for XPS. X-rays excite and remove an electron from a core level. The kinetic energy of that electron is equal to the energy of the photon, minus the binding energy of the core electron and the work function of the spectrometer (**$E_k = hv - E_b - \varphi_s$**) [99].

The principle of XPS is based on the photoelectric effect, in which the energy of the photoelectrons emitted from the sample is characteristic of each element, being the binding energy (E_b) of the ejected electrons determined from the measured kinetic energy (E_k) by the equation (2.5):

$$E_b = hv - E_k - \varphi_s \quad (2.5)$$

The E_b is the binding energy of core level electron, *hv* the characteristic energy of X-ray photon, E_k the kinetic energy of ejected photoelectron and φ_s the spectrometer work function [99].

When the energy of incident X-rays photons is enough to eject electrons from most of the energy levels of the atoms (including the core levels), thus leaving the atoms in an unstable energetic state, they return to the fundamental state by different ways. The emission of X-ray (or other) photons is one of them, but the technique does not analysis the radiation emitted from the sample, so this process does not perturb the XPS analysis because the detector is only electron sensitive. Another process is the emission of Auger electrons, where an electron occupies a vacancy in a lower energy band (see Figure 27). The photon emitted, resultant from this transition, is absorbed by another electron and the energy of the photon may be enough to cause ionization.

This mechanism "disturbs" the XPS analysis since the detector cannot discriminate photoelectrons from Auger electrons. However, as electrons Auger do not depend on the initial X-ray photon energy, but only on the difference in band energy, by using two X-rays sources with different energies it is possible to distinguish the photoelectrons from the Auger electrons. The emission of characteristic X-rays dominates for heavy elements and the Auger process occurs specially with light elements.

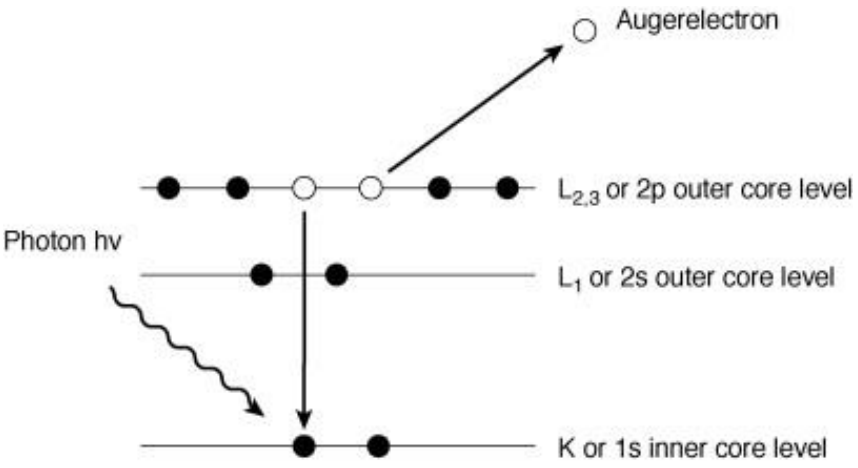

Figure 27: Schematic diagram of the Auger process. A core-level vacancy (such as created in Figure 26) is filled by an electron from a higher-level shell and a third electron is emitted to conserve energy. Note that the energy of the Auger electron is independent of the energy of the photon creating the core-level vacancy [99].

The binding energies of the outer shell electrons depend strongly on the bonding states of the atom, which make it possible to identify the elements present and their chemical state. This allows characterizing chemically the top of the surface of any solid supporting high vacuum, being it insulator or conductor. The XPS peaks position (binding energy) of an element may change by a few of eV (or tenth of eV) due to a change in the chemical bonding of that element. This effect is called chemical shift and the value of this shift, as well as its variation for lower or higher energies, usually depends on the valence state, electronegativity, proton affinity, electron density, and final state effect, i.e., electronic relaxation. For example, increasing the electron density in the atom that is being photoionized will decrease the measured binding energy or if the atom is bonded to a more electronegative element the binding energy increases and vice versa [98]–[100].

X-ray photoelectron spectroscopy (XPS, Kratos Axis Ultra HSA, Manchester, UK) analysis was performed at CEMUP (Centro de Materiais da Universidade do Porto, Portugal). Data acquisition was performed using a monochromator Al X-ray source operating at 15 kV (90 W). The survey XPS spectra were acquired, with pass energy (PE) of 80 eV, 1 eV step size, 200 ms dwell time and averaged from two scans. High-resolution C1s and O1s XPS spectra were acquired averaging five scans, with PE of 40 eV, 0.1 eV step size, 1500 ms (for C1s), and 1000 ms (for O1s) dwell time. Spectra were then analyzed using CasaXPS software (Casa Software Ltd., Teignmouth, UK). The contribution of the electric charge was corrected by calibrating all samples to the carbon peak reference at a binding energy of 284.6 eV.

2.5.4. Atomic force microscopy

The atomic force microscopy (AFM) allows to study a range of properties of the materials that are much broader than topography and inhomogeneity in composition of materials, at the nanoscopic scale. The correct selection of each different operating mode possibly to study an extremely wide range of material properties (geometry, viscoelastic, mechanical, electrical, magnetic properties, etc.) both at pressure and ambient temperature as under ultra-high vacuum or cryogenic temperatures and can also be combined with magnetic fields or other techniques such as Raman spectroscopy. This technique is characterized by being non-destructive, making it possible to “map” substrates, coatings and others surfaces, deduce the structure of terminated substrates after chemical treatment and deduce physical properties. An experiment of AFM is based on the principle of electrostatic interaction, between the atoms of a very thin tip (typical with a few micrometers in length and a radius of curvature around 5 - 100 nm) with the

atoms of the sample surface to be analyzed. The measurements of the deflections suffered by the stem which handle the tip, commonly called a probe, are realized on a photo detector that captures the displacement of the reflected laser focused on the opposite surface of the tip and convert the oscillations of the probe position into images that represent the surface topography through computational resources with nanometric precision (Figure 28). The movement of a piezoelectric element (piezo scanner), which supports a sample, changes its position in relation to the tip, yielding a constant force. This force depends on several factors such as the tip-sample distance, the tip geometry, the materials that make up the surface and the tip, and even any contamination that is present on the sample surface.

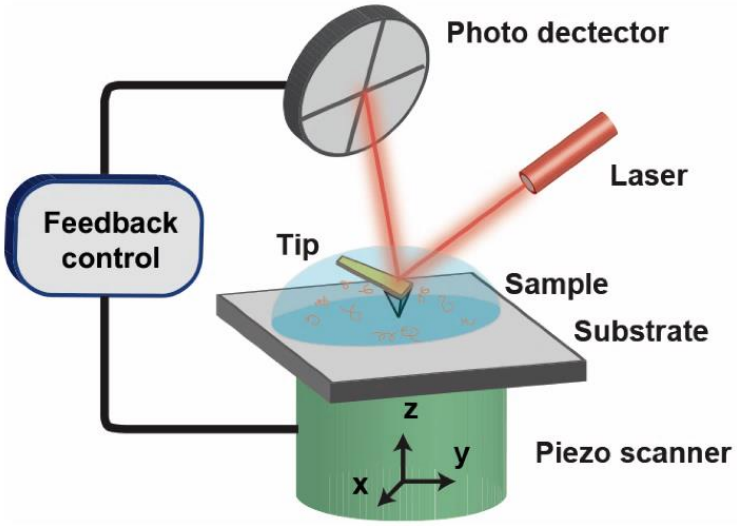

Figure 28: Schematic representation of an atomic force microscopy system [101].

There are several modes of operation of the AFM that enable image acquisition of various types of surfaces and are strongly dependent on the distance between the tip and the sample at the time of scanning. These operating modes, also known as scanning mode, are classified into: (i) contact, (ii) non-contact and (iii) intermittent contact (or dynamic force mode). Such classifications depend on the forces between the tip and the sample. In contact mode operation (repulsive region), the atoms of the tip and the surface are so close that their electronic orbitals begin to repel, and the stem is moved away from the sample and the repulsive forces that come from Pauli's exclusion principle star to act. In the non-contact mode (attractive region), at greater distances between the tip and the sample, the stem bends in the direction of the sample just when the tip approach starts predominating van der Waals forces. The intermittent contact mode operates either in an attraction or in repulsion regime, that is, the stem is forced to vibrate at a

defined frequency and at a certain distance from the sample, so that the sample is touched periodically by the tip.

In this work the equipment was used from the user's point of view with technical support with an Atomic Force Microscopy performed in contact mode using a *NT-MDT Ntegra Aura* and respective *Nova_Px 3.4.0* interface software. Commercial Pt coated doped silicon probes from *NT-MDT*, with curvature radius of 10 nm, resonance frequency ~130 kHz and spring constant of 3 N/m, were used. The topographic images were edited via *WSxM 5.0 8.0* software, belonging to the CICECO of the University of Aveiro.

2.6. Physical characterization

2.6.1. Dielectric and electrical properties

In order to perform these kinds of measurements in the as-produced films, we have firstly to choose the best type of electrodes to be used. We have preferred to implement interdigital electrodes instead of the usual buffer layer between the film and the substrate towards preventing other parameters from interfering with the epitaxy of the film during its production, as well as overcoming the high response of the $SrTiO_3$ substrate that can overlap the one from the film. Moreover, rare-earth manganites are known to be relatively prone to current losses or even tunneling within such nanometer scale, which would hamper dielectric and polar measurements.

2.6.1.1. Interdigital electrodes

The interdigital electrodes (IDEs) were fabricated using conventional photolithography and etching following the procedure, in the cleanroom at CEMUP (University of Porto) and at INESC-MN (Instituto Superior Técnico, University of Lisbon) [102].

The *AZ 1505 Microchemicals* photoresist was first spread over the film with a spinner *Headway Research Inc PWM32-PS-R790* and then dried by soft bake in a hotplate at 100 °C during 1 minute. After this, a *Heidelberg Direct Laser Writer uPG10* was used to design on the photoresist and then develop with an appropriate solvent. The required IDEs pattern was used as a mask to remove the surplus material by ion milling in a *Nordiko3600* system with a broad Argon beam of 40 mA (~ 130 μA/cm^2) at a pressure of 0.2 mTorr.

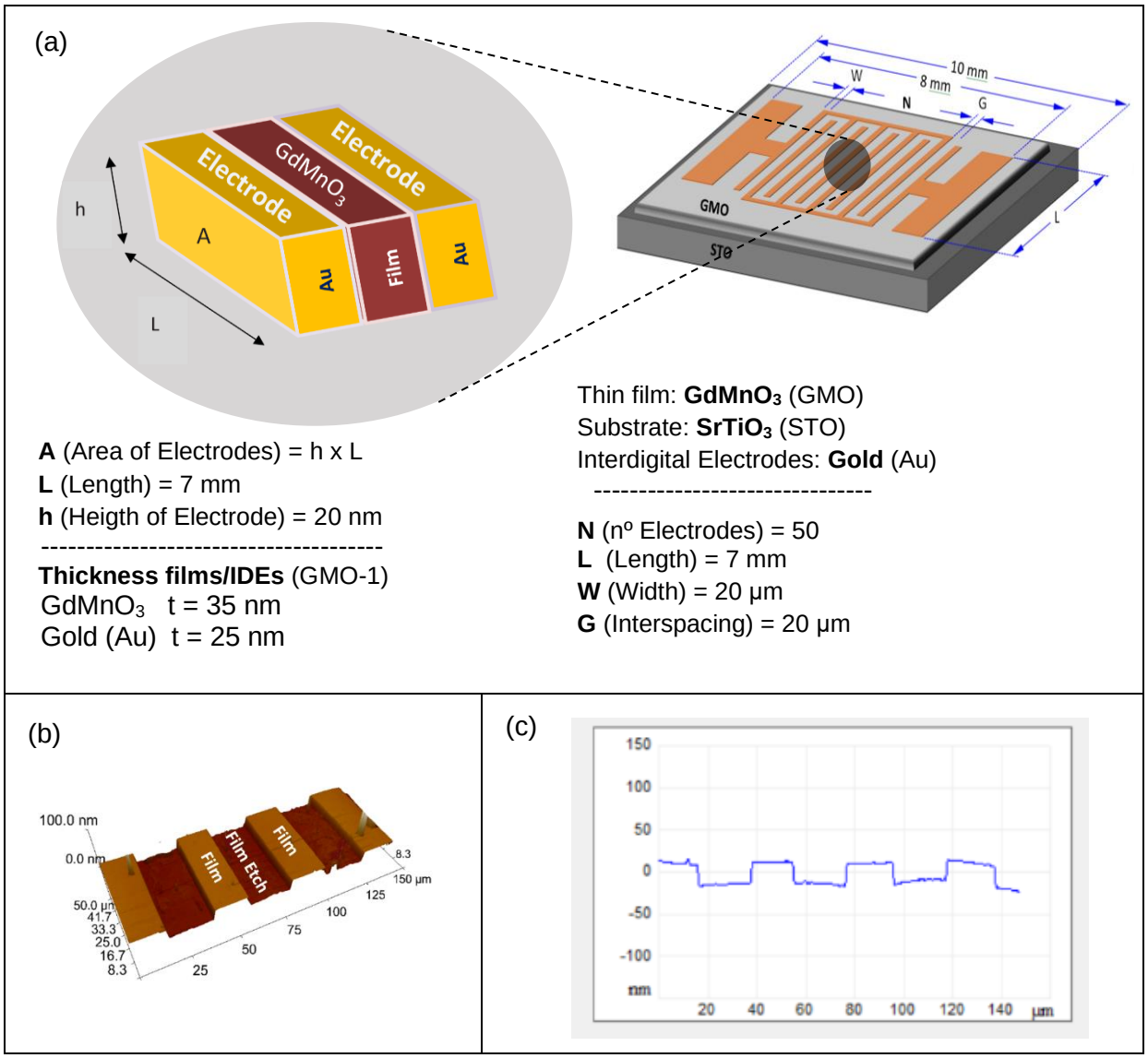

Figure 29: (a) Schematic representation of IDEs implemented in $GdMnO_3$ thin films, (b) three-dimensional AFM topography image and (c) step height of the IDEs structure before gold deposition of sample GMO-1.

The IDEs consist of N = 50 gold electrodes, deposited by evaporation using an *Edwards e-beam evaporators Auto 306*, filling the trenches previously made by ion beam etching (see Figure 29 (a) and (b)) and after removed by lift-off the resist and the corresponding excess of gold. These electrodes have length L = 7 mm, width W = 20 µm, interspacing G = 20 µm and depth of about 75 % of the thickness (*t*) of the deposited film, in order to avoid a significant dielectric response coming from the substrate. The lithographed IDEs on the prepared $GdMnO_3$ films show a regular pattern of 20.0 ± 0.5 µm wide channels and steps as it is shown in Figure 29 (b) and (c).

The total capacitance C_{Total} involving the interdigital electrode arrangement will be needed to obtain the complex electric permittivity of the film referred to in section 2.6.1.2. The total capacitance of the N interdigital electrodes is equivalent to N-1 capacitors in

parallel, which corresponds to the sum of N-1 capacitors. In our case, each capacitor is relatively similar and can be calculated by multiplying the capacitance of one of them by N-1.

The capacitance C_{uc} of each two parallel planes is given by:

$$C_{uc} = \varepsilon_0 \frac{A}{d} \quad , \tag{2.6}$$

with ε_0, the absolute permittivity defined by:

$$\varepsilon_0 = \frac{1}{c_0^2 \mu_0} = \frac{1}{3595027149.47\,\pi}\frac{F}{m} \approx 8.8542 \times 10^{-12}\ \frac{F}{m} \quad , \tag{2.7}$$

being *A* the vertical electrode area, and *d* the interspacing between the electrodes.

By making full use of symmetry and neglecting the capacitances of the edges, the total capacitance of the IDEs is calculated by:

$$C_{Total} = C_{uc}\,(N-1) \quad , \tag{2.8}$$

where *N* is the number of unit cells in the capacitor and *L* is the length of the electrode fingers. This capacitance model is valid in the presence of an isotropic dielectric film. As

$$A = L \times h = (7.0 \times 10^{-3}) \times (20 \times 10^{-9}) = 1.4 \times 10^{-10}\ m^2 \tag{2.9}$$

and

$$C_{uc} = 8.85 \times 10^{-12}\ \frac{1.4 \times 10^{-10}}{20 \times 10^{-6}} = 6.19 \times 10^{-16}\ F \tag{2.10}$$

we obtain for the total capacitance, using

$$C_{Total} = (N-1) \times C_{uc} \quad , \tag{2.11}$$

$$C_{Total} = (49) \times 6.19 \times 10^{-16} = 3.05 \times 10^{-14}\ F \tag{2.12}$$

2.6.1.2. Complex electric permittivity

The dielectric characterization of the $GdMnO_3$ thin films, deposited onto (100) and (110) - oriented $SrTiO_3$ substrates, was performed from 8 K to 300 K both in cooling and heating runs, with a temperature rate of 0.5 $K.min^{-1}$, and an accuracy better than 0.1 K. The measurements were performed by using an HP4284A impedance analyser from IFIMUP, University of Porto, under an AC electric field of amplitude around 1 V/m in the frequency range from 1 kHz to 1 MHz.

In the frequency domain, the complex electric permittivity can be expressed as follows:

$$\varepsilon^*(\omega) = \varepsilon'(\omega) - i\varepsilon''(\omega) \tag{2.13}$$

Assuming that the impedance has only a resistive and capacitive contribution, the equivalent circuit of the sample is as follows:

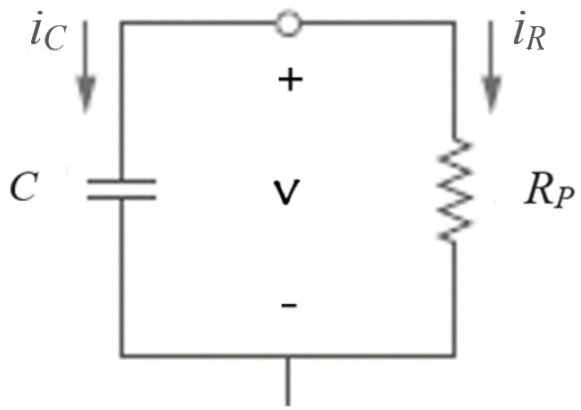

Figure 30: Schematic representation of the equivalent RC circuit.

Where C is the film capacitance and R_P the resistance. From here we can write $\varepsilon'(\omega)$ and $\varepsilon''(\omega)$ as follows [103]:

$$\varepsilon'(\omega) = \frac{C}{C_{Total}} \tag{2.14}$$

and

$$\varepsilon''(\omega) = \frac{1}{\omega\, C_{Total}\, R_p} \tag{2.15}$$

The capacitance C_{total} is obtained following the procedure presented in section 2.6.1.1.

We can also relate the complex dielectric permittivity with the electric displacement *D (ω)* and the electric field *E (ω)* [104]:

$$\varepsilon^*(\omega) = \frac{D(\omega)}{E(\omega)}\, e^{i\delta} \iff \varepsilon'(\omega) - i\varepsilon''(\omega) = \frac{D(\omega)}{E(\omega)}\,[\cos(\delta) - i\,sin(\delta)] \quad (2.16)$$

where the angle δ is a measure of the circuit losses and its given by:

$$tg(\delta) = \frac{\varepsilon''(\omega)}{\varepsilon'(\omega)} \quad (2.17)$$

To obtain the real and imaginary parts of the complex electric permittivity, we have then the expressions:

$$\varepsilon'(\omega) = \frac{C}{C_{Total}} \quad (2.18)$$

and

$$\varepsilon''(\omega) = \varepsilon'(\omega)\,.\,tg(\delta) \quad (2.19)$$

The experimental set-up used to measure the complex electric constant as a function of the temperature and frequency, is shown in Figure 31. It consists of an HP4284A impedance analyzer and an Agilent 34401A digital multimeter, both linked to a home-made data acquisition and control system, a closed-cycle He cryogenic system, equipped with a sample-holder, to which a calibrated diode is attached.

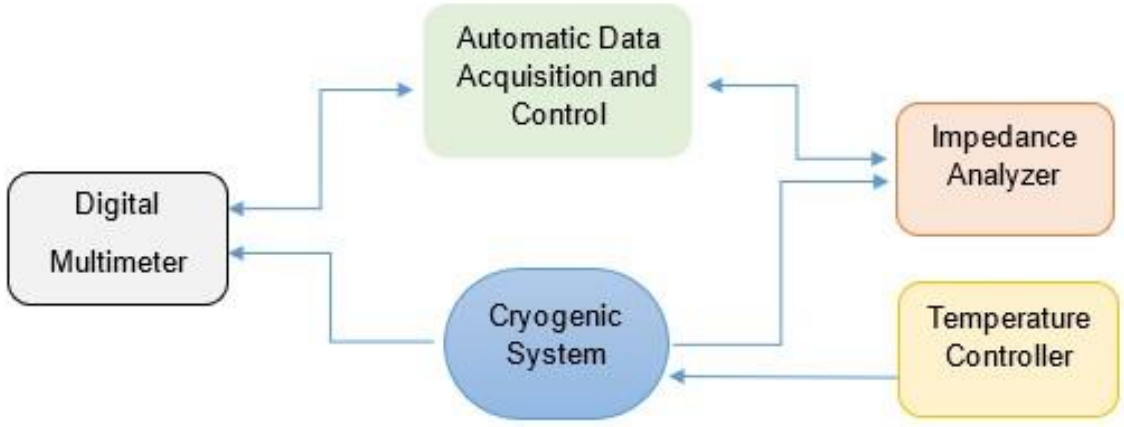

Figure 31: Diagram of experimental SET-UP used to study the complex dielectric constant.

The data acquisition and control system consist of a computer and a LabView® program, which enable to record automatically the data, to change the measuring AC electric field amplitude and frequency, and to control the temperature using an interface mediated temperature controller LakeShore 331. The cryogenic system is made of an APD HC-4 closed-cycle He cryostat, working in the 10 - 300 K temperature range with a temperature stability about ± 0.2 K.

2.6.1.3. Thermally stimulated depolarizing current

The polar characterization of the $GdMnO_3$ thin films was obtained through the measurement of the thermally stimulated depolarization current (TSDC) as a function of temperature. This technique consists of recording electric current generated by heating up the film, which was previously polarized by cooling it down under a fixed polarizing electric field. The electric current stems from the temperature dependence of the electric polarization. The experimental procedure implemented started with the application of a DC bias electric field, E_p, at a high temperature T_p, and then the sample is cooled down with the electric field still applied, until a lower temperature T_0 (which must be low enough to avoid depolarization by thermal excitation). After the field-cooling process, the poling electric field is removed and the electrodes of the sample short circuited in order to release spurious electric charges. Then, the sample is heated up and the electric current is measured. The corresponding current density, $J(T)$, is associated with the polarization variation as follows [105]:

$$J(T) = \frac{dP(T)}{dt} = \frac{i(T)}{S} \tag{2.20}$$

Here P(T) is the electric polarization, and S is the area of electrodes. The temperature dependence of the electric polarization is obtained by time integration of the TSDC current and was measured in the in-plane film orientation.

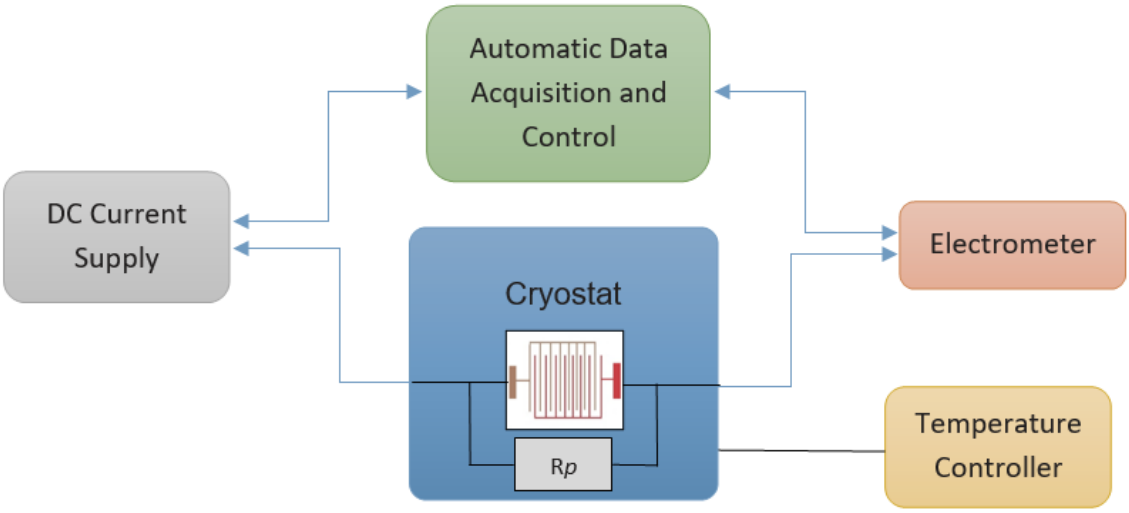

Figure 32: Diagram of experimental SET-UP used for the measurement of TSDC.

Figure 32 shows a schematic representation of the set-up used for the measurement of the TSDC. The sample, provided with interdigital electrodes, is placed in the sample-holder of a closed-cycle He cryostat.

The high voltage power supply, Stanford Research System, model PS350, enables us to apply a DC voltage up to 5000 V. A programmable Keithley 617 electrometer is used to measure the potential difference on the terminals of the sample. As the current intensity is of the order of magnitude of 1 pA, a calibrated electric resistance R*p* = 10^{10} Ω is connected in parallel to the sample, in order to improve the resolution of the current intensity measurement. The experimental set-up enables a current measurement accuracy better than 0.1 pA.

The data acquisition and control system are achieved with a homemade LabView® program, enable automatically to record the current intensity measured during heating run in short-circuit conditions, for different heating rates at IFIMUP, University of Porto. Different poling electric fields were applied during the preceding cooling process, all bellow 30 V/mm to avoid inducing non-spontaneous phenomena and a 30 min short-circuit is performed at the lowest temperature (10 K) and before current measurements.

In critical phenomena, like ferroelectricity, the temperature at which the electric polarization changes is independent of the temperature rate but the relaxation phenomena are directly dependent on the temperature rate. To distinguish these two processes, temperature rates from 2 to 10 K/min were used.

2.6.2. Magnetic properties

The magnetic characterization was performed by measuring the magnetization using a SQUID magnetometer that consists of an integrated device with a superconducting coil in a helium bath and a corresponding control system. This system allows accurate magnetization measurements in the 5 - 350 K temperature range and under magnetic fields up to 5 T and a sensitivity reaching 10^{-8} emu.

The SQUID magnetometer is basically made up of three parts (Figure 33): a system to control the temperature, another system responsible for the application of the magnetic field and a detection system used to measure the magnetic moment through the movement of the sample along the detecting coils, by a superconducting ring made up of two Josephson junctions that are highly sensitive to variations in the magnetic flux associated to the Meissner effect. The flow variation induces electrical current that is converted by the coupled SQUID detection circuit into an output voltage proportional the magnetic moment of sample.

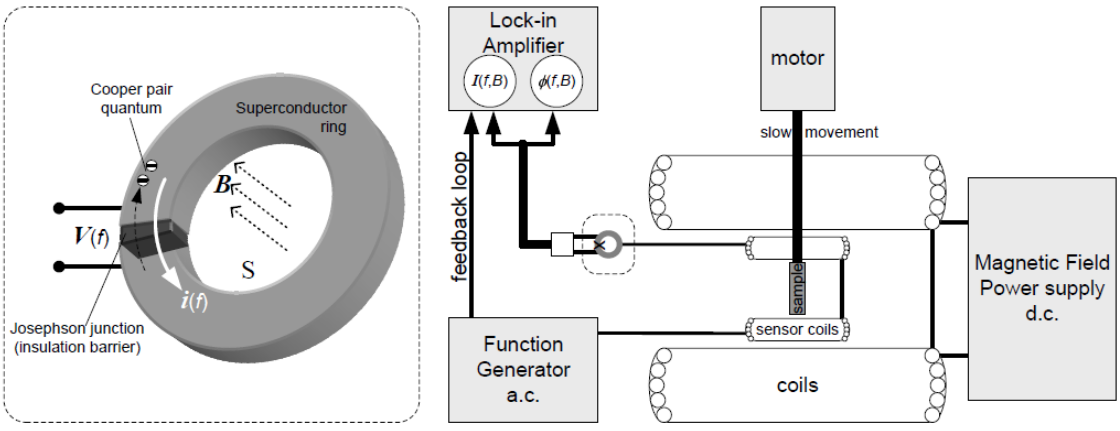

Figure 33: Simplified diagram of the Josephson junction (left) and of the a.c. SQUID magnetometer system (right) [89].

The low field temperature dependence of the magnetization was measured in heating runs. The measurements were made previous cooling down to 5 K under 0 Oe applied magnetic field (zero-field cooling run - ZFC) and then cooling down to 5 K under between 50 Oe and 100 Oe (field-cooling run - FC).

Isothermal magnetic hysteresis loops measurements, M(H), were performed for different fixed temperatures, as a function of the applied magnetic field, which varied from -5 to 5 T to obtain the saturation magnetization (M_{sat}) and the coercive fields (H_c). The internal dynamics of the magnetic properties were studied by complex magnetic AC susceptibility measurements using driving frequencies from 1 to 1000 Hz.

The magnetic properties measurements were carried out in a commercial (MPMS Quantum Design) Superconducting Quantum Interference Device (SQUID) magnetometer at IFIMUP, University of Porto, used in the temperature range from 5 K to 370 K, in reciprocating sample option (RSO) mode with a sensitivity of ~ 10^{-7} emu. The isofield M(T) curves were measured under an applied field of 100 Oe and the isotherms M(H) curves were measure between 0 and 50 kOe from 10 K to 300 K.

For SQUID analysis, thin films were cut into an elongated shape (5x2x1 mm^3) and placed with cotton in a polyethylene capsule, which in turn is placed in the center of a plastic straw. This kind of measurement makes it possible to identify magnetic transitions (critical temperatures) and to characterize the type of magnetic ordering. Being the obtained magnetization the total result of the sum of the film's magnetization plus the substrate's magnetic signal and in order to correctly analyze the magnetic signal of the film, it was necessary to make a correction of the obtained magnetic signal from substrates, subtracting the previously value measured from the substrates without any film.

3. Strain Engineering $GdMnO_3$ Thin Films Using (001) and (110) STO Substrates

In this chapter, we will present a comparative study of the structure, dielectric and magnetic properties of $GdMnO_3$ epitaxial thin films, deposited by RF-magnetron sputtering onto (001) and (110) oriented $SrTiO_3$ substrates. The choice of deposition conditions and parameters are described in Chapter 2.

According to the substrate orientation, we will report outstanding different physical behaviours of the fully strained thin films relatively to the bulk. These features entirely corroborate the strain engineering ability to tailor profoundly their properties.

This chapter begins by presenting in section 3.1 the description of the experimental results obtained in fully strained thin films of $GdMnO_3$ deposited onto (001) STO substrates ($GdMnO_3$/(001)-STO), and then, in section 3.2, we present those ones obtained in fully strained thin films of $GdMnO_3$ deposited onto (110) STO substrates ($GdMnO_3$/(110)-STO). Finally, in section 3.3, we will address the key role of the substrate orientation on the film properties.

The Table 3 summarizes the mains features of the $GdMnO_3$ thin films deposited onto $SrTiO_3$ crystalline substrates with (001) and (110) orientations.

Table 3: Name and thickness value of $GdMnO_3$ thin films, deposited onto (001) and (110) oriented $SrTiO_3$ substrates.

Samples	Deposition time (min)	Thickness (nm)	Substrate orientation
GMO - 0	120	250 ± 6	(001)-STO
GMO - 1	20	35 ± 1	(001)-STO
GMO - 2	20	40 ± 1	(001)-STO
GMO - 3	20	44 ± 1	(110)-STO
GMO - 4	60	120 ± 3	(110)-STO

After a previous study of the deposition conditions, we chose to use a deposition time of 20 min, as these films were the ones that showed the most reliable results. As it is our goal to use non-relaxed fully tensioned films, a low thickness is required to obtain suitable results, though we should have enough material that enables to perform various analysis using the available techniques. It is noteworthy that thin films deposited under the same conditions have similar structural properties, and thus we will focus on the films with the best deposited characteristics in each of the different substrate orientations that are GMO-1 and GMO-3 thin films. These films are considered as representative of a set of thin films, which were produced and structural characterized.

3.1. Thin Films of $GdMnO_3$ Deposited on (001)- $SrTiO_3$ Substrates

Summary: An unreported tetragonal phase was discovered in an epitaxially strained $GdMnO_3$ thin film deposited on a (001)-oriented $SrTiO_3$ substrate by RF-magnetron sputtering. The tetragonal axis of the films grown up to 35 nm thickness is perpendicular to the film surface and the basal lattice parameters are imposed by the cubic structure of the substrate. Furthermore, the emergence of a spontaneous electric polarization below ~ 31 K discloses the stabilization of an improper ferroelectric phase at low temperatures, which is controversal in $GdMnO_3$ bulk. These results reveal how strain engineering can be used to tailor the structure and properties of strongly correlated oxides.

3.1.1. Chemical composition and morphology

Figure 34 shows a representative cross-section SEM image of the GMO-1 thin film. It exhibits a dense and uniform layer, with a good adhesion to the substrate without structural defects or cracks. The average thickness is 35 ± 1 nm.

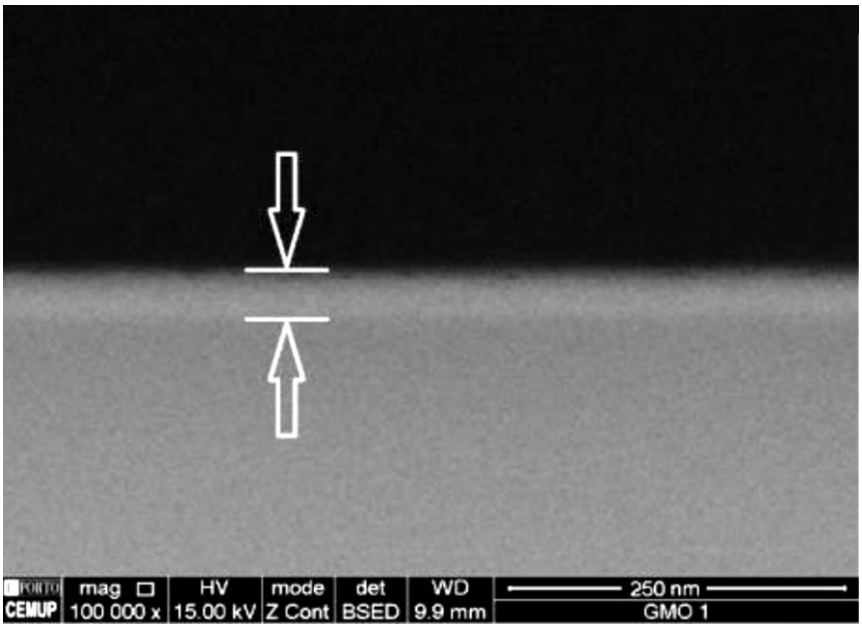

Figure 34: Representative SEM cross-section image of the GMO-1 film (35 nm thickness).

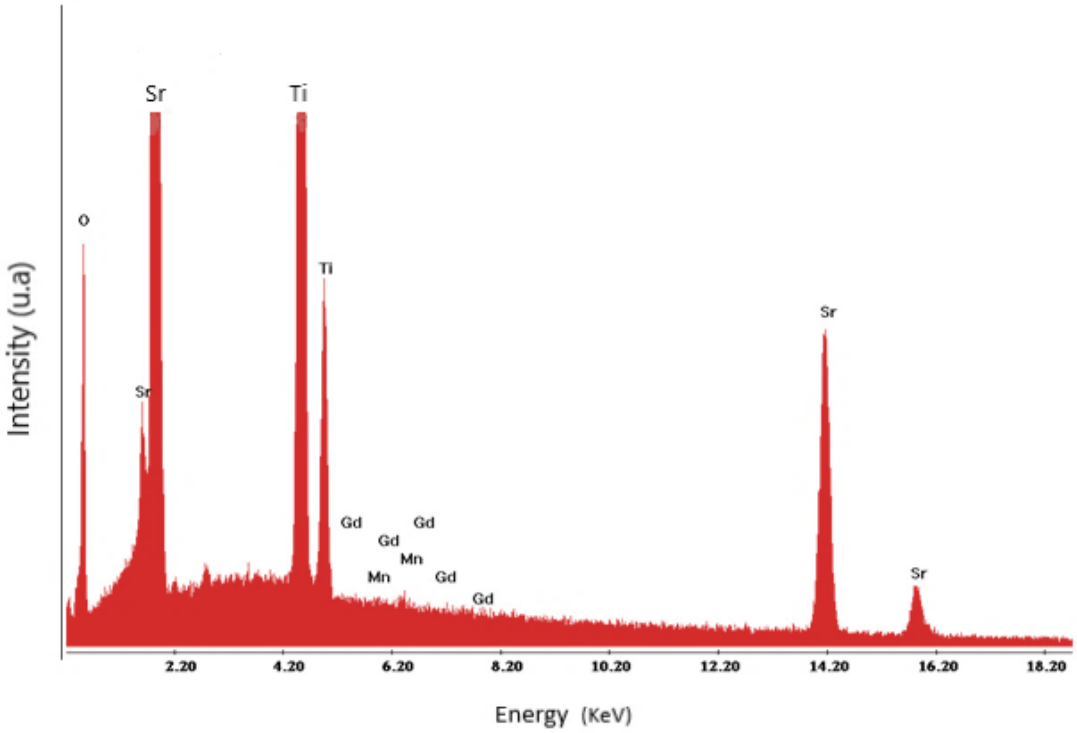

Figure 35: Energy dispersive X-ray spectroscopy spectrum of the elements in the GMO-1 film.

Energy dispersive X-ray spectroscopy (EDS) measurements of the GMO-1 film is shown in Figure 35. The EDS spectrum is dominated by peaks assigned to Ti and Sr elements of the substrate. Peaks assigned to Gd and Mn are hard to be observed. Nevertheless, the results confirm the presence of the Gd and Mn elements with a ratio of ~ 0.9, for an incident electron accelerating voltage (15-30 kV). Hence the Gd:Mn ratio can be estimated close to 1, within a 20% error margin for both Gd and Mn atomic ratio. Such error margin amount is expected due to the hindering diffraction effects of the reduced film thickness and film-substrate interface [106].

Table 4: Table obtained by EDS with the elements presented in the GMO-1 film.

Element	Wt %	At %	K-Ratio
O K	84.9	97.5	0.636
Mn K	3.6	1.2	0.029
Gd L	11.5	1.3	0.081
Total	100.0	100.0	

The XPS spectrum of the binding energy of the Mn 3*s* orbitals enables to distinguish the Mn oxidation states [107]. As seen in Figure 36, the characteristic splitting between the correlated local maxima of the multiplet peaks are estimated between 5.0 and 5.3 eV, corresponding to the overall presence of Mn^{3+}, associated with shorter Mn-O distances found in films, as described by Rubi *et al*. [38]. The XPS spectrum shows no traces of the reduced Mn^{2+} and the oxidized Mn^{4+}, which would be formed if oxygen stoichiometry was not verified. In this way, we conclude that the film exhibits the correct $GdMnO_3$ stoichiometry, without a significant amount of oxygen vacancies, which would promote changes on the physical properties other than those arising from the epitaxial strain.

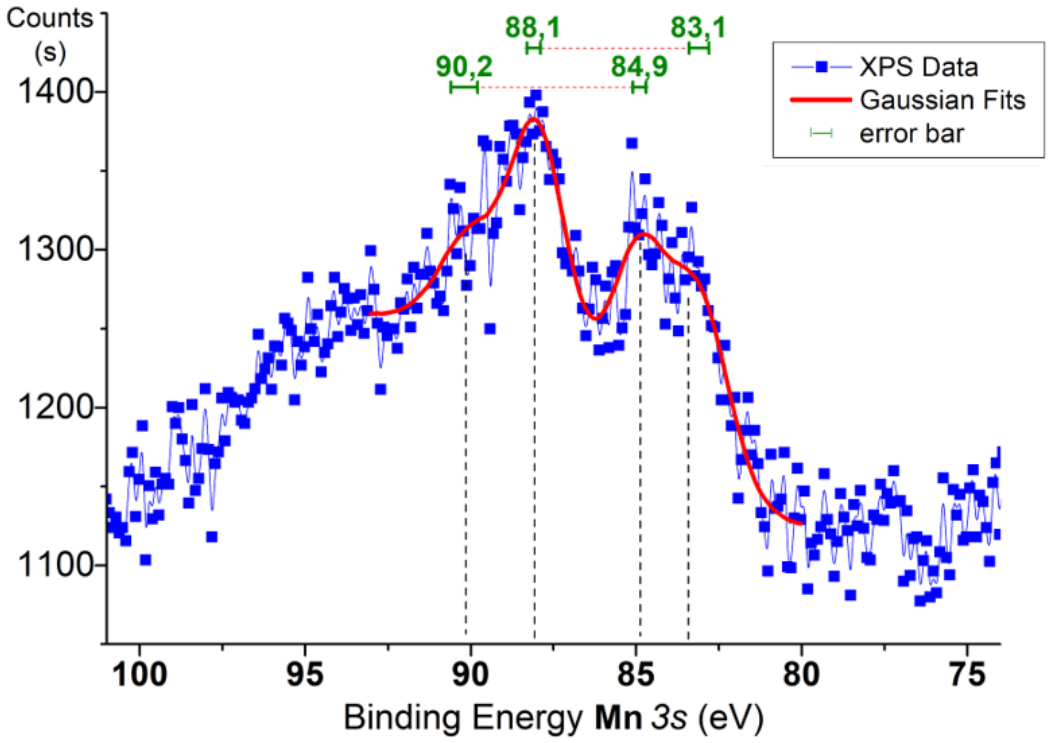

Figure 36: Representative XPS spectrum, in the 75 – 100 eV energy range of the as process GMO-1 film.

Figure 37 shows a representative AFM topography image and respective histogram of the GMO-1 film. These scans allow inspecting both local and overall film topography, confirming the smoothness and homogeneous quality of the film surface. The film average roughness, within a representative 2 x 2 μm^2 area, was estimated to be close to 0.3 nm, which is within the scale of the $SrTiO_3$ unit cell. This result is consistent with the random atomic termination of the (001)-oriented STO substrate surface, found to be the primitive cell dimensions (a = 0.3905 nm). Additionally, this result points out for the excellent adhesion of the film to the substrate, the film following the substrate surface topography. This assertion is also corroborated by the SEM cross-section image (see Figure 34) which does not show gaps between film and substrate.

The overall results obtained from the SEM and AFM measurements clearly evidence for the requested interface quality, and thus achieving the adequate atomic connectivity between film and substrate, which is very relevant for strain-engineering purposes.

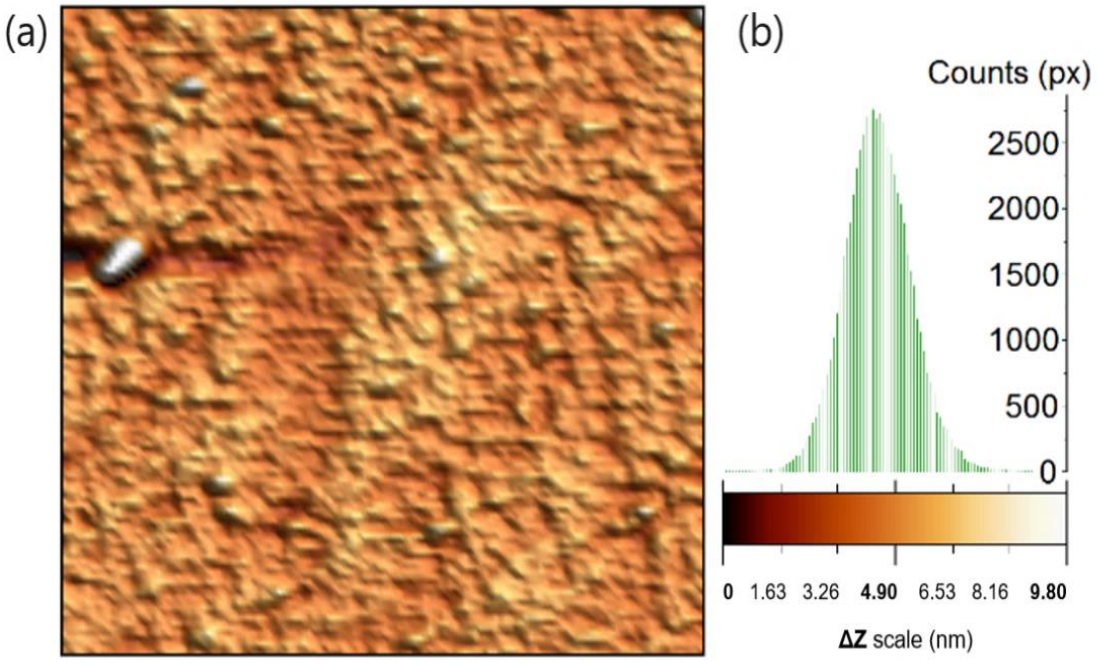

Figure 37: (a) Representative AFM topographic scan over 2 x 2 μm^2 area; (b) respective histogram of the GMO-1 film [108].

3.1.2. Structural characterization

Figure 38 shows a representative XRD pattern in the 20-60° 2Θ-range, recorded at room conditions of three $GdMnO_3$ thin films deposited onto (001)-oriented $SrTiO_3$, one sample with high thickness (GMO-0), representative of the bulk material and two others with very low thickness but similar (GMO-1 and GMO-2). It is worth to recall that in the following, the indexing of XRD peaks was performed by using the JCPDS cards for the respective phases.

The XRD pattern exhibits the strongest Bragg peaks approximately centered at 2Θ = 22.75° (001), 46.54° (002), 72.55° (003) and 104.24° (004), which are indexed to $SrTiO_3$ crystal, confirming the high quality and the (001)-orientation of the substrate, with a_{STO} = 3.905(0) Å (Figure 38 and Figure 39).

It is worth to stress that the XRD patterns recorded for these films do not clearly show the Laue´s oscillations. The lack of interference fringes is apparently due to the high quality of the epitaxial growth of the $GdMnO_3$ film, without an interface mismatch with the (001)-STO substrate. This result is in good agreement with the good adhesion of the film to the substrate already evidenced by SEM and AFM results.

In Figure 38 is clearly observed that the film GMO-0 presents two significant diffraction peaks centered at 2Θ = 23.92° and 2Θ = 48.95° which are indexed to reflections from the (020) and (040) planes of $GdMnO_3$, respectively. The calculations of the main parameter *b* obtained from these two peaks, when compared with the table JCPDS for $GdMnO_3$, has the same value *b* = 7.43(0) Å, indicating also that are at the same positions relatively to the $GdMnO_3$ bulk, confirming that this thicker film is relaxed [66].

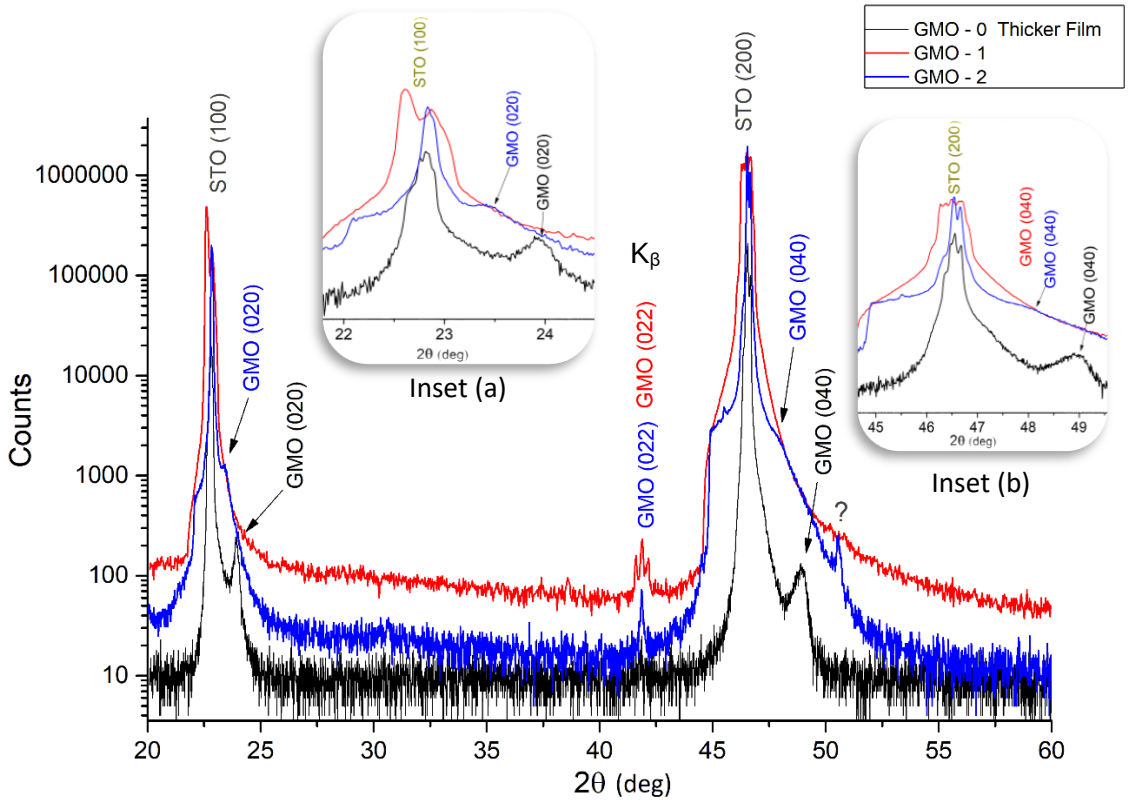

Figure 38: Extended range of the conventional (gonio) XRD patterns of $GdMnO_3$ / $SrTiO_3$ (001) films: GMO-0 (black), GMO-1 (red), and GMO-2 (blue). Insets a) and b) are detail views, wherein 2Θ ranges from 21° - 25° and 44° - 50°, respectively.

In Figure 38 it is possible to observe one small diffraction peak centered around 2Θ = 23.45° for the GMO-2 film, which can be indexed to (020) plane reflections. Contrarily, it is not undoubtedly observed the reflection peaks arising from (020) planes for the GMO-1 film. Moreover, the reflection peaks stemming from the (040) planes for both samples GMO-1 and GMO-2 could not also be clearly detected. To overcome this difficulty, we have registered XRD patterns with an offset of 1.5° for the GMO-1 and 1.2° for GMO-2 films. These results are shown in Figure 39 and in the detail views of Figure 40. In the Figure 40 a), the peaks indexed to reflections from planes (020) are clearly observed at

2Θ = 23.95° for the GMO-0 film, and at 2Θ = 23.45° for the GMO-1 and GMO-2 films. In the Figure 40 b), we observe the peaks indexed to reflections from planes (040) at 2Θ = 48.95° for the GMO-0 film, and at 2Θ = 47.94° for the GMO-1 and GMO-2 films.

The calculations of the main parameter *b* obtained from these two peaks for the films GMO-1 and GMO-2 has the value *b* = 7.64(0) Å, which exhibit an expansion of ~ 2.8 % compared with the value obtained for GMO-0 film or bulk $GdMnO_3$ (*b* = 7.43(0) Å), indicating that both thin films are strained.

The peak position shift of Δ(2Θ) ≈ 1° is fully consistent with the strain imposed by the substrate on the GMO-1 and GMO-2 films. Since it was found that there are no oxygen vacancies in these films or the oxygen stoichiometry is close to what is expected, it cannot stem from oxygen vacancies but instead from epitaxial growth.

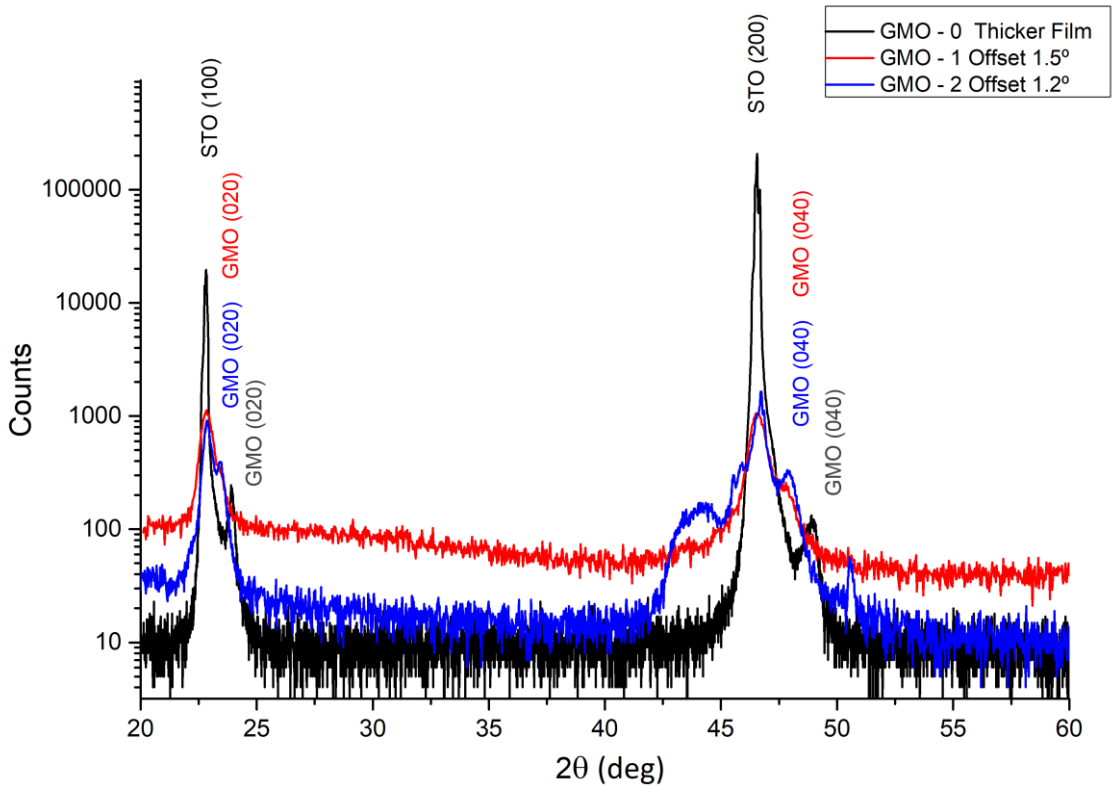

Figure 39: Extended range from 20° - 60° of the conventional (gonio) XRD patterns of $GdMnO_3$ / $SrTiO_3$ (001) films: GMO-0 (black), also GMO-1 (red) and GMO-2 (blue) with 1.5° and 1.2° angular off-set, respectively.

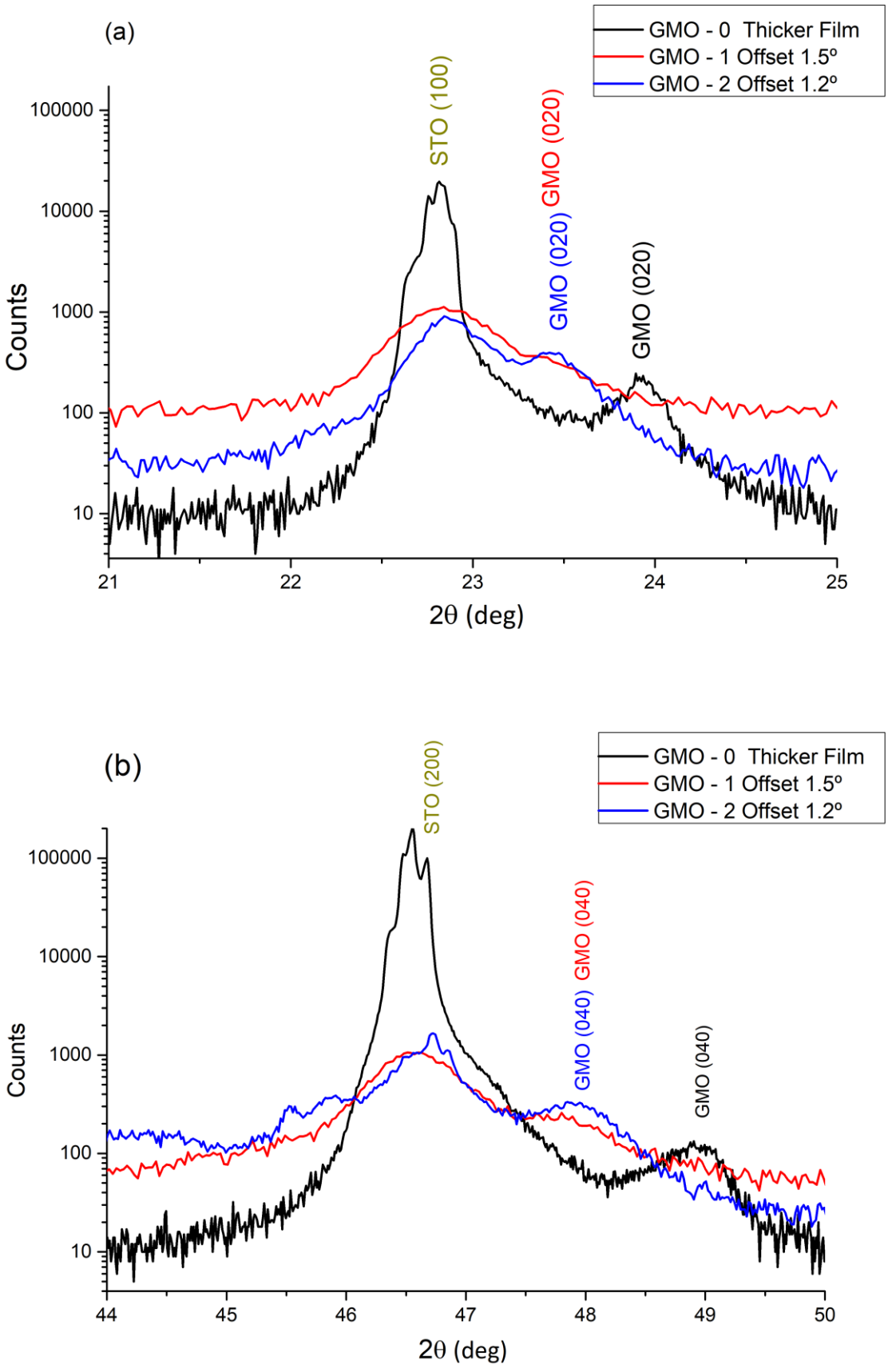

Figure 40: Extended range (a) 20° - 26° and (b) 44° - 50° views of the conventional (gonio) XRD patterns of $GdMnO_3$ / $SrTiO_3$ (001) films: GMO-0 (black), also GMO-1 (red) and GMO-2 (blue) with 1.5° and 1.2° angular off-set, respectively.

After detailed analysis of the X-ray spectra of $GdMnO_3$ films deposited on (001)-STO, it is possible to conclude that films deposited with low thickness (GMO-1 and GMO-2) show epitaxial deformation effects. The GMO-0 film with a thickness of 250 nm is already relaxed, showing structural properties similar to those of the bulk material, although it grows in the direction of *c*. It will not be further studied, and we will just focus on evenly tensioned films.

It is important to emphasize that the GMO-1 and GMO-2 films, processed under the same parameterized conditions, show similar residual stresses and structural properties. The GMO-1 film shows a slightly greater strain effect, and thus we will further focus our study on this film.

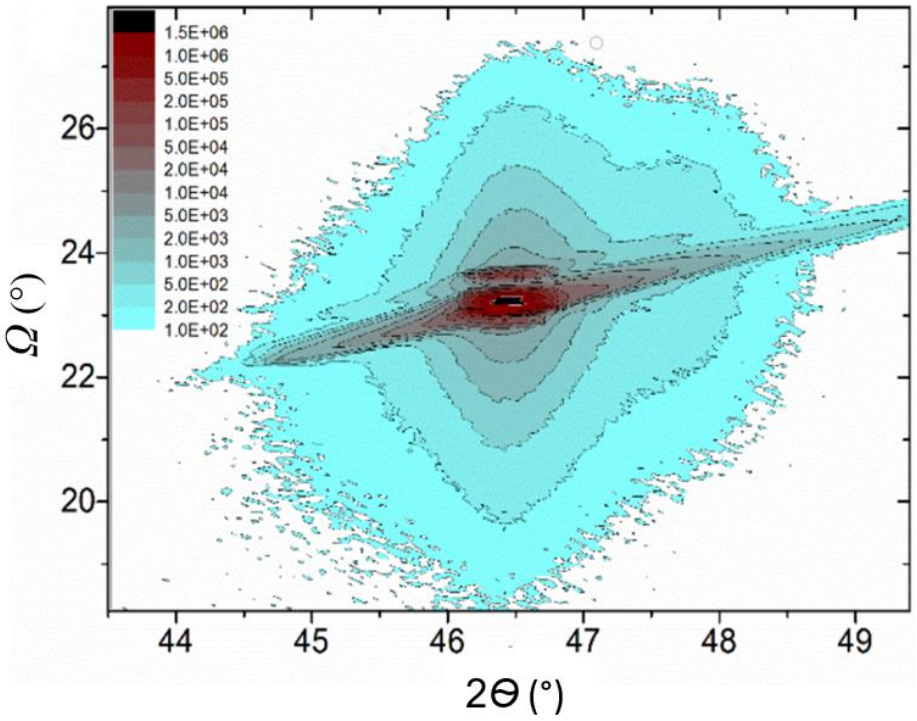

Figure 41: Projection in the (Θ, Ω) space coordinates of the symmetric reciprocal space map centered (RSM) at 2Θ = 46.47° and Ω = 23.23° for the GMO-1 film.

In order to get detailed information regarding the structure of the $GdMnO_3$ thin films we have performed a careful analysis of the XRD data. Figure 41 shows the symmetric reciprocal space map of the GMO-1 film centered at the main reflection peak arising from (002) STO planes, located at 2Θ = 46.47° and Ω = 23.23°. The single satellite reflection derived from the (040) GMO planes is only +0.4° offset in Ω and exhibits a small dispersion $\Delta(2\Theta) \leq 0.6°$, conforming the profile of the substrate peak, which is indicative

of the tight epitaxial growing of the film from the substrate. This result is in good agreement with the previous reported morphological analysis, presented in section 3.1.1.

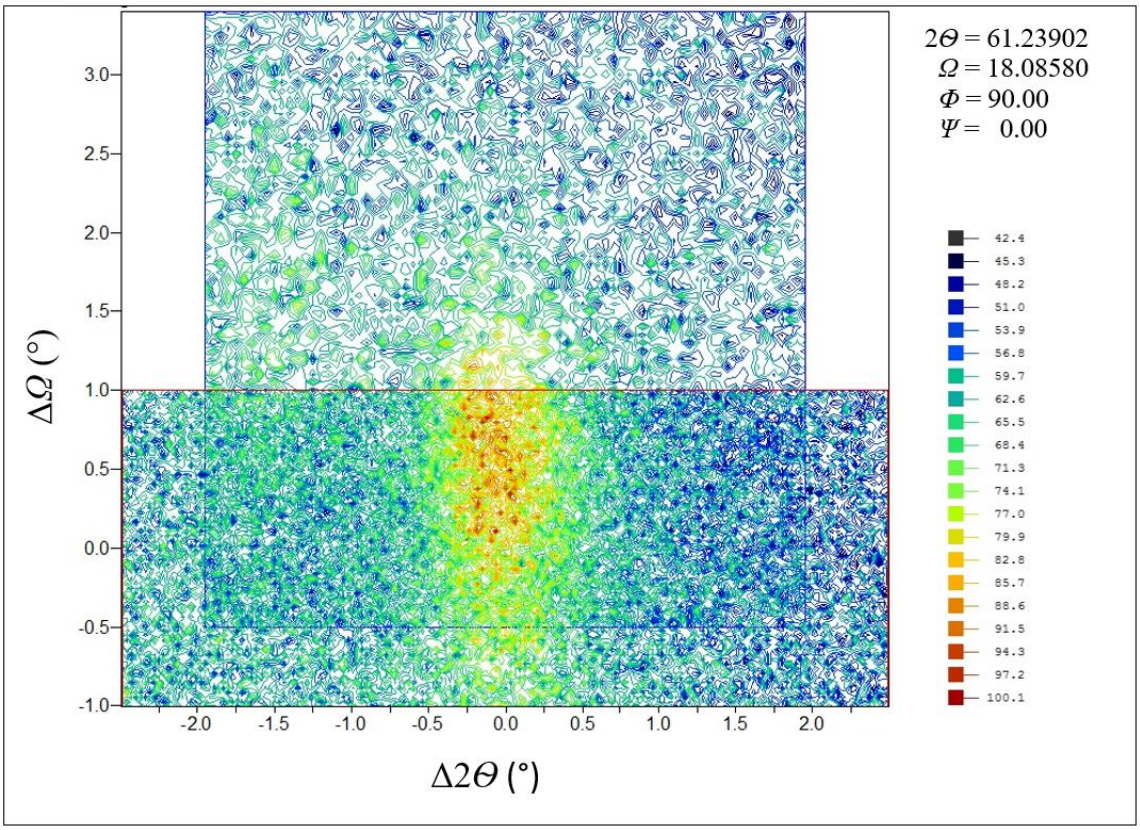

Figure 42: Projection in the (Θ, Ω) space coordinates of the asymmetric space map centered at 2Θ = 61.24° and Ω = 18.09° for GMO-1 film.

Figure 42 shows the asymmetric map of the GMO-1 film, centered at 2Θ = 61.24° and Ω = 18.09°, depicting a single peak, with a limited spread, with both $\Delta(2\Theta)$ and $\Delta\Omega \leq 1°$, indexed to the (203) planes. Observing the Figure 38, all the diffraction peaks arising from the GMO-1 film are well defined, relatively narrow and do not show mirroring, broadening nor diverging features from the respective centers. Consequently, there are no typical indications of maculae, neither domains due to a twinned crystalline structure, not even of significant lattice relaxation throughout the whole film thickness. Therefore, the film grows epitaxially in a single uniform crystallographic phase.

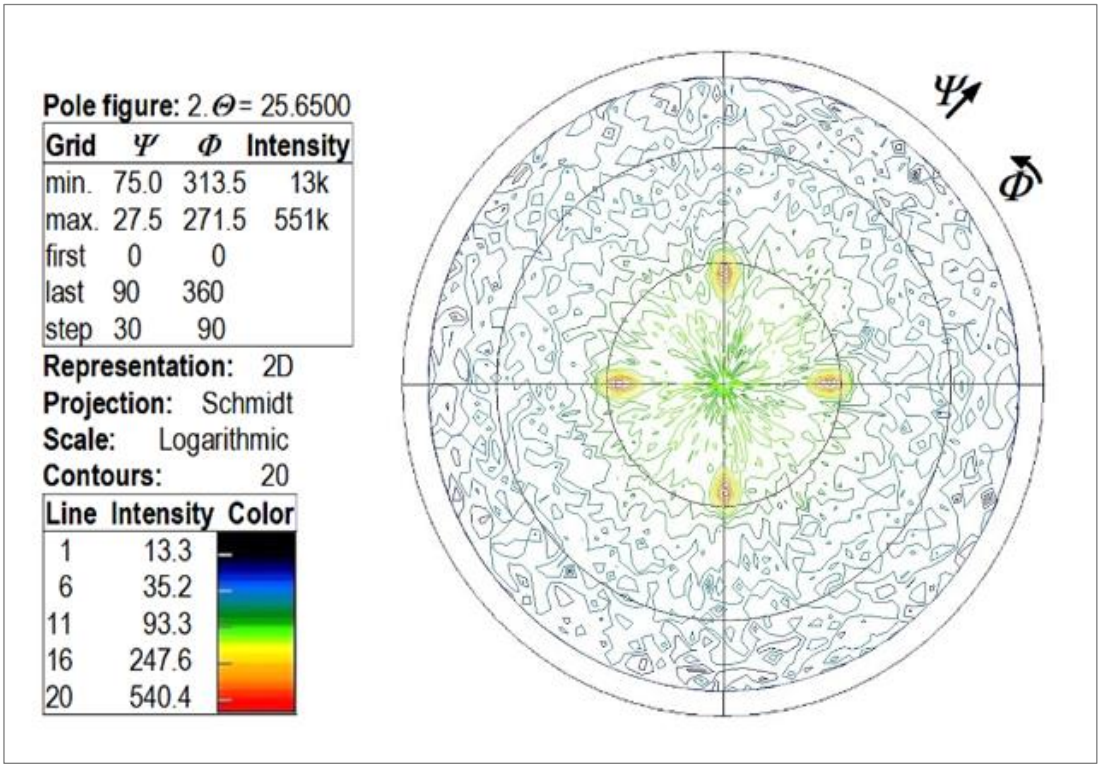

Figure 43: Symmetric pole figure obtained at 2Θ = 25.65°for GMO-1 film, corresponding to the 4 reflections of GMO (111) planes.

The symmetric pole figure presented in Figure 43, centered at 2Θ = 25.65° (d = 3.470 Å), encompasses and maximizes the reflections from the (111) planes of the GMO-1 film, whereas the STO (111) reflections are found at 2Θ = 39.96°. The projected 4-fold peaks clearly configure a square, which evidences that the in-plane a and c parameters of the $GdMnO_3$ film are forcibly identical. Moreover, these well-defined peaks are precisely aligned with the substrate edges corresponding to the respective (100)STO and (010)STO axes, which is a clear indication that the in-plane *a* and *c* axes of $GdMnO_3$ film are oriented at 45° to the in-plane STO axes. Accordingly, *a* and *c* are estimated to be 5.48(9) Å, approximately (-0.6%) the diagonal spacing $\sqrt{2}.a_{STO}$ = 5.522(5) Å of the substrate.

These sets of results are unequivocally consistent with a tetragonal symmetry with preferential oriented growth along *b* axis perpendicular to the substrate surface, as schematically represented in Figure 44.

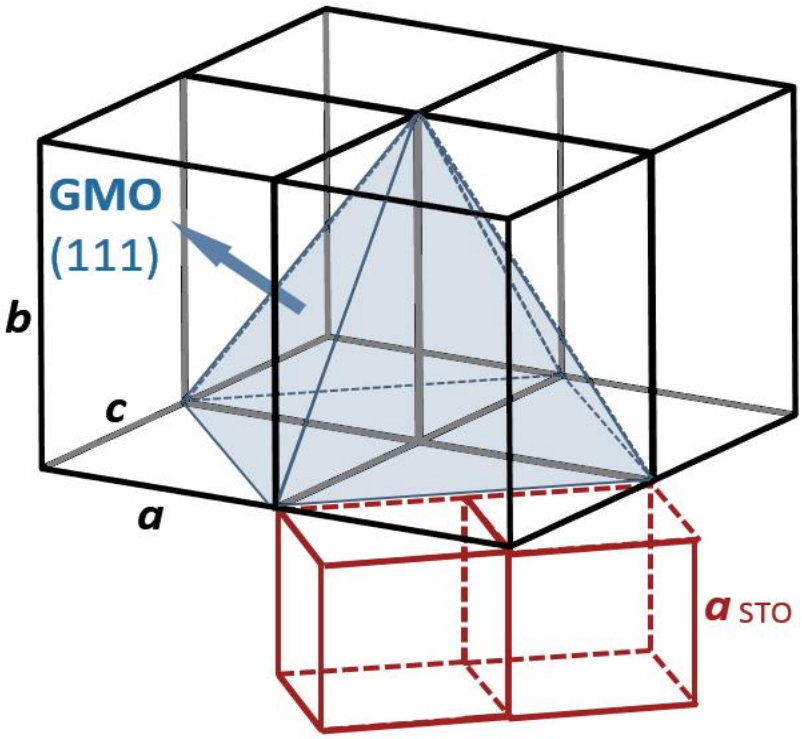

Figure 44: Schematics of the relative orientation of the tetragonal GMO-1 film onto (100)-STO substrate and the 4 reflections from planes (111).

These results demonstrate that the GMO-1 film does not follow the expected orthorhombic symmetry found in GMO-0 film with larger thickness, as well as in other films obtained using pulse laser deposition technique [46]. Possible effects of oxygen off-stoichiometry, that could be traced to an excess expansion of *b* parameter [106], are negligible and within the same ~ 1 % error margin of the calculated cell parameters. Bragg peaks that are ascribed to other crystallographic chemical phases could not be detected.

The GMO-1 film has an overall unit cell volume constrain of ~ 0.7 %, in comparison to the respective cell parameters of the bulk $GdMnO_3$ (a_o = 5.318 Å, b_o = 7.431 Å and c_o = 5.866 Å) [46], [66], [106], [109]. Moreover, the cell parameters of the tetragonal film phase undergo a remarkable alteration analog to an expansion of ~ 2.8 % in *b* and ~ 3.2 % in *c*, while *a* has ~ 6.4 % compression. Such significant values should be considered beyond a mere distortion of the orthorhombic phase.

3.1.3. Dielectric properties

Before presenting the experimental results, it is important to remember that for this purpose, interdigital electrodes were deposited on the films using conventional photolithography and etching, instead of the usual buffer layer between the film and the substrate to prevent other parameters from interfering with the epitaxy of the film during its production, as well as preventing the high response of the $SrTiO_3$ substrate that can overlap with that of the film (see more details in Chapter 2, section 2.6.1.1).

Figure 45 and Figure 46 show the temperature dependence of the real (*ε*') and imaginary (*ε*'') parts of the complex electric permittivity regarding the GMO-1 film, measured at different fixed frequencies, from 10 to 300 K, in a heating run. The real part of the electric permittivity exhibits dispersion for temperatures above 30 K, having a higher magnitude as temperature approach 30 K range from above. The shape of the *ε*'(T) curves is frequency dependent, wherein the relative maximum is obtained at ~ 55 K for the *ε*'(T) curve measured at 1 kHz.

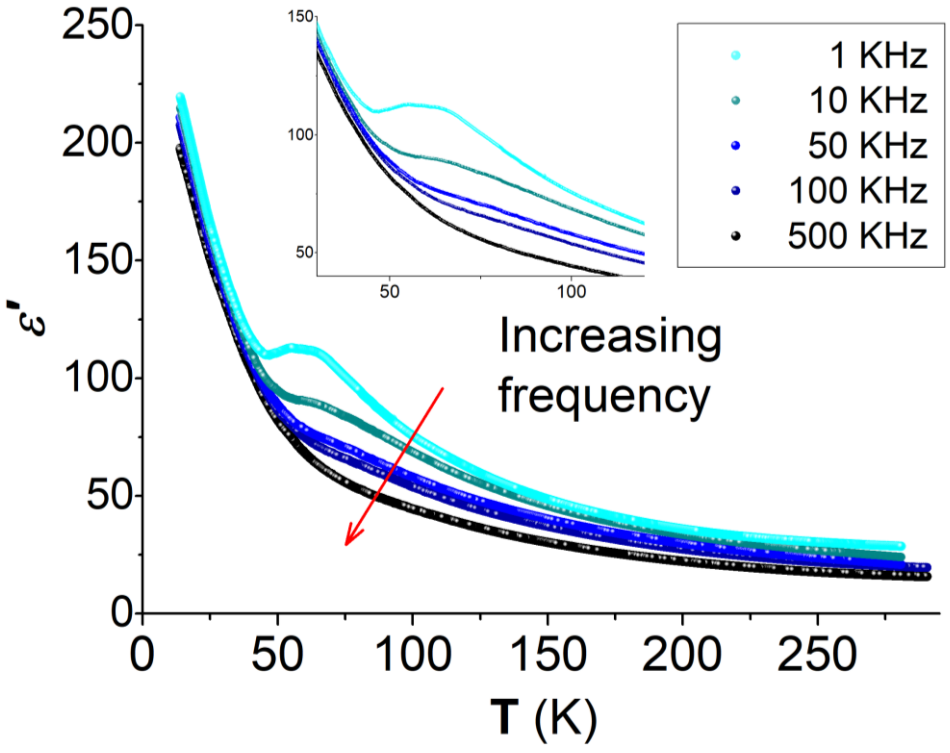

Figure 45: Temperature dependence of the real part of the complex electric permittivity of the GMO-1 film, measured at different fixed frequencies. Inset is a detail of increasing frequency.

As the frequency increases, the amplitude of the anomaly decreases and moves towards higher temperatures. In addition, the observed anomalies in the imaginary part of *ε*''(T) are also frequency dependent in the whole studied temperature range. These features

in ε'(T) and ε''(T) evidence for the existence of a dielectric relaxation process in the GMO-1 film, whose activation energy is 80 meV, higher than the 22 meV reported value found in bulk $GdMnO_3$ (see Figure 47) [110]. Although dielectric relaxation is intrinsic to $GdMnO_3$ (which has already been observed in the bulk) this relaxation phenomenon is sensitive to the strain imposed by the substrate on $GdMnO_3$. Further on, we will also see this dependence on the orientation of the substrate, which imposes another strain value.

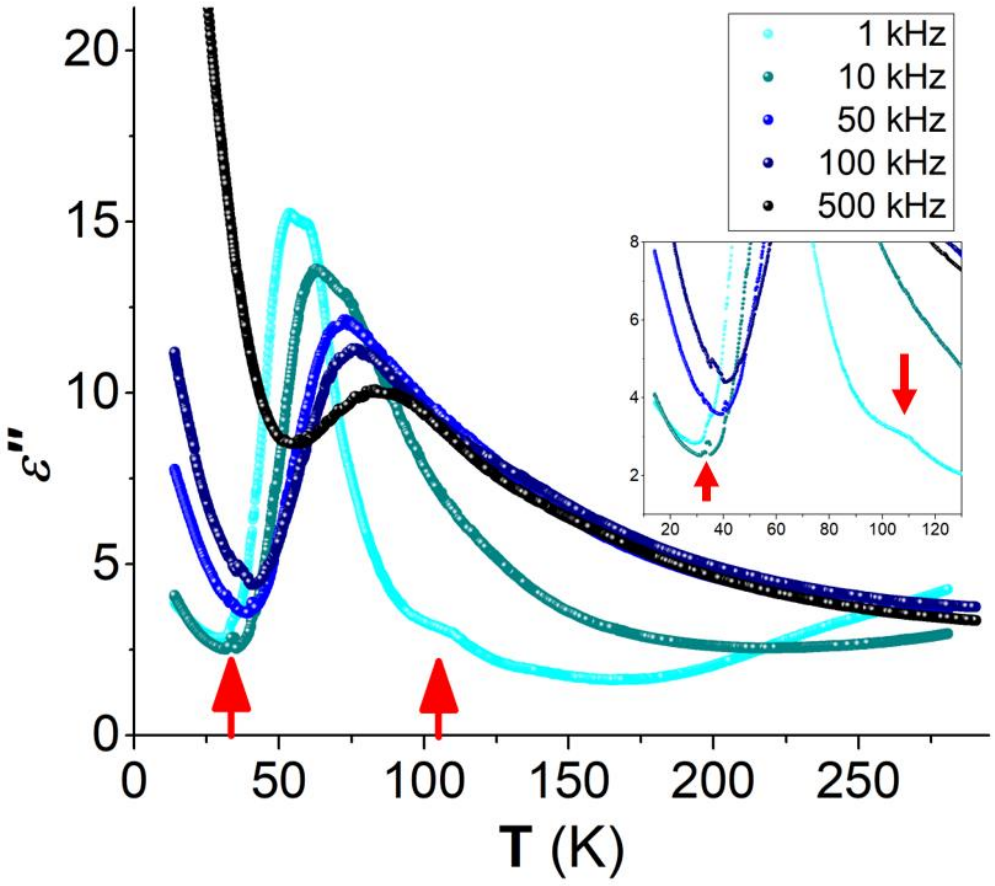

Figure 46: Temperature dependence of the imaginary part of the complex electric permittivity of the GMO-1 film, measured at different fixed frequencies. Red arrows point to anomalies of ε''(T). Inset is a detail of the low temperature anomalies.

The ε''(T) curve measured at 1 kHz exhibits a small anomaly at 105 K, which is ascribed to the antiferrodistortive phase transition of the STO substrate, as it is usually observed when this material is used as substrate. Due to the relatively small amplitude of this anomaly and the fact that it is only observed at a single frequency along with the different temperature dependence of the measured dielectric constant, regarding the actual dielectric response of STO, we realize that the contribution of the STO to the overall dielectric response is negligible small. A closer look at the ε''(T) curve measured at 10

kHz reveals a small but clear anomaly at $T_1 \approx 35$ K, which is also observed in other frequencies at the same temperature.

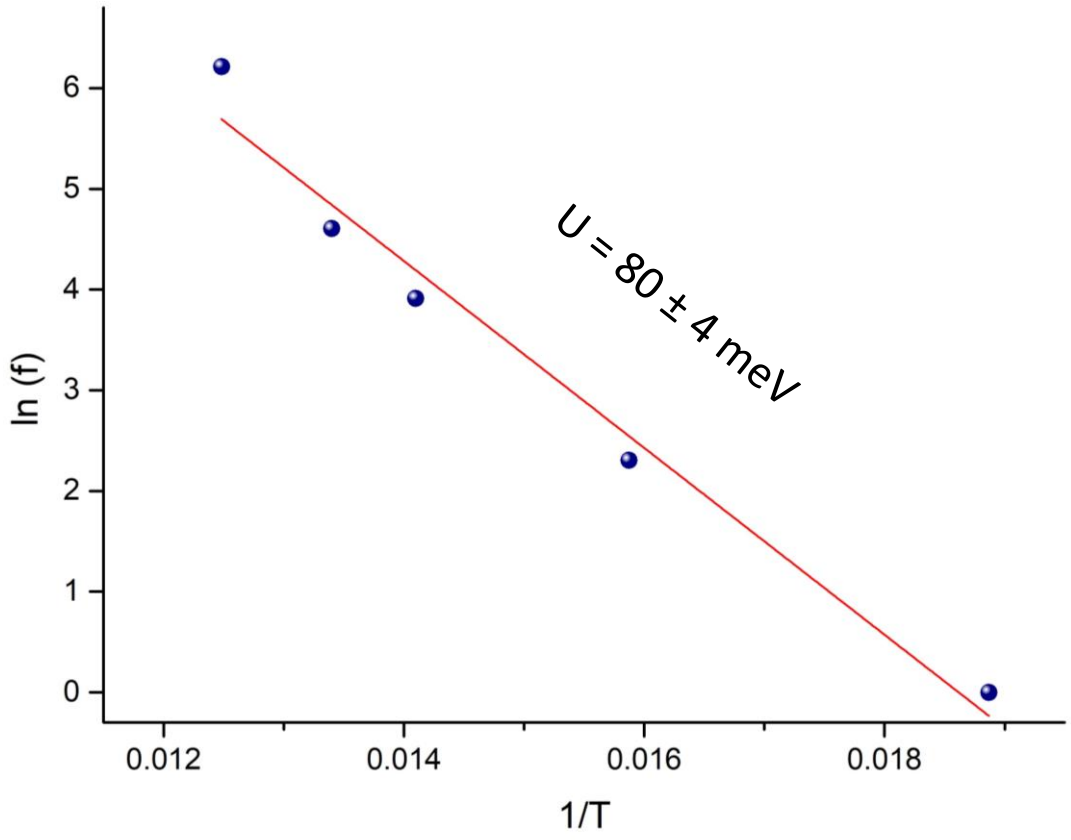

Figure 47: Arrhenius plot for the relaxation process with respective activation energy of the GMO-1 film.

3.1.4. Thermally stimulated depolarizing currents

In order to disentangle the underlying processes that can be associated with the emergence of the anomaly observed at $T_1 \approx 35$ K, we have studied the polar properties of the GMO-1 film. For this purpose, we have measured the thermally stimulated depolarizing current (TSDC) in two distinct poling conditions: the sample was cooled i) in the absence of an electric field, and ii) under different bias electric fields: 1.0, 2.5, and 5.0 kV/m. The TSDC was measured in the absence of an applied electric field in heating runs, at fixed temperature rate of 8 K/min. The results are displayed in Figure 48. The preparation of samples and the implementation of the measurement technique are detailed in Chapter 2, section 2.6.1.3.

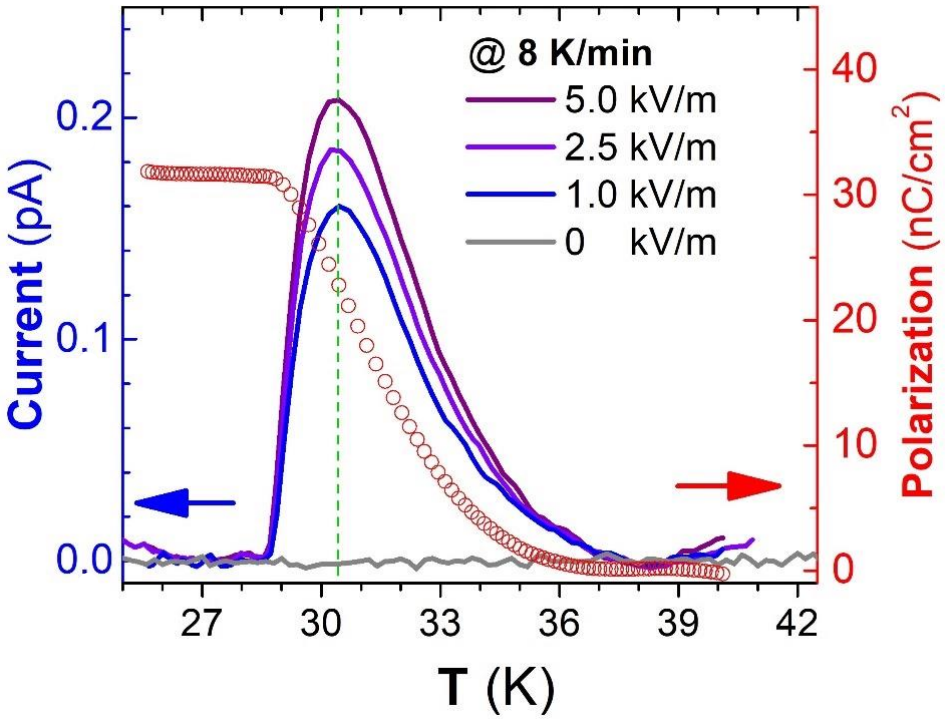

Figure 48: Left axis: TSDC as a function of temperature, after cooling the sample, with different polling electric fields. Right axis: the respective estimated polarization, obtained from time integration of the highest TSDC density. Green Dashed line represents the temperature at which the maximum current occurs for each polling electric field.

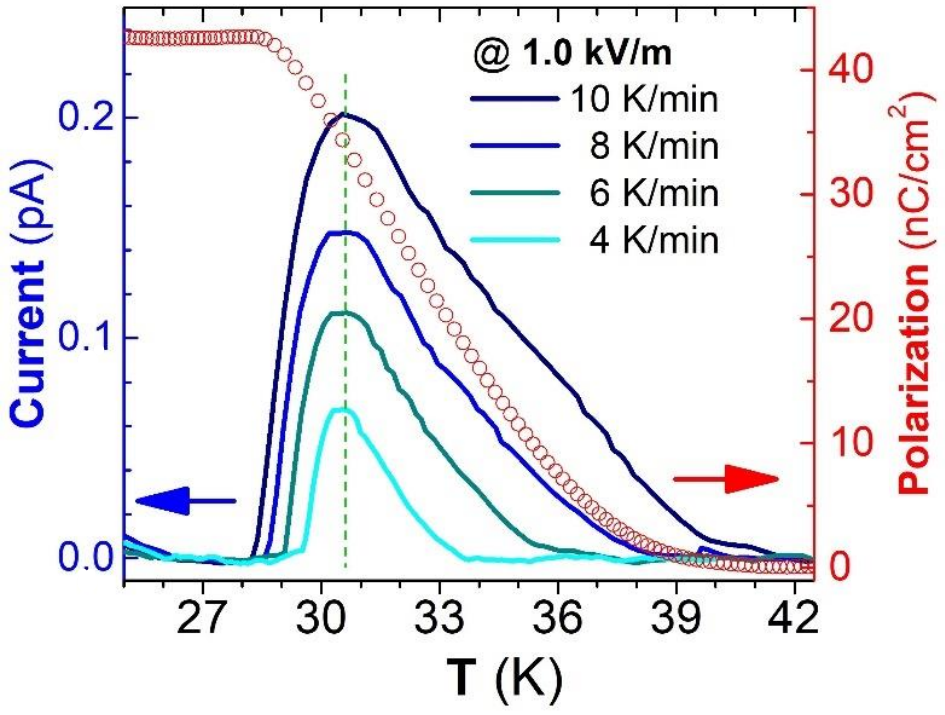

Figure 49: Left axis: TSDC as a function of temperature, after cooling the sample, measure with different heating rates. Right axis: the respective estimated polarization, obtained from time integration of the highest TSDC density. Green Dashed line represents the temperature at which the maximum current occurs for each heating rates.

In the absence of a polling electric field, no anomaly in the temperature dependence of the TSDC could be observed. An anomaly in the temperature dependence of the TSDC is apparent at 31 K, in experiments for which the sample was cooled down under the poling field, while experiments using inverse poling fields result in the respective reversed TSDC signal (see Figure 50). Moreover, the temperature for which the anomaly in the temperature dependence of the TSDC is ascertained does not depend on the strength of the poling electric field. However, as it is expected, the amplitude of the anomaly increases by increasing the poling electric field.

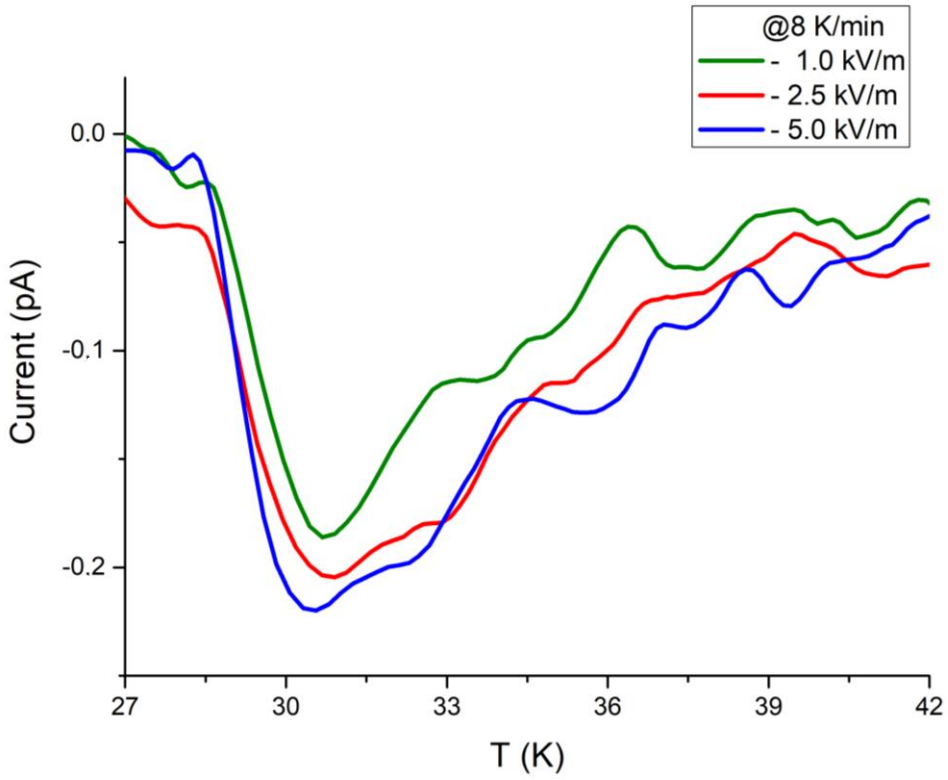

Figure 50: TSDC as a function of temperature, after cooling the sample with different inverse polling electric fields.

The heating rate dependence of TSDC was also studied after poling the film with a 1.0 kV/m electric field under different temperature rate: 4; 6; 8; and 10 K/min, in order to determine its actual origin. Figure 49 shows the experimental result of the temperature dependence of the TSDC. The amplitude of TSDC anomaly increases and becomes broader with increasing heating rate, possibly due to thermal inertia effects of the measuring system, but the peaks maxima, signaled by the vertical green dotted line, remains at 31 K, independently of the heating rate. This outcome reflects the spontaneous origin of the TSDC associated with the stabilization of a ferroelectric phase,

and excludes others charge displacement origins, as those observed in electrets and related compounds, wherein the driving force is the restoration of charge neutrality through disorientation of electric dipoles, and diffusion of immobilized space charges, among others [105]. This result clearly evidences for the ferroelectric nature of the $GdMnO_3$ thin film on (001) oriented STO substrate, between 10 K – 31 K. It is worth to stress that the critical temperature of the para-ferroelectric phase transition in the $GdMnO_3$ thin film is about 8 K higher relatively to $GdMnO_3$ bulk [58].

In order to determine the temperature dependence of the in-plane component of the electric polarization associated with the ferroelectric phase, we have carried out the time integration of the pyroelectric current shown in Figure 49 that was measured at the lowest electric poling field, in order to avoid induced contributions expected from applying higher poling fields. In this case, the in-plane component of the electric polarization value around 40 $nC.cm^{-2}$ is obtained below 31 K, of similar order of the saturation values found in bulk $TbMnO_3$ and $DyMnO_3$ below 20 K [109]. K. Shimamoto *et al.* have reported the emergence of an electric polarization of ~1 $\mu C.cm^{-2}$ along the *a*-axis in 10 nm thick orthorhombic $GdMnO_3$ thin films onto (010)-$YAlO_3$ substrates [46]. This value contrasts with the one here reported in the tetragonal $GdMnO_3$ films, which can be explained by the different nature of the ferroelectric phase in orthorhombic and tetragonal $GdMnO_3$ films, ascertained by the different temperature dependences of the electric permittivity. Actually, the temperature dependence of the real part of the electric permittivity of orthorhombic $GdMnO_3$ film onto (010)-$YAlO_3$ substrate exhibits a cusp-like anomaly and no relaxational process is ascertained [46]. Contrarily, in our case, a completely different result is obtained, evidencing the improper nature of the ferroelectric phase in the tetragonal film. Moreover, the difference between the values can also stem from the fact that we are only measuring the in-plane component of the electric polarization.

3.1.5. Magnetic measurements

The magnetic measurements were performed as described in detail in Chapter 2, section 2.6.2 wherein the external magnetic field was applied parallel to the plane of the film. The magnetic response of the $SrTiO_3$ (001) substrate, measured in field cooling conditions, is shown in Figure 51. The M(T) values are one of magnitude higher (~ 6 x 10^{-5} emu/g) than the experimental sensibility of the SQUID facility (1x10^{-7} emu), and small variations could be ascertained below 150 K. The temperature dependence of the magnetization of the GMO-1 film, measured under field cooling conditions, and obtained by subtracting the STO contribution, is shown in Figure 52. The order of magnitude of

the in-plane component M(T) is about 4 orders of magnitude higher than the magnitude of the clean substrate. M(T) monotonous increases as temperature lower from 300 K. Several small anomalies can be observed in M(T) at 133 K, 99 K and 53 K. The amplitude of the magnetization kinks occurring at these temperatures is larger than 10^{-4} emu/g, which excludes any contribution arising from the substrate. The later one occurs about 10 K above the value of T_N found for bulk material (T_N ~ 42 K).

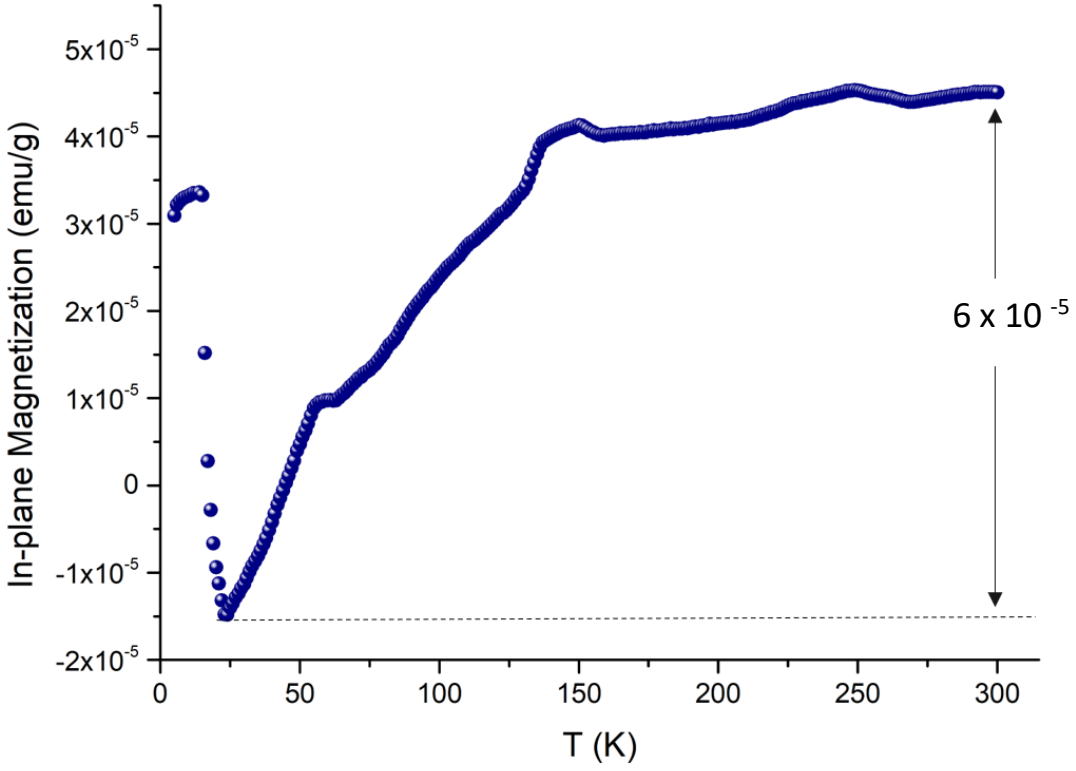

Figure 51: Temperature dependence of the magnetization of the substrate STO measured in field cooling conditions under an applying static field of 100 Oe.

The quality of the results hinders us to make more reliable claims about the magnetic response of the GMO-1 film and the nature of the remaining two anomalies deserves further studies.

In contrast, the continuous measuring of M(T) as T decreases down to 4 K, point for a weak ferromagnetic response in GMO-1 film. This interpretation needs further studies. However, if the weak ferromagnetic response is corroborated, this means that the magnetoelectric coupling in tetragonal $GdMnO_3$ has different nature than in orthorhombic material.

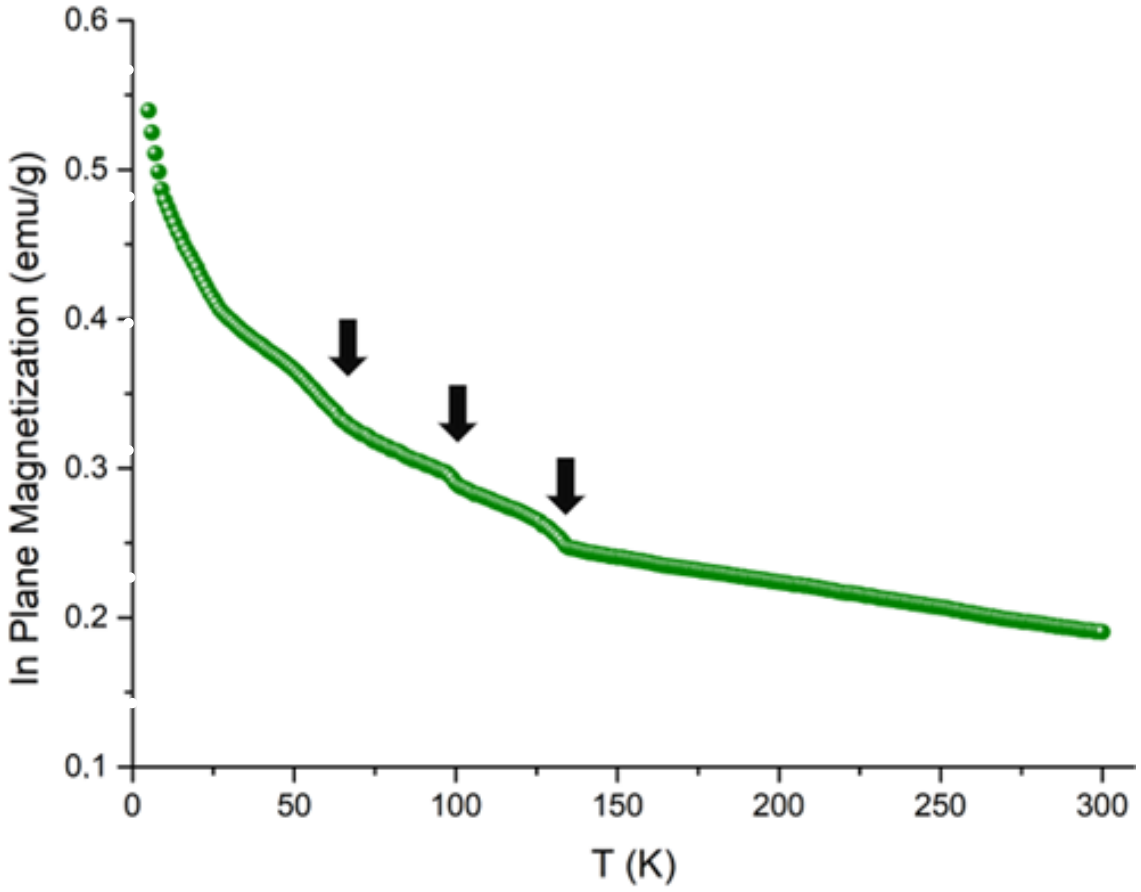

Figure 52: Temperature dependence of the magnetization of the GMO-1 film measured in field cooling conditions, applying static field of 100 Oe (contribution from STO was subtracted).

3.2. Thin Films of $GdMnO_3$ Deposited on (110)- $SrTiO_3$ Substrates

Summary: $GdMnO_3$ epitaxial thin films were also deposited onto (110)-oriented $SrTiO_3$ substrates by RF magnetron sputtering. The structure, microstructure, dielectric and magnetic properties were investigated in detail. The XRD results revealed that the $GdMnO_3$ thin films exhibit an epitaxial strained orthorhombic symmetry and grow preferably in off-plane (001) orientation, wherein the basal lattice parameters are strained by the substrate lattice. A dielectric relaxation process was ascertained, whose activation energy changes at specific temperatures, occurring at 41 K and at 20 K, respectively, which can be associated with magnetic phase transitions. The canted nature of the low temperature magnetic phase is discussed.

3.2.1. Morphology and chemical composition

Figure 53 shows a representative cross-section SEM image of the GMO-3 film. It exhibits a dense and uniform layer, with a good adhesion to the substrate, without structural defects or cracks, and average thickness of 44 ± 4 nm.

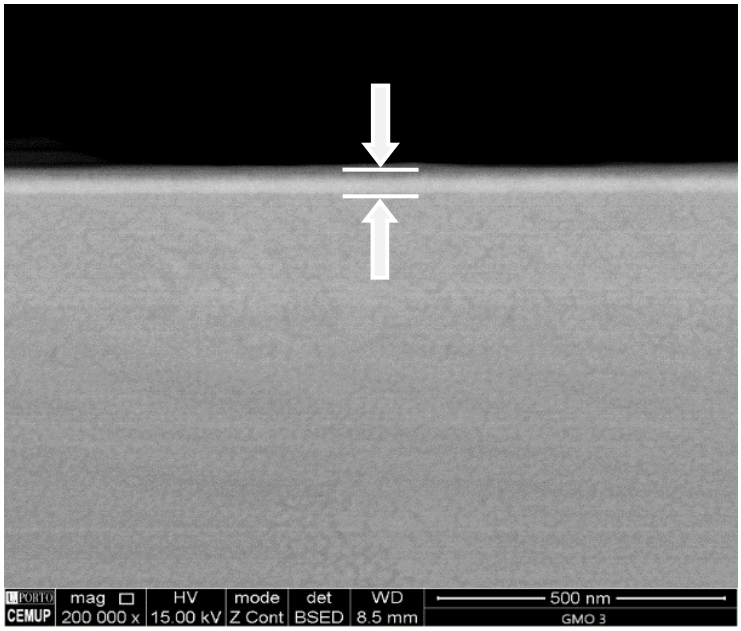

Figure 53: Representative SEM cross-section image of the GMO-3 film.

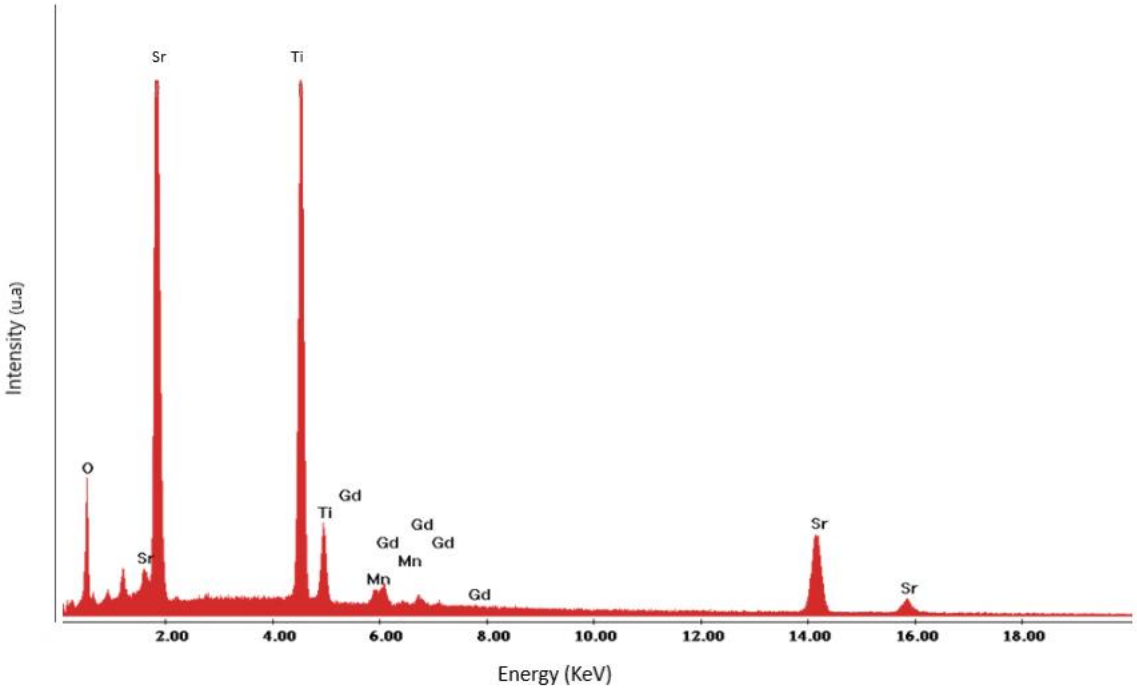

Figure 54: Energy dispersive X-ray spectroscopy spectrum of the elements present in the GMO-3 film.

Table 5: Table obtained by EDS with the elements presented in the GMO-3 film.

Element	Wt %	At %	K-Ratio
O K	62.7	92.4	0.268
Mn K	7.2	3.2	0.062
Gd L	30.1	4.4	0.252
Total	100.0	100.0	

The Figure 54 shows the energy dispersive X-ray spectroscopy (EDS) measurements of the GMO-3 film and confirms the presence of the elements Gd and Mn with a ratio of ~ 1.37, conditional to the incident electrons accelerating voltage (15-30 kV). Hence Gd:Mn ratio can be estimated close to 1.5, within a 20% error margin for both Gd and Mn atomic ratio. This error margin amount is expected due to the hindering diffraction effects of the film reduced thickness and interface with substrate [106]. In addition to the peaks referring to the elements of the film (Gadolinium (Gd), Manganese (Mn) and Oxygen (O)), other peaks referring to the elements of the substrate were also detected, namely strontium (Sr), Titanium (Ti) and Oxygen (O), where oxygen accounts for all the elements present in the two materials.

According to these results, the obtained films have the desired chemical stoichiometry $GdMnO_3$, with uniform and homogeneous layer, ensuring both the chemical and morphological quality of the GMO-3 film.

3.2.2. Structural characterization

Figure 55 displays a representative X-ray Reflectometry diffractogram of the GMO-3 film, exhibiting low contrast fringes, from which the thickness of 44 ± 4 nm was estimated. The low contrast fringes corroborate the good adhesion of the film to the substrate, ascertained from the SEM images. Figure 56 shows the conventional X-ray diffraction pattern (red line) of a GMO-3 film. The main STO reflections are observed at $2\Theta = 32.14°$ and $2\Theta = 67.56°$, indexed to the (110) and (220) planes, respectively. This result confirms the orientation (110)-STO of the substrate, ascribing a_{STO} = 3.905(0) Å, in good agreement to referenced data [65].

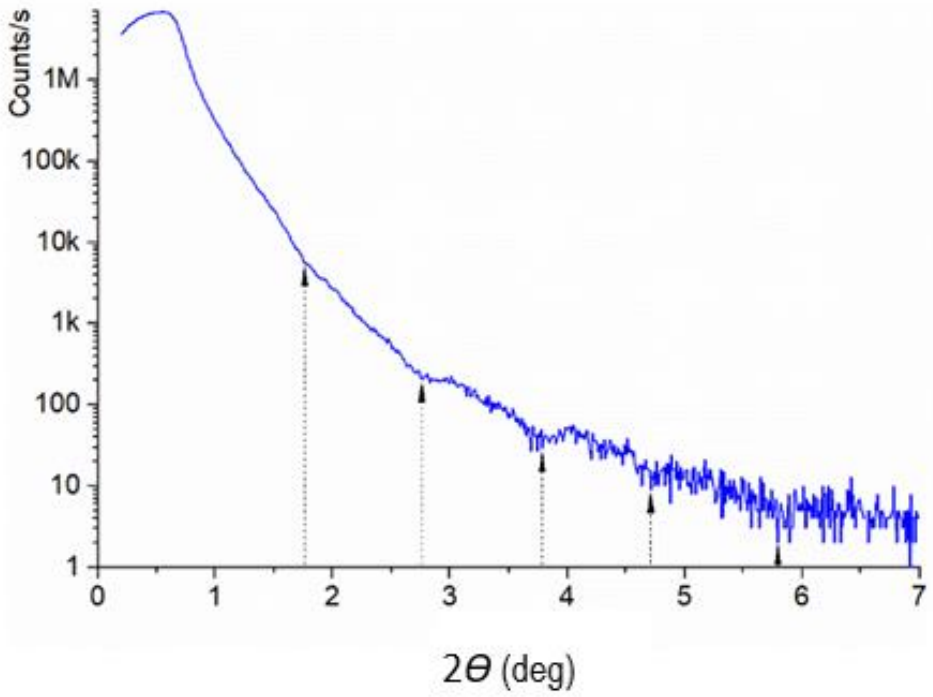

Figure 55: XRR diffractograms of the GMO-3 (44 nm) thin film with respective fringes signalled by arrows.

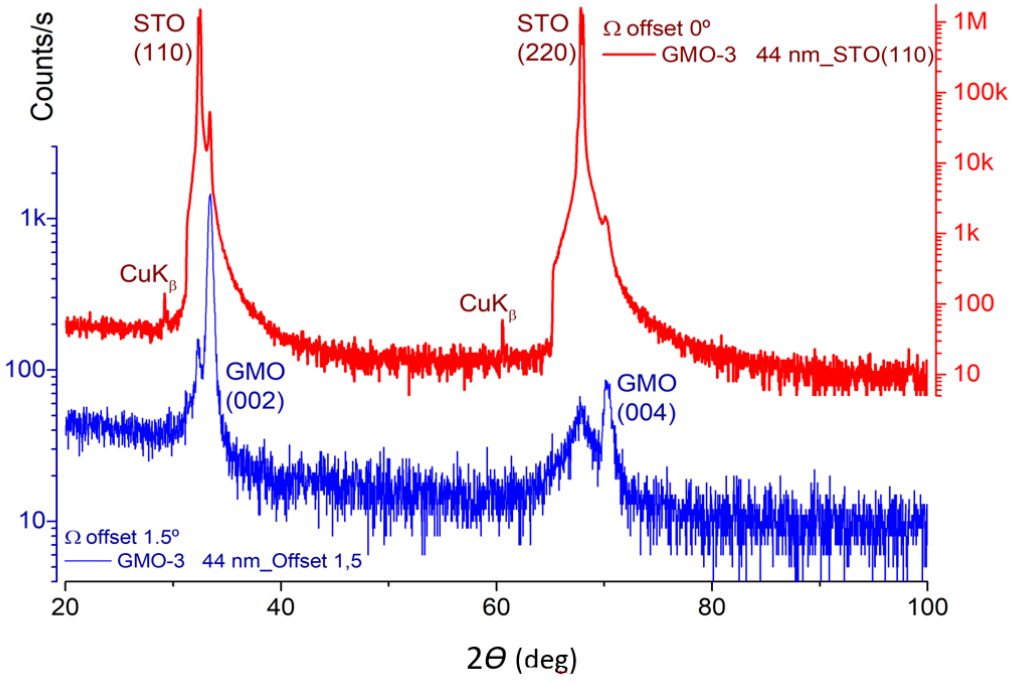

Figure 56: Details of the conventional (gonio) XRD patterns of the GMO-3 film (red line) and using a $\Delta\Omega = 1.5°$ offset (blue line).

No evidence of spurious GdO_x or MnO_x phases could be found in the detection limit of the technique, corroborating the stoichiometry and phase purity of the film. By adjusting the XRD acquisition parameters with a $\Delta\Omega$ = 1.5° offset (blue line in Figure 56), it allows to focus on the $GdMnO_3$ film layer and surpass substrate reflections. The main peaks at 2Θ = 33.43° and 70.24° are indexed, respectively, to the (002) and (004) planes of the $GdMnO_3$ phase, evidencing the preferential off-plane growth of $GdMnO_3$ oriented along the *c*-axis. In addition, it is possible to perceive a slight Bragg peak at 2Θ = 31.25°, indexed to the reflection from the (200) planes. This evidences that the film does not grow uniformly and two different $GdMnO_3$ layers (hereafter called α- and γ- layers) are present.

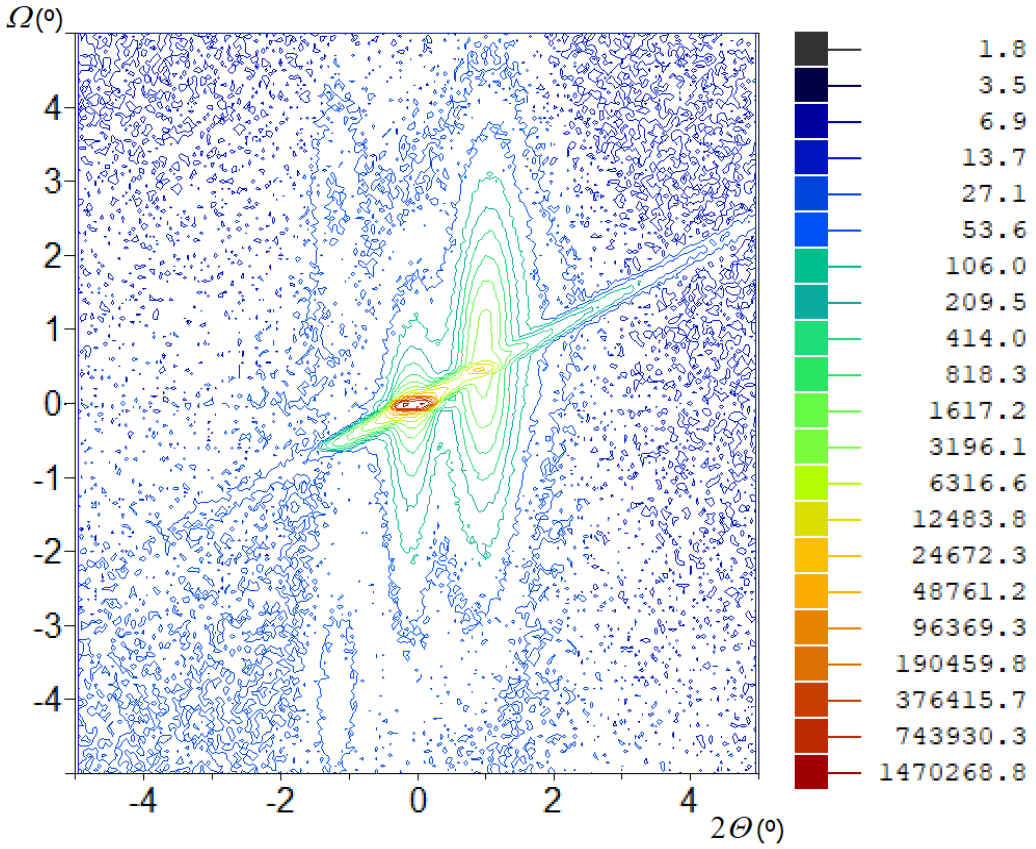

Figure 57: Symmetric reciprocal space map (Θ-Ω) over substrate reflection (110)-STO at 2Θ = 32.43° and Ω = 16.22°.

Figure 57 shows the symmetric XRD space map in the Θ-Ω coordinates, relatively to the (110)-STO reflection peak, centered at 2Θ = 32.43° and Ω = 16.22°. This map evidences the presence of 3 reflection peaks emerging from the $GdMnO_3$ thin film. The main peak found at 2Θ = 33.35° ($\Delta(2\Theta)$ = ±0.1), with Ω = 16.72° ($\Delta(2\Omega)$ = ± 0.1), shadows the shape of the (110)-STO peak, and shows a long relaxation tail visible up to 2Θ = 37°, which can

be associated with Laue interference fringes, typically found in a layered topology. This peak is consistent with the Bragg reflection on the GMO (002)-planes, confirming the off-plane growth direction along the c_γ-axis, and yielding a lattice parameter c_γ = 5.372(4) Å assigned to the γ-layer. Two additional satellite peaks are observed at 2Θ = 31.24°, extending orthogonally to each side of (110)-STO peak at Ω = 18.87° and Ω =12.25°, respectively. These peaks are indexed to GMO (200)-plane reflections. Although relatively faint, these two peaks are well-defined (Δ2Θ ≈ ±0.5°, ΔΩ ≈ ±0.5°), thus confirming the presence of a twined crystalline growth along a_α-axis in the off-plane direction, with a calculated lattice parameter a_α = 5.72(2) Å of the α-layer. The low ratio between the I_α/I_γ peaks intensity suggests the α-layer is only a few nanometres thick. The asymmetric space map over the reflection on GMO (114) planes, displayed in Figure 58, shows a regular single peak positioned at 2Θ = 73.69°, which does not point to any twinning effects, in good agreement with the rather small thickness of α-layer.

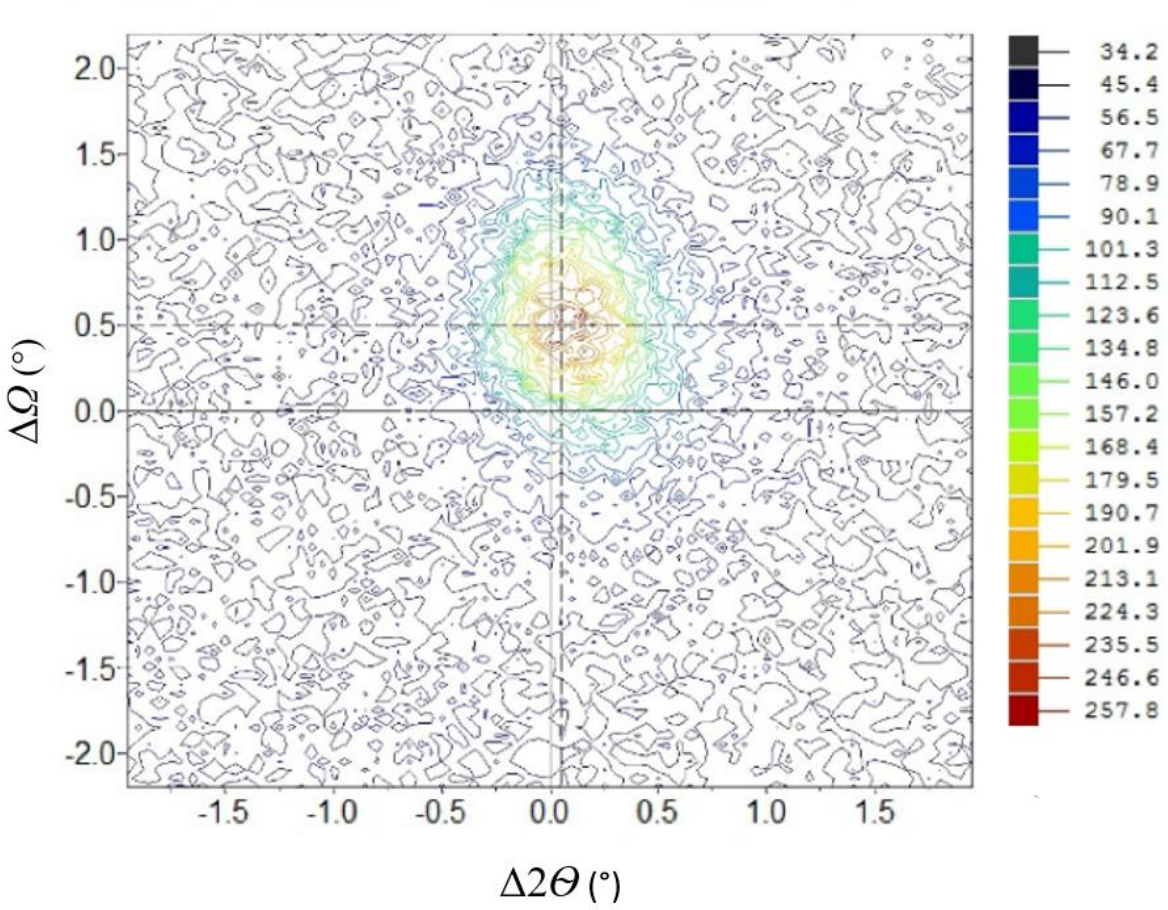

Figure 58: Asymmetric space map over the reflection GMO (114) at 2Θ = 73.69°, Ω = 19.78°, Φ = 38.64° and Ψ =-0.38°.

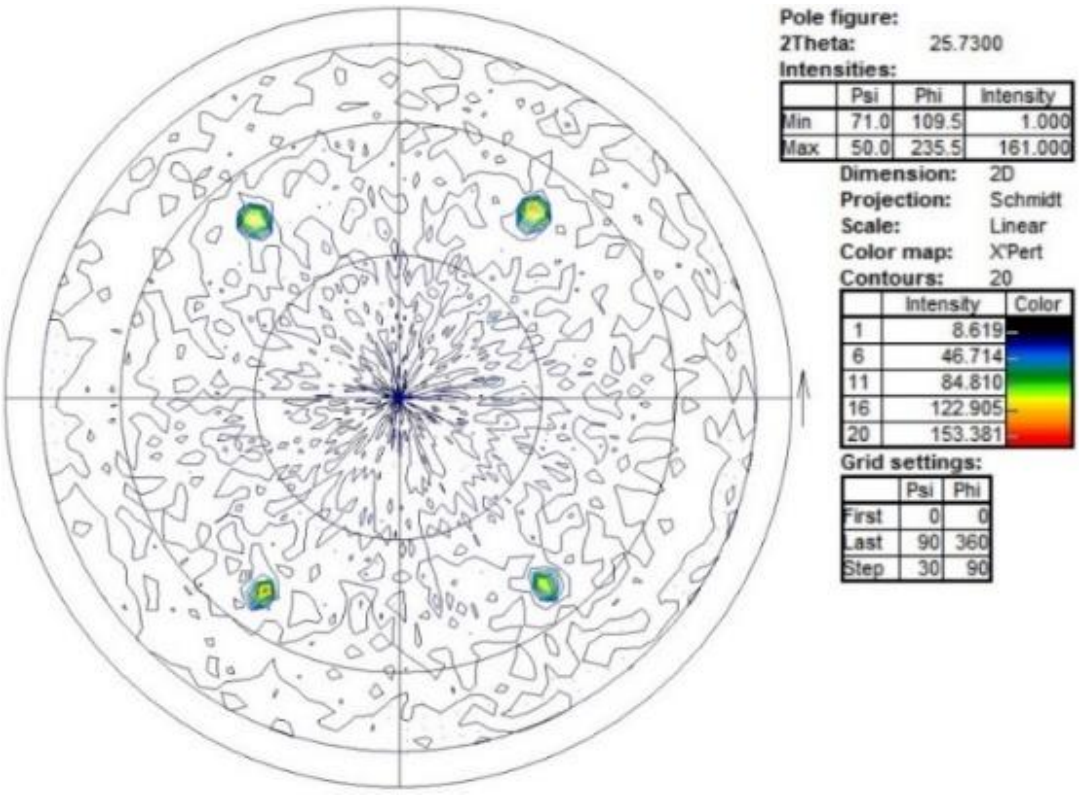

Figure 59: Symmetric pole figure encompassing thin film (111) central reflection at 2Θ = 25.73°.

Figure 59 shows the symmetric pole figure obtained at 2Θ = 25.73° corresponding to the reflection from the (111) planes of the $GdMnO_3$ film. The observation of 4 reflections near Ψ ≈ 50.0° ± 0.1°, positioned at Φ = 55.2°, 128.2°, 235.5° and 307.6°, confirms the orthorhombic symmetry of the $GdMnO_3$ phase, and is compatible with the dominant off-plane preferential growth orientation of the film along the c_γ-axis, from the γ-layer, with the a_γ- and b_γ-axes lying in-plane. The average projected angle ΔΦ = 36.3°± 0.2° corresponds to the relation $a_\gamma/b_\gamma = 0.734(0)$.

Figure 60 shows a schematic of the relative orientation of the $GdMnO_3$ unit cell to the (110)-STO substrate, to visualize the crystallographic relations between the main phase of the $GdMnO_3$ thin film and the (110)-STO substrate. According to the projected angles from the pole figure, the *a*-axis trails the substrate cell face diagonal and *b*-axis follows the cell face side.

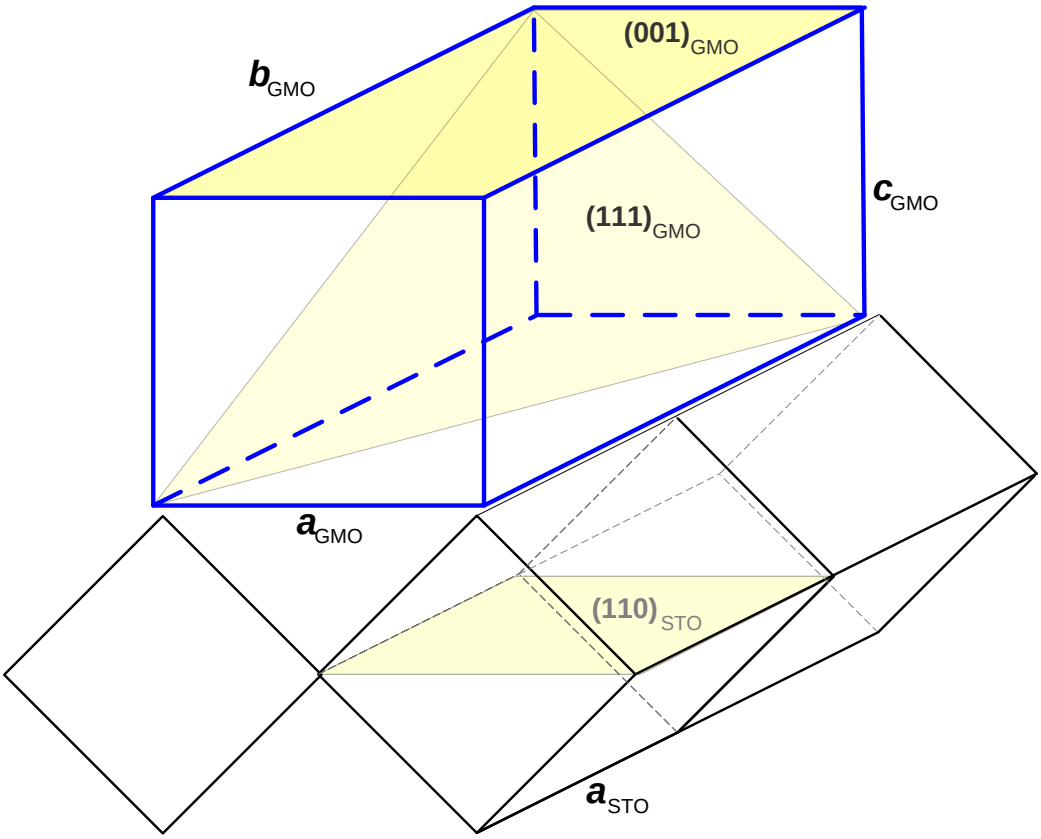

Figure 60: Diagram representing the crystallographic relations between the $GdMnO_3$ film main phase and the (110)-STO substrate.

The lattice parameters of the γ-phase GMO-3 film (a_γ, b_γ and c_γ), calculated from the XRD patterns, and the respective relative distortions to the STO substrate and bulk $GdMnO_3$ (a_0, b_0 *and* c_0) are shown in Table 6. The γ-phase GMO-3 film a_γ lattice parameter expands 1.4% relatively to the primitive cell diagonal of the STO substrate and contracts 4.4% relatively to the corresponding value in bulk $GdMnO_3$, while the b_γ lattice parameter behaves in opposite way: it contracts 2.3% relatively to the double STO lattice parameter and expands 2.8% relatively to the corresponding value in bulk $GdMnO_3$. The γ-phase GMO-3 film c_γ lattice parameter also contracts 2.9% relatively to the primitive cell diagonal of the STO substrate and expands 1% relatively to the corresponding value in bulk $GdMnO_3$. This result evidences for opposite strain behaviour of the in-plane a_γ and c_γ GMO-3 film.

Table 6: Lattice parameters and relative variations of GMO-3 thin film to STO substrate and bulk GMO [109].

STO Substrate (Å)	$\Delta_{\gamma/STO}$ (%)	GMO-3 Oγ-layer	$\Delta_{\gamma/GMO}$ (%)	GMO O-bulk [109]
$\sqrt{2}.a_{STO}$ 5.530	+ 1.4	a_γ (Å) 5.60(8)	- 4.4	a_o (Å) 5.866
2 x a_{STO} 7.820	- 2.3	b_γ (Å) 7.64(1)	+ 2.8	b_o (Å) 7.431
$\sqrt{2}.a_{STO}$ 5.530	- 2.9	c_γ (Å) 5.37(2)	+ 1.0	c_o (Å) 5.318
		V_γ (Å^3) 230.1(8)	- 0.7	V_o (Å^3) 231.81

Since γ-layer volume has a less pronounced variation of -0.7 % from the bulk GMO, it suggests that α-layer grows on the STO substrate and acts as buffer for γ-layer. Due to the reduced presence of α-layer, it was not possible to obtain the values of the in-plane b_α and c_α directly. Nonetheless, α-layer(orto) is highly constrained by epitaxial relations to either the substrate (110)-STO and the GMO γ-layer, corresponding to: $\sqrt{2}a_{STO} > c_\alpha \approx c_\gamma > c_0$, and to $2a_{STO} > b_\alpha \approx b_\gamma > b_o$, which forcibly leads to an expansion of the lattice volume relative to the bulk GMO, estimated between +1.3 % minimum and +6.8 % maximum.

3.2.3. Complex dielectric permittivity

Figure 61 and Figure 62 show the temperature dependence of the real (ε') and imaginary (ε'') parts of the complex electric permittivity, respectively, of the GMO-3 film, measured at different fixed frequencies, from 10 to 300 K, in a heating run. As temperature decreases, for frequencies above 100 kHz, the ε'(T) curves increase and reach a maximum at a frequency dependent temperature, while for frequencies below to 100 kHz this maximum is not reached down to 10 K. The ε''(T) curves monotonously increase as temperature decreases, with a strongly frequency dependent slope. These frequency

dependent features are clear evidence for a relaxation process that hinders the direct observation of anomalies associated with phase transitions.

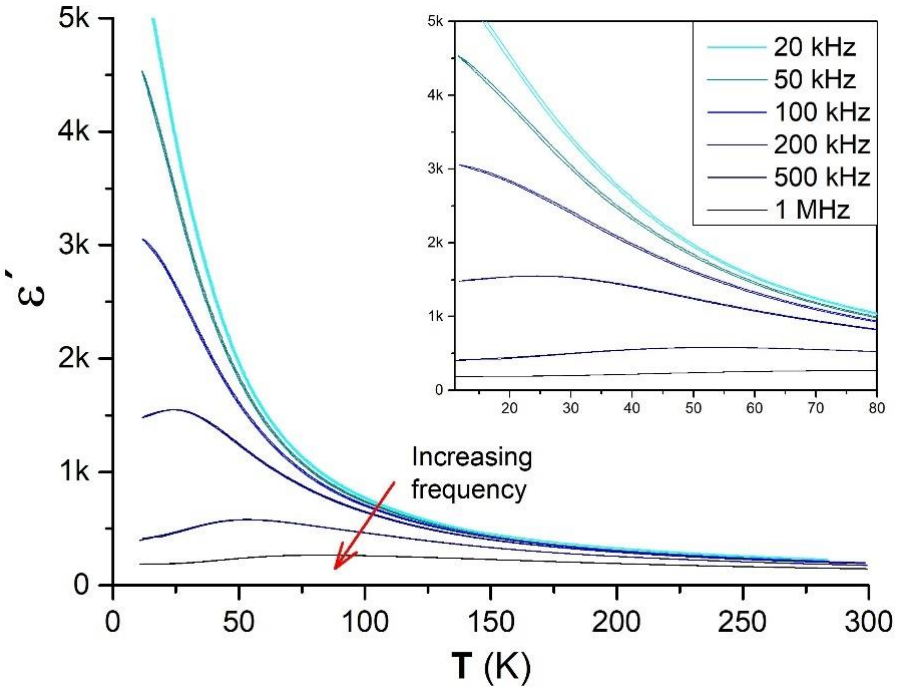

Figure 61: Real part of complex dielectric permittivity measured in plane as a function of temperature for different fixed frequencies of the GMO-3 film. The inset is a detail of the low temperature anomaly.

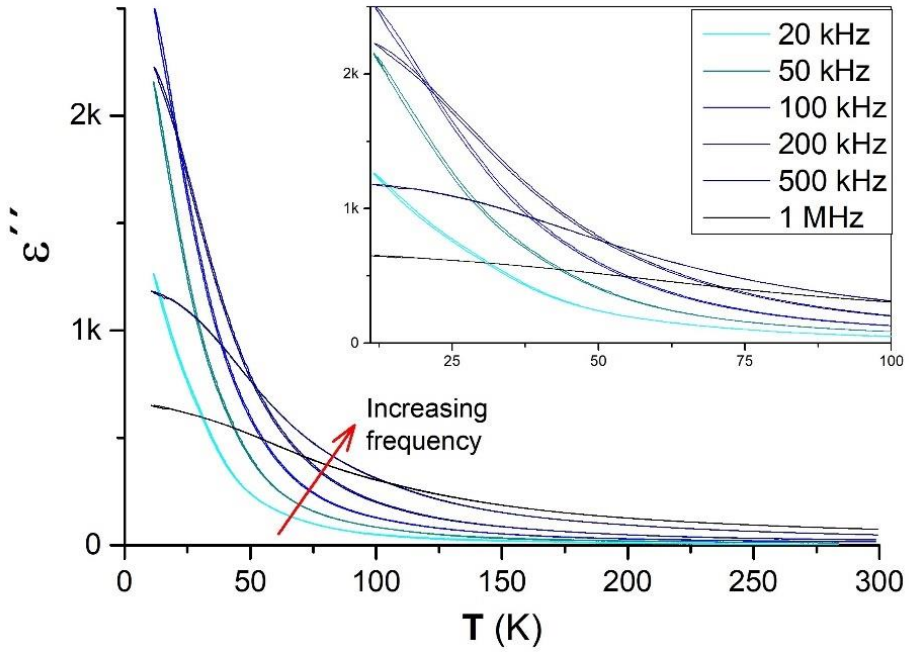

Figure 62: Imaginary part of complex dielectric permittivity measured in plane as a function of temperature for different fixed frequencies of the GMO-3 film. The inset is a detail of the anomaly.

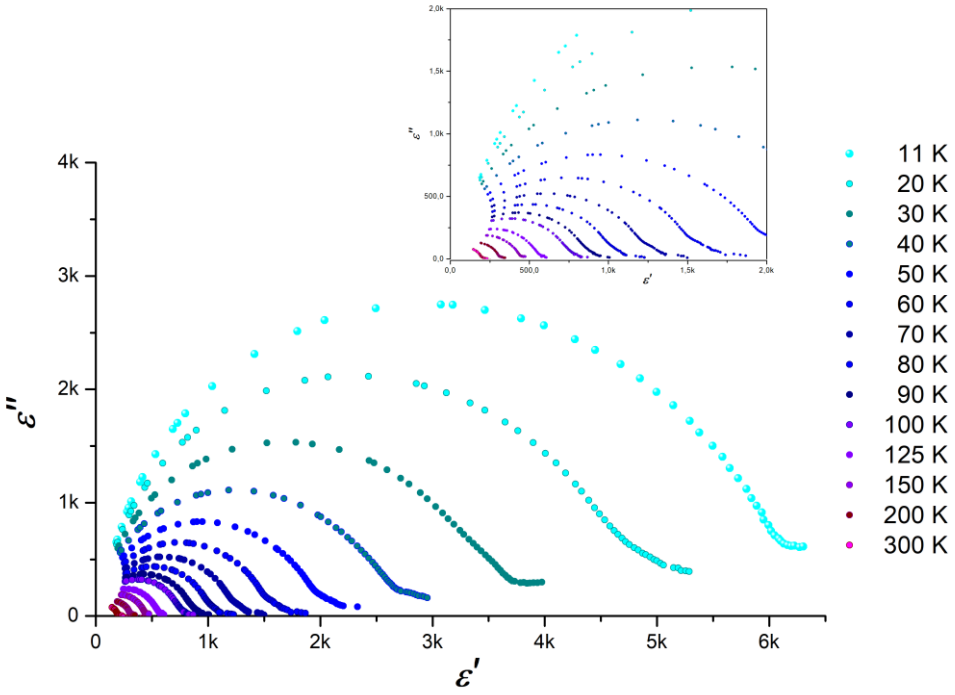

Figure 63: Cole-Cole plots at different fixed temperatures of the GMO-3 film. The inset is a detail of the anomaly.

However, more information regarding the low temperature critical phenomena can be achieved from the study of the dielectric relaxation. Figure 63 shows the Cole-Cole plots at different temperatures, which follow well defined semicircles, with decreasing radius for increasing temperatures. In this work, the relaxation frequency was taken at the maximum of each semicircle, to obtain the Arrhenius plot, shown in Figure 64. The activation energy (E_a) can be obtained by the Arrhenius equation:

$$f = f_o \, e^{\frac{-E_a}{k_B T}} \tag{3.1}$$

where $f(T)$ is the temperature dependent relaxation frequency, f_o is a pre-exponential factor, E_a the activation energy, k_B is the Boltzmann constant, and T is the temperature. The activation energy can be determined graphically by manipulating the Arrhenius equation to put it into the form of a straight line, applying the natural logarithm of both sides:

$$\ln(f) = \frac{-E_a}{k_B}\left(\frac{1}{T}\right) + \ln f_o \tag{3.2}$$

a slight rearrangement of this equation gives us a straight line plot ($y = mx + b$) for ln (f) versus 1/T, where the slope is $-E_a/k_B$.

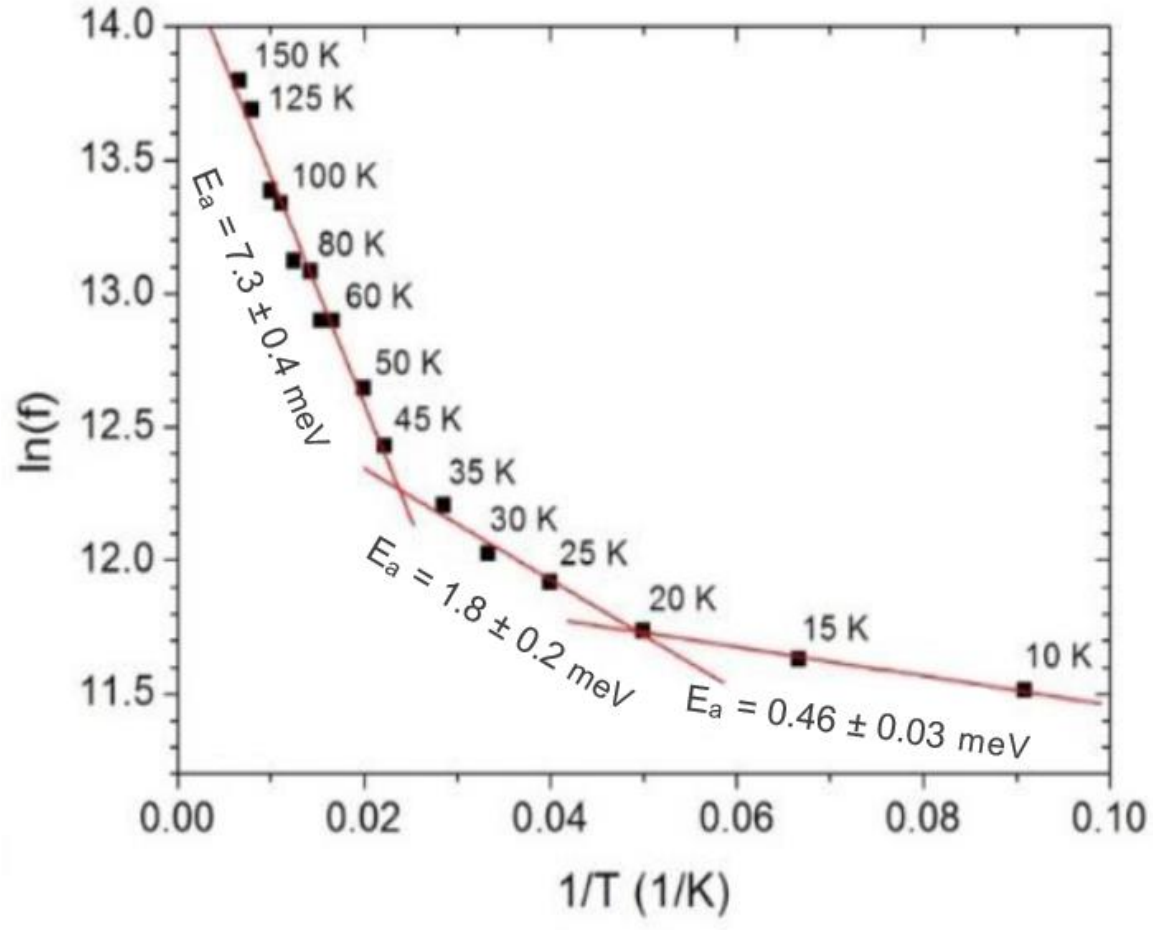

Figure 64: Arrhenius plot for the relaxation process with respective activation energies of the GMO-3 film.

As it can be ascertained from Figure 64, the data cannot be described by a single linear regime for the whole studied temperature range. Two changes of slope occur, one between 35 K and 45 K, and another at around 20 K, associated with changes of the relaxation process which mirror in the activation energy. Above 45 K the activation energy is 7.3 ± 0.4 meV, while between 35-45 K and 20 K it reduces to 1.8 ± 0.2 meV, and below 20 K it further drops to 0.46 ± 0.03 meV. Similar changes of the activation energy were also observed in bulk $GdMnO_3$, though from values of 10 to 20 meV, having been correlated with the magnetic phase transitions [111]. The result here presented points out for the existence of two phases transitions, one between 35 and 45 K, and another around 20 K. These temperatures are close to the two critical temperatures found in bulk $GdMnO_3$. In order to shed light to this assertion, we have studied the magnetization of the film as a function of temperature.

3.2.4. Magnetic measurements

Figure 65 shows the temperature dependence of the magnetization of the GMO-3 film, measured in ZFC and FC conditions, under a 40 Oe magnetic field. The M(T) curve measured in ZFC conditions exhibits a peak-like anomaly at 20 K, at the same temperature where the change in the activation energy of the relaxation process is observed. The value of the M(T) increases significantly in FC conditions just below 25 K. If bulk $GdMnO_3$ magnetic properties are considered, this result evidences for the stabilization of a weak-ferromagnetic component, arising from a canted AFM phase below T_C = 20 K, which is responsible for the large increase of the separation between the ZFC and FC curves below this temperature.

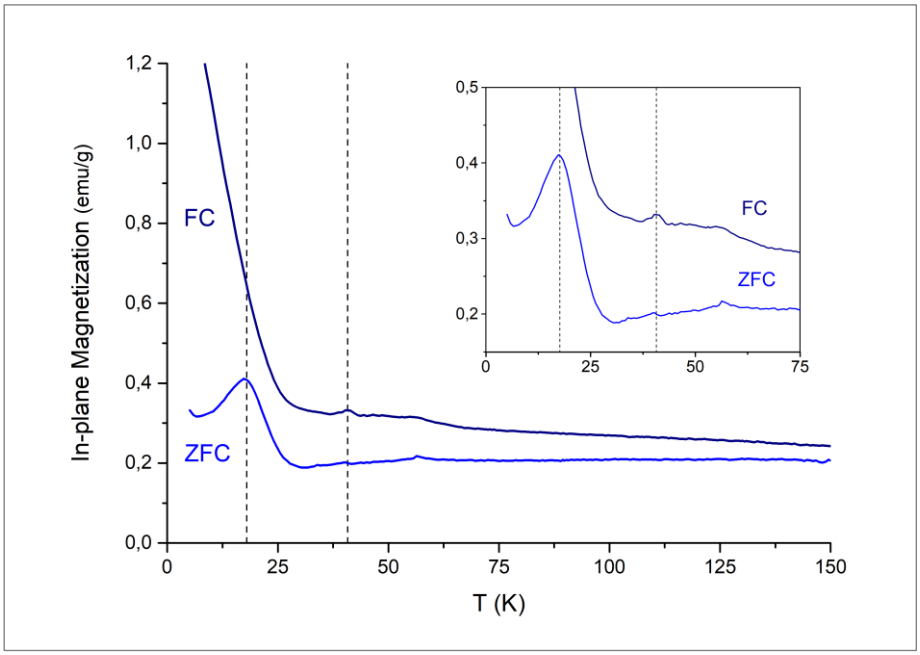

Figure 65: In-plane magnetic response of the GMO-3 film as a function of temperature, measured in ZFC and FC conditions under an applied field of 40 Oe. Vertical dashes lines mark phase transitions. The inset is a detail of the anomalies.

A faint but clear anomaly in M(T) measured in both ZFC and FC conditions is observed at 41 K, within the temperature interval of the second change in the activation energy. Although our data does not allow to unravel the nature of this anomaly, the stabilization of another magnetic phase cannot be excluded. Again, if bulk $GdMnO_3$ magnetic properties are considered, this anomaly is likely associated with the transition from the high temperature paramagnetic to the ordered magnetic phase, with an incommensurate spin modulation. Although further experimental evidences are still required, these results show that the GMO-3 film discloses a similar magnetic phase sequence as the bulk $GdMnO_3$.

Other anomalies in the M(T) curves can also be seen at 55 K. However, we do not assign them to any magnetic phase transitions for two reasons: i) the relaxation process activation energy does not change at this temperature; and ii) it has been reported that spurious oxygen found inside the SQUID magnetometer can be at the origin of such type of anomalies around 55 K [112].

Conclusion

The foremost purpose of this thesis is unquestionably to ascertain the definitive role of strain engineering in current technology as a route to provide improving functionalities or even rising new ones in brand new strong correlated systems. In the context of this thesis, strain-engineering comprises the control of the deformation withstood by a low dimensional system emerging from an oriented crystalline substrate induced stress, towards to meet specific requirements at the desired working conditions.

This approach has been widely and successfully used to tailor optical properties, to induce novel phases and specific polymorphous in well-known systems, as $SrTiO_3$, $BiFeO_3$ and $TbMnO_3$, at nano-scale level.

Though strain engineering can be used in a plethora of nano-scale strong correlated systems, this thesis is focused in applying this route to a most well-known oxide, the gadolinium manganite for the following main motives. On the first hand, $GdMnO_3$ is included in the family of rare-earth manganites, known by exhibiting relevant physical properties like colossal magnetoresistance, charge-orbital ordering, different magnetic structures and multiferroicity. On the second hand, they are strongly dependent on the Mn-O-Mn bond angle and thus on oxygen octahedra tilts. For the specific case of the orthorhombic rare-earth manganites, the magnitude of the Mn-O-Mn bond angle for $GdMnO_3$ falls at the border line between the value for $TbMnO_3$ and $DyMnO_3$, both well-known spontaneous multiferroics, and for $EuMnO_3$, which is a magnetic-field induced multiferroic. On the third hand, as the Mn-O-Mn bond angle mirrors the delicate balance between competitive electronic and magnetic interactions, these materials are highly sensitive to external parameters, which can distort their crystallographic structure, and eventually induce a change of lattice symmetry and concomitant oxygen octahedra tilts, thus customise their physical properties.

Though mechanical stress can be used to implement such distortions in $GdMnO_3$ bulk, significant higher distortions can be obtained in two dimensional $GdMnO_3$ films, up to a significant fraction of their ideal strength. These distortions can be achieved from handling the misfit between the lattice parameters and thermal expansion coefficients of the substrate and the $GdMnO_3$ film, as well as the one imposed by the substrate orientation surface.

The choice of the paramount substrate to grow a single phase epitaxial (non-relaxed) $GdMnO_3$ film is of crucial importance. Among the different available materials, oriented single crystalline $SrTiO_3$ substrates were chosen, since they are perovskite structured oxides, allowing a good interconnectivity between the substrate and the $GdMnO_3$ film, ensuring better epitaxy and control of octahedron rotation.

In order to accomplish the foremost purpose referred to above, this thesis aims to unravel the role played by strain-engineering in tuning the physical properties of $GdMnO_3$ thin films deposited onto single crystalline $SrTiO_3$ substrates that only differ in the symmetry of their surface: the (100) and (110) orientation. Both types of films withstand at room temperature a moderate tensile strain, which is a consequence of the relative values of bulk $SrTiO_3$ and $GdMnO_3$ pseudocubic lattice parameters.

By strictly following this work plan, we were able to demonstrate thoroughly the huge differences ascertained in $GdMnO_3$ films deposited on the same substrate but just with two different oriented surfaces. On one hand, the entirely odd crystallographic structure obtained: a tetragonal and an orthorhombic symmetry for the (100) and (110) oriented substrate, respectively. As it was referred to above, such different crystallographic distortions are concomitantly associated with specific Mn-O-Mn bond angle and oxygen octahedra tilt changes, and ultimately to noteworthy physical properties alterations.

One way to highlight these drastic changes is to focus on the temperature phase sequence of both $GdMnO_3$ films, ascertained by carrying out dielectric, TSDC and magnetic measurements.

Regarding the (100) $GdMnO_3$ film, the most proeminent result observed is the stabilization of an improper ferroelectric phase below to 31 K, which is not apparently observed in the bulk. In fact, the tetragonal symmetry must impose restrains in packing oxygen octahedra, and Mn-O-Mn orbitals overlap, and thus definite alterations in charge transfer. The reported contribution of a twin-like domain structure ascribed to a possible high temperature electric polarization in orthorhombic $GdMnO_3$ films is not applicable in this case, and thus the mechanisms associated with the stabilization of the ferroelectric phase in orthorhombic $GdMnO_3$ thin films needs still further attention.

In what the (110) $GdMnO_3$ film is concerned, a thoroughly different phase sequence is observed. Dielectric relaxation studies show that the activation energy changes at 41 K and 20 K that can be associated with magnetic changes. The latter is also clearly observed in the magnetic results and evidences for the stabilization of a canted AFM phase below to 20 K. The former is also detected in M(T) by a faint anomaly. Though,

the stabilization of another magnetic phase cannot be excluded, our data do not allow us to unravel its actual nature.

These outcomes evidence for the noteworthy effect of the epitaxial strain induced by substrate orientation on the structural distortions of $GdMnO_3$ thin films, and how strain mediated supplementary distortions influence the macroscopic properties. Thus, this work provides a guide to tailor the structure and the properties of strongly correlated oxides, through strain engineering, in order to unravel new and unexpected phases in perovskite thin films.

Open Questions and Future Work

To complement this work is exceedingly requested to produce high quality, single phase $GdMnO_3$ thin films deposited onto (111) - oriented $SrTiO_3$ substrates under similar experimental conditions. The structural, microstructural, dielectric and magnetic results systematic analysis will allow a far-reaching comparison with the results presented in this thesis for the $GdMnO_3$/(001)-STO and $GdMnO_3$/(110)-STO thin films. Furthermore, it will yield a most comprehensive understanding of the role of strain engineering in obtaining specific properties in strong correlated oxides.

References

[1] D. Shin *et al.*, “Quantum paraelectric phase of $SrTiO_3$ from first principles,” *Phys. Rev. B*, vol. 104, no. 060103, pp. 2–7, 2021.

[2] H. Liu, Y. Du, P. Gao, Y. Huang, Y. Ikuhara, and Y. Chu, “Tetragonal $BiFeO_3$ on yttria-stabilized zirconia,” *APL Mater.*, vol. 3, no. 116104, 2015.

[3] L. W. Martin, Y. H. Chu, and R. Ramesh, “Advances in the growth and characterization of magnetic, ferroelectric, and multiferroic oxide thin films,” *Mater. Sci. Eng. R Reports*, vol. 68, no. 4–6, pp. 89–133, 2010.

[4] A. Kumar, A. S. Verma, and S. R. Bhardwaj, “Prediction of Formability in Perovskite-Type Oxides,” *Open Appl. Phys. J.*, vol. 1, pp. 11–19, 2008.

[5] I. Loa *et al.*, “Pressure-induced quenching of the Jahn-Teller distortion and insulator-to-metal transition in LaMnO3,” *Phys. Rev. Lett.*, vol. 87, no. 12, pp. 125501/1-125501/4, 2001.

[6] D. Kan *et al.*, “Epitaxial strain effect in tetragonal $SrRuO_3$ thin films,” *J. Appl. Phys.*, vol. 113, no. 173912, pp. 0–7, 2013.

[7] G. Koster *et al.*, “Structure, physical properties, and applications of $SrRuO_3$ thin films,” *Rev. Mod. Phys.*, vol. 84, no. 1, pp. 253–298, 2012.

[8] J. Wei *et al.*, “Enhancement of Spin – Orbit Torque by Strain Engineering in $SrRuO_3$ Films,” *Adv. Funct. Mater.*, no. 2100380, pp. 1–7, 2021.

[9] W. Lu, W. Song, P. Yang, J. Ding, G. M. Chow, and J. Chen, “Strain Engineering of Octahedral Rotations and Physical Properties of $SrRuO_3$ Films,” *Sci. Rep.*, vol. 5, no. 10245, pp. 1–9, 2015.

[10] Y. Y. Pai, A. Tylan-Tyler, P. Irvin, and J. Levy, “Physics of $SrTiO_3$-based heterostructures and nanostructures: A review,” *Reports Prog. Phys.*, vol. 81, p. 036503 (53pp), 2018.

[11] S. A. Hayward, F. D. Morrison, and J. F. Scott, “Interaction between quantum paraelectricity and ferroelasticity in $SrTiO_3$,” *J. Phys. Condens. Matter*, vol. 17, pp. 7009–7022, 2005.

[12] N. Sai and D. Vanderbilt, “First-principles study of ferroelectric and antiferrodistortive instabilities in tetragonal $SrTiO_3$,” *Phys. Rev. B*, vol. 62, no. 21, pp. 942–950, 2000.

[13] R. Wördenweber and Y. Dai, “Strain Engineering of $SrTiO_3$,” in *Strontium Titanate: Synthesis, Properties and Uses*, New York: Nova Science Publishers, Inc., 2019, pp. 101–155.

[14] K. A. Müller and H. Burkard, “$SrTiO_3$: An intrinsic quantum paraelectric below 4 K,” *Phys. Rev. B*, vol. 19, no. 7, pp. 3593–3602, 1979.

[15] J. Engelmayer *et al.*, “Ferroelectric order versus metallicity in Sr(1−x) Ca(x) TiO(3−δ) (x=0 . 009),” *Phys. Rev. B*, vol. 100, no. 19, p. 195121, 2019.

[16] J. G. Bednorz and K. A. M̈ller, “Sr(1-x) Ca(x) TiO_3: An XY Quantum Ferroelectric with Transition to Randomness,” *Phys. Rev. Lett.*, vol. 52, no. 25, pp. 2289–2292, 1984.

[17] Y. L. Li *et al.*, “Phase transitions and domain structures in strained pseudocubic (100) $SrTiO_3$ thin films,” *Phys. Rev. B*, vol. 73, no. 184112, 2006.

[18] R. Wördenweber, J. Schubert, T. Ehlig, and E. Hollmann, “Relaxor ferro- and paraelectricity in anisotropically strained $SrTiO_3$ films,” *J. Appl. Phys.*, vol. 113, no. 164103, 2013.

[19] Y. Dai, J. Schubert, E. Hollmann, G. Mussler, and R. Wördenweber, “Engineering of the Curie temperature of epitaxial Sr(1−x) Ba(x) TiO_3 films via strain,” *J. Biol. Chem.*, vol. 120, no. 114101, 2016.

[20] H. W. Jang *et al.*, “Ferroelectricity in strain-free SrTiO3 thin films,” *Phys. Rev. Lett.*, vol. 104, no. 19, 2010.

[21] D. G. Schlom, L.-Q. Chen, C.-B. Eom, K. M. Rabe, S. K. Streiffer, and J.-M. Triscone, “Strain Tuning of Ferroelectric Thin Films,” *Annu. Rev. Mater. Res.*, vol. 37, no. 1, pp. 589–626, 2007.

[22] J. H. Haeni *et al.*, “Room-temperature ferroelectricity in strained $SrTiO_3$,” *Nature*, vol. 430, no. 7001, pp. 758–761, 2004.

[23] R. Xu *et al.*, “Strain-induced room-temperature ferroelectricity in $SrTiO_3$ membranes,” *Nat. Commun.*, vol. 11, no. 3141, 2020.

[24] C. Lee *et al.*, “Effect of reduced dimensionality on the optical band gap of $SrTiO_3$,” *Appl. Phys. Lett.*, vol. 102, no. 122901, pp. 1–6, 2013.

[25] K. Van Benthem, C. Elsässer, and R. H. French, “Bulk electronic structure of $SrTiO_3$: Experiment and theory,” *J. Appl. Phys.*, vol. 90, no. 6156–64, 2001.

[26] Y. Ishida, R. Eguchi, M. Matsunami, K. Horiba, M. Taguchi, and A. Chainani, “Coherent and Incoherent Excitations of Electron-Doped $SrTiO_3$,” vol. 056401, pp. 3–6, 2008.

[27] Y. A. Fujimori, I. Hase, M. Nakamura, H. Namatame, Y. Fujishima *et al.*, “Doping-induced changes in the electronic structure of $La(x)Sr(1-x)TiO_3$: Limitation of the one-electron rigid-band model and the Hubbard model,” *Phys. Rev. B*, vol. 46, no. 9841, 1992.

[28] O. N. Tufte and P. W.Chapman, “Electron Mobility in Semiconducting Strontium Titanate,” *Phys. Rev.*, vol. 155, no. 3, pp. 796–802, 1967.

[29] N. Devices, *Nanoelectronics and Information Technology : Advanced Electronic Materials and Novel Devices Publications Publications Catalog Catalog*, 3rd ed., no. November. Wiley-VCH; 3rd edition (May 29, 2012), 2004.

[30] J. F. Scott, “Applications of Modern Ferroelectrics,” *Science (80-.).*, vol. 315, no. 5814, pp. 954–959, Feb. 2007.

[31] T. Mikolajick *et al.*, “Next generation ferroelectric materials for semiconductor process integration and their applications,” *J. Appl. Phys.*, vol. 100901, no. 129, p. 100901, 2021.

[32] T. H. Arima, “Spin-driven ferroelectricity and magneto-electric effects in frustrated magnetic systems,” *J. Phys. Soc. Japan*, vol. 80, no. 5, pp. 1–14, 2011.

[33] T. Aoyama, K. Yamauchi, A. Iyama, S. Picozzi, K. Shimizu, and T. Kimura, “Giant spin-driven ferroelectric polarization in $TbMnO_3$ under high pressure,” *Nat. Commun.*, vol. 5:4927, 2014.

[34] T. Kimura, T. Goto, H. Shintani, K. Ishizaka, T. Arima, and Y. Tokura, “Magnetic control of ferroelectric polarization,” *Nature*, vol. 426, no. 6962, pp. 55–58, 2003.

[35] I. A. Sergienko and E. Dagotto, “Role of the Dzyaloshinskii-Moriya interaction in multiferroic perovskites,” *Phys. Rev. B*, vol. 73, no. 094434, pp. 1–5, 2006.

[36] D. J. Kim *et al.*, “Room-Temperature Ferroelectricity in Hexagonal $TbMnO_3$ Thin Films,” *Adv. Mater.*, vol. 26, no. 45, pp. 7660–7665, 2014.

[37] C. J. M. Daumont *et al.*, “Epitaxial $TbMnO_3$ thin films on $SrTiO_3$ substrates: A structural study,” *J. Phys. Condens. Matter*, vol. 21, no. 18, 2009.

[38] D. Rubi, C. De Graaf, C. J. M. Daumont, D. Mannix, R. Broer, and B. Noheda, “Ferromagnetism and increased ionicity in epitaxially grown $TbMnO_3$ films,” *Phys. Rev. B - Condens. Matter Mater. Phys.*, vol. 79, no. 1, pp. 1–5, 2009.

[39] R. E. Newnham, *Properties of Materials: Anisotropy, Symmetry, Structure*. OUP Oxford, 2005.

[40] G. Lalitha and P. Venugopal Reddy, “Elastic behavior of some manganite-based orthorhombic $RMnO_3$ (R=Sm, Eu, Gd, Dy) multiferroics,” *J. Magn. Magn. Mater.*, vol. 320, no. 5, pp. 754–759, 2008.

[41] A. M. Glazer, “The classification of tilted octahedra in perovskites,” *Acta Crystallogr. Sect. B*, vol. 28, no. 11, pp. 3384–3392, 1972.

[42] D. J. Passos, “From manganites to ferrites: a study on the structural, magnetic and magnetoelectric properties, MSc Thesis,” MSc Thesis. Technical report, University of Porto, 2015.

[43] P. M. Woodward, “Octahedral Tilting in Perovskites. I . Geometrical Considerations,” *Acta Crystallogr. Sect. B*, vol. 53, pp. 32–43, 1997.

[44] J. A. Alonso, M. J. Martínez-Lope, M. T. Casais, and M. T. Fernández-Díaz, “Evolution of the Jahn-Teller distortion of MnO6 octahedra in $RMnO_3$ perovskites (R = Pr, Nd, Dy, Tb, Ho, Er, Y): A neutron diffraction study,” *Inorg. Chem.*, vol. 39, no. 5, pp. 917–923, 2000.

[45] T. Kimura *et al.*, “Distorted perovskite with e1g configuration as a frustrated spin system,” *Phys. Rev. B*, vol. 68, no. 060403, pp. 1–4, 2003.

[46] K. Shimamoto *et al.*, “Single-axis-dependent structural and multiferroic properties of orthorhombic $RMnO_3$ (R=Gd-Lu),” *Phys. Rev. B*, vol. 95, no. 18, pp. 1–9, 2017.

[47] N. S. Fedorova *et al.*, “Relationship between crystal structure and multiferroic orders in orthorhombic perovskite manganites,” *Phys. Rev. Mater.*, vol. 2, no. 10, pp. 1–15, 2018.

[48] T. Goto, T. Kimura, G. Lawes, A. P. Ramirez, and Y. Tokura, “Ferroelectricity and Giant Magnetocapacitance in Perovskite Rare-Earth Manganites,” *Phys. Rev. Lett.*, vol. 92, no. 25, pp. 1–4, 2004.

[49] M. Mochizuki and N. Furukawa, “Microscopic model and phase diagrams of the multiferroic perovskite manganites,” *Phys. Rev. B - Condens. Matter Mater. Phys.*, vol. 80, no. 13, pp. 1–22, 2009.

[50] R. M. A. V. da Silva, “From Structural Distortions to Physical Properties in Orthorhombic Rare-Earth Perovskites,” University of Porto, 2019.

[51] M. Mostovoy, “Ferroelectricity in Spiral Magnets,” *Phys. Rev. Lett.*, vol. 96, no. 067601, pp. 1–4, 2006.

[52] H. Katsura, N. Nagaosa, and A. V Balatsky, “Spin Current and Magnetoelectric Effect in Noncollinear Magnets,” *Phys. Rev. Lett.*, vol. 95, no. 057205, pp. 1–4, 2005.

[53] T. Arima *et al.*, “Magnetic-field-induced transition in the lattice modulation of colossal magnetoelectric $GdMnO_3$ and $TbMnO_3$ compounds,” *Phys. Rev. B*, vol. 72, no. 100102(R), pp. 2–5, 2005.

[54] P. R. Scott, “High - pressure synchrotron x-ray diffraction study of $RMnO_3$ (R = Eu , Gd , Tb and Dy) up to 50 GPa My IOPscience,” vol. 3, no. March 2014, 2012.

[55] C. Lin, Y. Zhang, J. Liu, X. Li, and Y. Li, “Pressure-induced structural change in orthorhombic perovskite $GdMnO_3$,” *J. Phys. Condens. Matter*, vol. 24, no. 11, p. 115402, 2012.

[56] J. Oliveira *et al.*, “Structural and insulator-to-metal phase transition at 50 GPa in $GdMnO_3$,” *Phys. Rev. B*, vol. 85, no. 052101, pp. 1–5, 2012.

[57] K. Noda, S. Nakamura, J. Nagayama, and H. Kuwahara, “Magnetic field and external-pressure effect on ferroelectricity in manganites: Comparison between $GdMnO_3$ and $TbMnO_3$,” *J. Appl. Phys.*, vol. 97, no. 10, pp. 2012–2015, 2005.

[58] T. Kimura, G. Lawes, T. Goto, Y. Tokura, and A. P. Ramirez, “Magnetoelectric phase diagrams of orthorhombic $RMnO_3$ (R=Gd, Tb, and Dy),” *Phys. Rev. B - Condens. Matter Mater. Phys.*, vol. 71, no. 22, pp. 1–13, 2005.

[59] M. Tokunaga, Y. Yamasaki, Y. Onose, M. Mochizuki, N. Furukawa, and Y. Tokura, “Novel Multiferroic State of Eu(1-X) Y(x) MnO_3 in High Magnetic Fields,” *Phys. Rev. Lett.*, vol. 103, no. 187202, pp. 3–6, 2009.

[60] M. N. Grisolia *et al.*, “Structural, magnetic, and electronic properties of $GdTiO_3$ Mott insulator thin films grown by pulsed laser deposition,” *Appl. Phys. Lett.*, vol. 105, no. 17, p. 172402, Oct. 2014.

[61] D. Lee *et al.*, “Epitaxial stabilization of artificial hexagonal $GdMnO_3$ thin films and their magnetic properties,” *Appl. Phys. Lett.*, vol. 90, no. 182504, pp. 2–5, 2007.

[62] D. Lee, J. Lee, S. Yup, P. Murugavel, Y. Ko, and J. Chung, “Growth behavior of artificial hexagonal $GdMnO_3$ thin films,” *J. Cryst. Growth*, vol. 310, pp. 829–835, 2008.

[63] E. Vlakhov *et al.*, “Magnetron sputtering deposition and characterization of $GdMnO_3$ thin films,” *J. Optoelectron. Adv. Mater.*, vol. 9, no. 2, pp. 456–459, 2007.

[64] S. Mukherjee *et al.*, “Multiferroic phase diagram of E-type $RMnO_3$ films studied by neutron and X-ray diffraction,” *Phys. Rev. B*, vol. 98, no. 174416, pp. 1–12, 2018.

[65] X. Li *et al.*, “Novel multiferroicity in $GdMnO_3$ thin films with self-assembled nano-twinned domains,” *Sci. Rep.*, vol. 4, no. 1, p. 7019, May 2015.

[66] Y. Romaguera-Barcelay, J. Agostinho Moreira, A. Almeida, P. B. Tavares, and J. Pérez De La Cruz, “Structural, electrical and magnetic properties of magnetoelectric $GdMnO_3$ thin films prepared by a sol-gel method,” *Thin Solid Films*, vol. 564, pp. 419–425, 2014.

[67] Y. Romaguera-barcelay, J. A. Moreira, A. Almeida, J. P. Araújo, and J. P. De, “Dimensional effects on the structure and magnetic properties of $GdMnO_3$ thin films,” *Mater. Lett.*, vol. 70, pp. 167–170, 2012.

[68] T. Lottermoser, T. Lonkai, U. Amann, and M. Fiebig, “Magnetic phase control by an electric field,” *Nature*, vol. 430 (6999), pp. 541–544, 2004.

[69] R. Scherwitzl, “Metal-insulator transitions in nickelate heterostructures,” Thèse de doctorat: Université de Genève, 2012.

[70] A. Vailionis *et al.*, “Misfit strain accommodation in epitaxial ABO_3 perovskites: Lattice rotations and lattice modulations,” *Phys. Rev. B - Condens. Matter Mater. Phys.*, vol. 83, no. 6, pp. 1–13, 2011.

[71] C. Huang and L. Chen, “Effects of interfaces on the structure and novel physical properties in epitaxial multiferroic $BiFeO_3$ ultrathin films,” *Materials (Basel).*, vol. 7, no. 7, pp. 5403–5426, 2014.

[72] S. Middey, J. Chakhalian, P. Mahadevan, J. W. Freeland, A. J. Millis, and D. D. Sarma, “Physics of Ultrathin Films and Heterostructures of Rare-Earth Nickelates,” *Annu. Rev. Mater. Res.*, vol. 46, no. 1, pp. 305–334, 2016.

[73] “www.surfacenet.de/stocklist-catalogue-of-substrates-targets.html.” .

[74] J. E. Kleibeuker *et al.*, “Atomically defined rare-earth scandate crystal surfaces,” *Adv. Funct. Mater.*, vol. 20, no. 20, pp. 3490–3496, 2010.

[75] Y. Romaguera-Barcelay, J. Agostinho Moreira, G. González-Aguilar, A. Almeida, J. P. Araujo, and J. Pérez De La Cruz, “Synthesis of orthorhombic rare-earth manganite thin films by a novel chemical solution route,” *J. Electroceramics*, vol. 26, no. 1–4, pp. 44–55, 2011.

[76] S. A. Campbell, *Fabrication Engineering at the Micro and Nanoscale*, Third Edit. New York: Oxford University Press, Inc., 2008.

[77] S. M. Rossnagel, “Thin film deposition with physical vapor deposition and related technologies,” *J. Vac. Sci. Technol. A Vacuum, Surfaces, Film.*, vol. 21, no. 5, pp. S74–S87, Sep. 2003.

[78] L. Marton and R. L. Sproull, “Advances in Electronics and Electron Physics,” *Phys. Today*, vol. 13, no. 3, pp. 54–55, Mar. 1960.

[79] M. Ohring, “Vacuum Science and Technology,” in *The Materials Science of Thin Films*, M. Ohring, Ed. Academic Press, 1992, pp. 49–77.

[80] R. Bosco, J. Van Den Beucken, S. Leeuwenburgh, and J. Jansen, “Surface Engineering for Bone Implants: A Trend from Passive to Active Surfaces,” *Coatings*, vol. 2, no. 3, pp. 95–119, Jul. 2012.

[81] M. Ohring, *Materials Science of Thin Films - Depositon & Structure*, 2nd ed. Academic Press; 2nd edition, 2001.

[82] V. Gomes, “Micro e Nanofibras multiferróicas preparadas por electrospinning,” Tese Doutoramento; Universidade do Minho, 2016.

[83] M. Ohring, *Materials Science of Thin Films*, 2nd ed. San Diego: Academic Press, 2002.

[84] T. Ohnishi, K. Shibuya, T. Yamamoto, and M. Lippmaa, “Defects and transport in complex oxide thin films,” *J. Appl. Phys.*, vol. 103, no. 10, pp. 0–6, 2008.

[85] H. T. G. Hentzell, D. A. Smith, and C. Grovernor, “The development of grain structure during growth of metallic thin films,” *Acta Metall.*, vol. 32, no. 5, pp. 773–781, 1984.

[86] S. Y. Dieter Wolf, *Materials Interfaces: Atomic-level Structure and Properties*. Springer Dordrecht, 1992.

[87] “http://www.physics.udel.edu/yji/PHYS624/Chapter3.pdf.” .

[88] J. Epp, *X-ray diffraction (XRD) techniques for materials characterization*. Elsevier Ltd, 2016.

[89] F. Figueiras, “Study of Multiferroic Materials,” PhD thesis, University of Aveiro, 2011.

[90] Miho Yasaka, “X-ray thin-film measurement techniques V: X-ray reflectivity measurement,” *The Rigaku Journal*, vol. 26, no. 2, 2010.

[91] T. C. Huang, R. Giiles, and G. Will, “Thin-film thickness and density determination from X-ray reflectivity data using a conventional power diffractometer,” *Thin Solid Films*, vol. 230, pp. 99–101, 1993.

[92] C. P. M. Sá, “Carcterização Morfológica, Microestrutural e Micronalítica de Materiais por Microscopia Electrónica de Varrimento e Microanálise por raios X,” 2006.

[93] R. F. Egerton, *Physical principles of electron microscopy*, vol. 8, no. 12. Boston: Springer Science+Business Media, Inc., 2005.

[94] W. Zhou and Z. L. Wang, *Scanning microscopy for nanotechnology: Techniques and applications*. New York, NY: Springer New York, 2007.

[95] W. Denk and H. Horstmann, “Serial block-face scanning electron microscopy to reconstruct three-dimensional tissue nanostructure.,” *PLoS Biol.*, vol. 2, no. 11, p. e329, Nov. 2004.

[96] Y. Ding and D. O. Northwood, “Methods for preparation of cross-sectional scanning electron microscopy specimens and their application to corroded specimens of a zirconium alloy and TiN coated stainless steel,” *Mater. Charact.*, vol. 29, no. 1, pp. 25–33, Jul. 1992.

[97] C. R. Brundle, C. A. Evans, and S. Wilson, *Encyclopedia of Materials Characterization: Surfaces, Interfaces, Thin Films*. 1992.

[98] Dieter Schild, “X-ray Photoelectron Spectroscopy,” in *Hydrogen Technology*, A. Léon, Ed. Springer Berlin Heidelberg, 2008, pp. 575–601.

[99] J.F.Moulder, W. F. Stickle, P.E. Sobol, and K. D. Bomben, *Handbook of X-Ray Photoelectron Spectroscopy: A Reference Book of Standard Spectra for Identification and Interpretation of XPS Data*. Eden Prairie, Physical Electronics Division, Perkin-Elmer Corp., 1992.

[100] Kai Siegbahn, *Alpha-, Beta- and Gamma-Ray Spectroscopy*. North-Holland, Amsterdam: Elsevier, 1968.

[101] C. Zeng, C. Vitale-Sullivan, and X. Ma, “In Situ Atomic Force Microscopy Studies on Nucleation and Self-Assembly of Biogenic and Bio-Inspired Materials,” *Minerals*, vol. 7, no. 9, p. 158, Aug. 2017.

[102] N. J. Kidner, Z. J. Homrighaus, T. O. Mason, and E. J. Garboczi, “Modeling interdigital electrode structures for the dielectric characterization of electroceramic thin films,” *Thin Solid Films*, vol. 496, no. 2, pp. 539–545, Feb. 2006.

[103] W. S. Ferreira, “Competitive Exchange Magnetic Interactions and Magnetoelectric Coupling in Eu(1−x) Y(x) MnO_3,” PhD thesis, Universidade do Porto, 2011.

[104] A. S. F. Kremer, *Broadband Dielectric Spectroscopy*. Berlin, Heidelberg: Springer Berlin Heidelberg, 2003.

[105] J. Vanderschueren and J. Gasiot, “Thermally stimulated relaxation in solids,” in *Topics in Applied Physics, vol 37*, P. Bräunlich, Ed. Springer Berlin Heidelberg, 1979.

[106] Y. K. T. Yamanaka, N. Hirai, “Structure change of Ca(1–x) Sr(x) TiO_3 perovskite with composition and pressure,” *Am. Mineral.*, vol. 87, no. 1997, pp. 1183–1189, 2002.

[107] M. C. Biesinger, B. P. Payne, A. P. Grosvenor, L. W. M. Lau, A. R. Gerson, and R. S. C. Smart, “Resolving surface chemical states in XPS analysis of first row transition metals, oxides and hydroxides: Cr, Mn, Fe, Co and Ni,” *Appl. Surf. Sci.*, vol. 257, no. 7, pp. 2717–2730, Jan. 2011.

[108] I. Horcas, R. Fernández, J. M. Gómez-Rodríguez, J. Colchero, J. Gómez-Herrero, and A. M. Baro, “WSXM : A software for scanning probe microscopy and a tool for nanotechnology,” *Rev. Sci. Instrum.*, vol. 78, no. 1, p. 013705, Jan. 2007.

[109] T. Mori, N. Kamegashira, T. Shishido, and T. Fukuda, “Crystal growth and crystal structures of the $LnMnO_3$ perovskites: Ln = Nd, Sm, Eu and Gd,” *Mater. Lett.*, vol. 54, no. 2–3, pp. 238–243, 2002.

[110] S. Ramaiyan Mahadevan, S. Varadarajan, A. M. Awasthi, and S. Natarajan, “Studies on dielectric relaxation in ceramic multiferroic $Gd(1-x)\,Y(x)\,MnO_3$,” *J. Am. Ceram. Soc.*, vol. 100, no. 6, pp. 2596–2603, 2017.

[111] R. V. Silva, “Ferroelectricity, Magnetically-induced Through, Unraveled Coupling, Spin-phonon,” Master thesis, University of Porto, 2013.

[112] D. G. Friend and M. L. Huber, “Thermophysical property standard reference data from NIST,” *Int. J. Thermophys.*, vol. 15, no. 6, pp. 1279–1288, Nov. 1994.